Quantum dynamics revealed in weakly coupled quantum dot - superconductor turnstiles

David van Zanten

UNIVERSITÉ GRENOBLE ALPES

THÈSE

Pour obtenir le grade de

DOCTEUR DE L'UNIVERSITÉ GRENOBLE ALPES

Spécialité : **Physique/Physique de matiere condensee**

Arrêté ministériel : 7 août 2006

Présentée par

David van Zanten

Thèse dirigée par **Prof. Dr. Hervé Courtois**
et codirigée par **Dr. Clemens Winkelmann**

préparée au sein du **Institut Néel - CNRS**
et de **Ecole Doctorale de Physique**

Dynamique quantique dans un tourniquet à électrons basé sur une boîte quantique

Thèse soutenue publiquement le **1 juin 2015**, devant le jury composé de :

Prof. Dr. Philippe Lafarge
Professeur, Université Paris Diderot, Président
Prof. Dr. Jukka Pekola
Professeur, Aalto University, Rapporteur
Prof. Dr. Ir. Herre van der Zant
Professeur, Technische Universiteit Delft, Rapporteur
Dr. Xavier Jehl
Ingénieur, CEA Grenoble, Membre
Prof. Dr. Hervé Courtois
Professeur, Université Joseph Fourier/Institut Néel-CNRS, Membre
Dr. Clemens Winkelmann
Maître de Conférences, Grenoble INP/Institut Néel-CNRS, Membre

"Abstract"

Accurate control over the state and motion of *single* individual electrons would enable a variety of appealing applications reaching from quantized to quantum coherent electron sources. Realizing the accuracy of quantized current sources required for a metrological standard is however extremely challenging and has naturally fuelled fundamental research into single electron transport through mesoscopic structures.

A promising candidate, foreseen to meet the demand, combines the concept of quantized charge in single electron transistors (SETs) and the gapped density of states in superconducting metals (hence called hybrid electron turnstile), to produce a quantized current. The time-correlated electron transport (sub-poissonian) between the superconducting leads is conveyed by the continuous density of states of the central normal island. The large amount of available states at the normal island, although favourable in terms of tunnel coupling, has nevertheless two important ramifications i.e. 1) thermal fluctuations and 2) adverse higher-order processes, which limit the performance of hybrid electron turnstiles.

Inspired by this ingenious application and the advances in quantum dot transport, we explore the operation of a hybrid electron turnstile embodying a bottom-up quantum dot instead of the usual metallic island. The desired devices are obtained by controlled electromigration of aluminium nano-wires preceded by the deposition of gold nano-particles. This in-situ process (conducted at 4 K) produces pristine tunnel junctions between aluminium leads and gold nano-particles with a yield of $\sim 4\%$.

We characterize the stationary and turnstile operation by direct current measurements at $\sim$ 100 mK, in a heavily filtered, but electromigration compatible, inverse dilution refrigerator. Analysis of the acquired conductance maps under stationary conditions, reveal a large charging energy ($\gtrsim$ 10 meV) and mean level spacing ($\gtrsim$ 1 meV). With a detailed study of the coherence peak broadening at the Coulomb blockade (CB) threshold, we show that electron transport through the quantum dot is conveyed by a single quantum level. Although the tunnel coupling is weak, the single level life-time is dominated by the lead - quantum dot hybridization as thermal energy fluctuation and in-elastic scattering are suppressed by the large single level spacing on the quantum dot

and the superconducting gap in the leads. The observation of sub-threshold resonances parallel to the CB diamond edges are consistent with earlier predicted higher-order Cooper-pair - electron (CPE) cotunneling processes.

Under turnstile operation a periodic modulation signal (sine or square wave) is added to the static gate potential. We demonstrate quantized current up to 200 MHz at which its accuracy starts to worsen due to missed tunnel events. Strong experimental evidence of the single quantum dot level nature of our turnstile device is provided by a sharp onset of backtunneling processes and the temperature-robust operation beyond 300 mK.

Finally we observe a systematic current suppression unique to the low frequency sine wave operation. Supported by theoretical work, we show that the underlying missed tunnel events are caused by adiabatic traverses across the avoided crossing of a quantum dot level and superconducting gap edges. These experiments deliver the first experimental observation of the level repulsion between an electronic discrete state and a semi-continuum and demonstrate the quantum coherent evolution of our devices under adiabatic operation conditions.

"Résumé"

Le contrôle du nombre et de l'état quantique d'électrons individuels est un élément clé pour la construction d'applications innovantes comme les sources à un électron ou les standards métrologiques de courant. La difficulté d'atteindre la précision métrologique pour une source de courant alimente la recherche fondamentale sur le transport individuel d'électrons dans les structures mésoscopiques.

Un candidat prometteur combine le concept de quantification de la charge dans un transistor à un électron (Single Electron Transistor, SET) et la bande interdite de la densité d'états d'électrodes supraconductrices. Le transport corrélé en temps (sub-poissonien) d'électrons entre les électrodes supraconductrices est alors assuré par la densité d'états continue de l'ilot métallique central. Le grand nombre d'états électroniques disponibles dans lilot, bien que favorable en termes de couplage tunnel, a néanmoins deux conséquences importantes que sont les fluctuations thermiques et des processus parasites d'ordre supérieur, ce qui limite la performance de ces dispositifs.

Dans ce contexte, nous explorons le transport de charges dans un tourniquet à électrons hybride basé sur une boîte quantique en lieu et place de l'ilot métallique. Les dispositifs sont réalisés par l'électromigration contrôlée de constrictions d'Aluminium précédée par le dépôt aléatoire de nano-particules d'or. Ce procédé in-situ (réalisé à basse température) permet l'obtention de jonctions tunnel entre des électrodes supraconductrices d'aluminium et nano-particules d'or avec un taux de succès de l'ordre de 4%.

Nous caractérisons le transport statique et en fréquence dans ces nanostructures par la mesure statique du courant à une température de 100 mK dans un environnement fortement filtré, mais néanmoins compatible avec l'électro-migration, d'un réfrigérateur à dilution. L'analyse des cartes de conductance en fonction des tensions drain-source et de grille révèle une énergie de charge très élevée de l'ordre de 10 meV et un écart entre niveaux discrets d'énergie de l'ordre de 1 meV. Par une étude détaillée de l'élargissement des pics de cohérence au seuil du blocage de Coulomb, nous montrons que le transport électronique est assuré par un niveau unique dans la boîte quantique. Bien que le couplage tunnel soit faible, le temps de vie d'un électron dans un niveau donné est dominé

par l'hybridation des états électroniques entre les électrodes et la boîte quantique. En effet, les fluctuations thermiques et les processus inélastiques sont inopérants du fait du grand écart d'énergie entre niveaux et de la bande interdite supraconductrice dans les électrodes. L'observation de résonances sous le seuil imposé par le blocage de Coulomb est décrite par des processus de co-tunneling de type paire de Cooper-électron.

Lorsqu'un signal radio-fréquence de forme sinusoïdale ou carrée est ajouté à la tension de grille, un fonctionnement de tourniquet à électron est montré. Nous obtenons un courant quantifié jusqu'à une fréquence de 200 MHz, au delà de laquelle la précision se dégrade à cause d'évènements tunnel manqués. Le couplage à un niveau unique dans la boîte quantique est clairement démontré par l'apparition d'effets de transport tunnel inversé à grande tension drain-source ainsi que l'insensibilité à la température jusqu'à environ 300 mK. Enfin, nous observons une suppression systématique du courant uniquement à basse fréquence et avec un signal r.f. sinusoïdal. En accord avec une prédiction théorique, nous montrons que les effets tunnel manqués sont causés par un processus adiabatique au travers l'anti-croisement d'un niveau quantique sur la boîte quantique avec la densité d'états des électrodes supraconductrices. Nos expériences fournissent la première démonstration expérimentale de la répulsion de niveaux entre un niveau discret et un semi-continuum, illustrant ainsi l'évolution cohérente de nos tourniquets hybrides à électron dans un régime adiabatique.

Contents

"Introduction"

The ability to control electrons with increasing versatility and accuracy is a cornerstone of modern information technology. Small electronic currents can be switched, amplified and transformed into light and heat by ordinary electronic devices present in our equipment. These devices, e.g. bipolar and field-effect transistors, light-emitting diodes and Peltier elements, typically manipulate a continuous flow of de-localized electrons very similar to a liquid (figure 1a). With the advances in modern electronic circuit technology, we gradually gain control over the motion and (quantum) state of single electrons.

The granular nature of single charges particularly appears in small insulating barriers through which electrons may only pass by the process of quantum tunneling [27]. The energy barrier, referred to as *tunnel junction*, converts an incoming flow of electrons into a poissonian distributed stream of individual charges employing the stochastic nature of the quantum tunnel process (figure 1b).

A true one-by-one motion of electrons is procured in small metallic islands contacted by two tunnel barriers (figure 1c). Charging the central island by a single additional electron goes with an associated energy cost characterized by the charging energy $E_C = e^2/2C_\Sigma$, where C_Σ is the total capacitance of the island. At low temperature ($k_BT < E_C$), well defined charge states are established i.e. the number of additional electrons on the island becomes quantized (*charge quantization*). Electrons can not be exchanged between the island and the leads as the thermal energy fluctuations (described by the Fermi-Dirac distribution) are insufficient to provide the charging energy.

With the implementation of a third electrode, capacitively coupled to the island, the electro-chemical potential required to add/remove single electrons to/from the island can be manipulated. Current between the leads will take place if and only if electrons can be both *added to* and *removed from* the island (on-state). At sufficiently low bias $eV_B < E_C$ electron transport can only proceed by *sequential tunnel events* and will therefore be correlated to the islands charge occupation. This single electron nature of the current through the island gives this three-terminal device its name i.e. *single electron transistor* (SET).

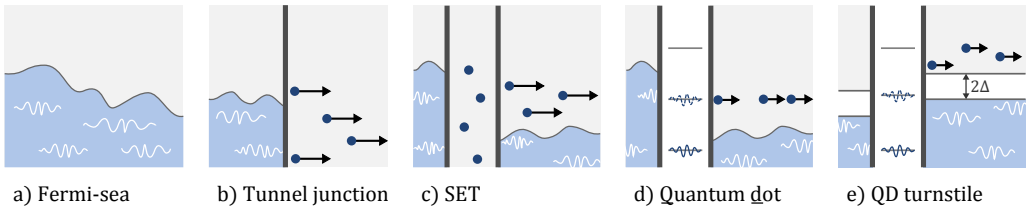

Figure 1: Energy schematics of various mesoscopic conduction channels showing increased control over electron localization, energy and time interval between two particles.

The SET on-state current is yet, despite its sequential nature, at best characterized as a (sub-poissonian) stochastic stream of electrons. There is no control over the exact time interval between two electrons, let aside individual electrons or their energy. Still, the theoretical prediction [89, 4] and observation [43] of single electron charging effects in SETs inspired the concept of a quantized current source as to define a new metrological current standard. Single electron transport, synchronized with an external cyclic signal was foreseen to produce a quantized current $I = ef$, where f is the signal frequency, with an accuracy superior to 1 ppm. Now, decades later it turns out that the objective of a metrological standard build on the quantization of charge is quite challenging and goes far further than just a definition for current. It requires exquisite control over single electrons as if operated by a pupped master.

THE QUEST FOR QUANTUM METROLOGY

The quest for this new metrological standard was initiated by the theoretical proposal of Likharev and Zorin [89] in the mid 1980s. Shortly after, in 1990, Geerligs *et al.* [44] demonstrated the quantization of current using four normal metal tunnel junctions positioned in series. A single gate electrode is capacitively coupled to the center island and provides active control over the electron transport. The operation as single electron source is best explained as a 2-stage 'load and lock' principle driven by the gate voltage (figure 2a). During the first stage, a positive gate voltage, loads a single electron and locks it at the center island. Double electron occupation is blocked by charging energy. Next, the application of a negative gate voltage enables the electron to leave the center island and directly after, the device. Sequential tunneling during the operation is blocked by the energy required to charge the neighbouring islands. This is achieved by the two additional tunnel junctions with respect to any ordinary SET. In order to give direction to the generated current a small bias voltage is required to break the symmetry between the source and drain. The necessity of a bias voltage distinguishes this 'turnstile' from electron pumps which operate at zero bias. The pursuit for metrological accuracy that followed, propelled an enormous amount of experimental effort which we will shortly discuss.

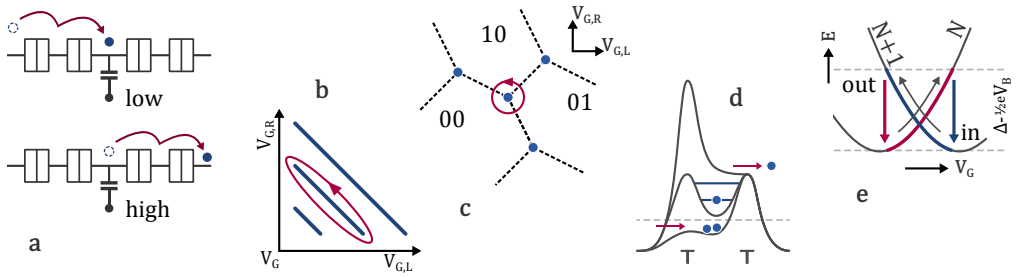

Figure 2: Schematic representations of the operation principle of various single electron sources. a) Electron transport during the first and second operation stage of the first electron turnstile [44]. A gate is capacitively coupled to the central island of four tunnel junctions in series. b,c) Stability diagram of a double MOSFET electron pump [54] (b) and double island SET (c). Blue lines/dots denote regions of non-zero current. Pump operation is illustrated by the magenta line. d) Potential landscapes of a *single parameter* tunable barrier pump illustrating 1) the initialization phase, 2) a captured electron and 3) the electron ejection. e) Energy diagram of the hybrid SET charge states as function of the gate. The superconducting gap introduces hysteresis which blocks sequential tunneling at small bias $eV_B < 2\Delta$.

Metallic tunnel junction arrays

The work of Geerligs *et al.* was closely followed by the demonstration of current quantization in the first multijunction electron pump [121]. Three metallic (non-superconducting) tunnel junctions form two islands with significant charging energy, which are each capacitively coupled to a gate electrode. The number of additional electrons on each can be manipulated by the corresponding gate potentials as shown by the stability diagram in figure 2c. Lines separating charge states indicate the degeneracy of two charge states and cross at nodes where sequential tunneling through the complete array becomes possible. To generate a quantized current, the device is operated around such a node by two phase-shifted r.f. signals applied to the gates. During each counter-clockwise cycle string in state $|00\rangle$, an electron is pulled from the left lead onto the first island while the system traverses the $|10\rangle$ state. Next the electron is moved to the second island as the system crosses the $|01\rangle$ state. Finally, the electron is ejected into the right lead and the cycle is restarted.

The theoretical analysis [56, 5] of error processes in multijunction electron pumps shows that the accuracy at low operation frequency is significantly limited by cotunneling processes which can be suppressed by extending the number of charge islands. Soon, subsequent experiments where performed with four [97] and finally five [70] separate charge islands. In the latter experiment the current accuracy was indeed significantly improved and the remaining error of 15 ppb (f = 10 MHz) is mainly determined by photon-assisted tunneling [54, 68, 67].

In more modern versions of the early 3-junctions electron pump, the two metallic island are replaced by quantum dots e.g. in carbon nanotubes [19], graphene [21]

and single dopants [129]. As the operation frequencies are inherently limited, the experimental work is meanly of fundamental value.

2DEG tunable barrier pumps

Closely after the demonstration of the electron turnstile, Kouwenhoven *et al.* [81, 82] reported on a different kind to device which constitutes the basis of most modern metrological electron pumps. Instead of manipulating the electro-chemical potential of a charge island, Kouwenhoven *et al.* utilized tunable tunnel barriers made by quantum point contacts (QPCs) in a 2DEG. Depletion of the electron gas below the QPCs forms an electro-static potential well which confines the electron wave-function. The application of two phase-shifted r.f. signals to the QPC top gates, alternately lowers the two barriers such that during each cycle an electron is 1) loaded from one lead, 2) locked inside the well and 3) finally ejected into the other lead.

Curiously it took more than a decade before this work was continued in 2007. Blumenthal *et al.* showed that a conventional 2DEG tunable barrier pump can be operated at high frequency (f = 547 MHz) without significant depression of the current accuracy ($1\sigma = 10^{-4}$). Hereto the barrier modulation was substantially revised with respect (see figure 2d) to the pioneering experiments. During the 'initialization' stage, the left barrier is lowered below the Fermi-energy of the 2DEG which allows electrons to 'flow' into the central part. During this stage, electrons experience minimal resistance which allows high frequency operation. Upon raising the barrier, most electrons leave and only a determined number of electrons become trapped. The number of captured electrons can be tuned by a third gate located between the two barriers. Finally, the electrons are ejected as the left barrier is raised high above the right. The capacitive coupling between the gates lifts the potential in the central part such that the electrons are pushed over the right barrier into the lead.

In the experimental work that followed, the operation of *single-parameter* barrier pumps was studied under magnetic field [151, 59, 36], in parallel circuits [9, 152], by their noise signatures [94], and as function frequency [60, 65] and potential landscape [137, 46]. Furthermore a theoretical model known as the decay cascade model was developed, which nicely captures the operation of tunable barrier electron pumps [59, 64]. An experimental verification was provided recently by a beautiful full counting statistic (FCS) measurement [39, 38].

Combining all prior work, Giblin *et al.* [46] were able to demonstrate a quantized current of 150 pA with a near-metrological accuracy of $1\sigma = 1.2 \cdot 10^{-6}$. This amazing result was obtained with a custom shaped device, operated under a high magnetic field (14 T) and a dedicated wave form indicating the advanced stage of this experimental field. By fitting the results to the decay cascade model the authors argue that the

obtained accuracy is actually limited by the current detection setup and should be as low as $1\sigma = 0.1 \cdot 10^{-6}$.

MOSFET tunable barrier pumps

Powered by the advancing developments in CMOS technology, the fabrication of MOSFET controlled single electrons transistors (SET) became possible early in this century [41, 157, 107]. Two adjacent metal-oxide-semiconductor field-effect transistors, integrated on a silicon nanowire, act as tunable barriers with an on/off ratio of several orders magnitude. The employment as single electron pump was first demonstrated by Ono *et al.* [106] but with limited performance. The principle of operation involved the modulation of both gated barriers (see figure 2b) within their tunnel regime. In a subsequent experiment [42] the operation frequency was increased to 100 MHz. The accuracy, still about 1%, was shown to be limited by thermal errors at the operation temperate of 17 K [154]. More recently, Jehl *et al.* [55] reported a staggering improvement of both frequency and accuracy by taking advantage of modern high performance CMOS technology (fully depleted SOI).

The single-parameter operation of MOSFET barrier pumps, first demonstrated by a Fujiwara *et al.* [40], requires a non-adiabatic raise of the active barrier similar to 2DEG tunable barrier pumps. Consequently the current accuracy is limited by the initialization stage. A better electron confinement, obtained by the implementation of a plunger gate, was shown to improve the overall device performance [130]. An alternative approach to improve electron confinement consist of the implementation of single donor atoms in the active channel [155, 85, 154]. Most recently the quantization of hole current was shown. Due to a larger effective mass, the accuracy of hole pumping is expected to be superior to electrons [155].

Hybrid SET turnstiles

Despite the vast amount of experimental work on single electron sources, a simple but promising solution remained overlooked until 2007. In their leading work, Pekola *et al.* proposed and demonstrated the turnstile operation of a single metallic island contacted by tunnel junctions to superconducting leads [117]. The device is similar to the first turnstile in terms of geometry, but takes advantage of superconducting leads as to omit the two outermost tunnel junctions. The superconducting gap (2Δ) in the lead density of states (figure 3a right) blocks quasi-particle[1] tunnel events at low energy (as shown in figure 3a) and consequently sequential tunneling at small bias $eV_B < 2\Delta$. This introduces hysteresis in charge stability with respect to normal metal SETs as is illustrated in figure 2e. A periodic manipulation of the gate potential around

[1]The electron transport in superconductors is carried by quasi-particles (single electrons) and Cooper-pairs i.e. paired electrons of double charge and integer spin.

charge degeneracy transports electron one-by-one through the turnstile, leading to a quantized current. A small bias is required to give direction to tunnel events. Although the operation of NISIN structures is possible, it suffers inherently from excessive heating and parity effects as opposed to the SINIS configuration which benefits from intrinsic cooling [61].

A theoretical analysis of first and second order error processes was provided by Averin *et al.* [3]. Thermally induced errors, appearing as subgap leakage and back-tunneling, are found to be well suppressed at a realistic electronic temperature of 100 mK in aluminium based devices. Nevertheless, proper device shielding is required as the device environment can significantly affect the effective operation temperature [133, 115, 91]. The dominating higher order error processes comprise Andreev reflection and Cooper-pair — electron (CPE) cotunneling. Andreev processes can, as a double island occupation is involved, be suppressed by a large charging energy [2, 71], whereas CPE cotunneling processes only depend on bias and cannot be easily subdued [116] other than by decreasing the tunnel coupling. This puts a theoretical upper limit to the metrological current (few tens of pA) of a single normal metal hybrid SETs. However, the parallelization of many devices, is shown to be feasible for metrological purposes [96].

Single-level hybrid turnstiles

In the work of this thesis we have explored yet another approach to suppress both thermal and quantum errors in hybrid SET devices. Further reduction of the island size to a few nanometers will strongly confine of the electron wave-function which leads to the discretization of states on the quantum dot. When the thermal energy of the quantum dot becomes smaller than the spacing between levels, the electron temperature become undefined and corresponding thermal errors vanish. Furthermore, the number of quantum dot states participating in the turnstile operation is reduced. At yet larger level spacing, exceeding the superconducting gap, the quantum dot is effectively reduced to a single level and enhanced control of quantum tunnel events is obtained. In this thesis we will first discuss the operation of the single level turnstile (chapter 5) after which we will demonstrate its operation experimentally in chapter 6.

ELECTRONIC COOLERS

Hybrid structures consisting of superconducting and normal parts have been employed since far before the single electron turnstile. Thermal excitations in normal metal part result in a smooth distribution of the electron energy described by the Fermi-Dirac distribution (figure 3a left side). In superconductors however, the gap in the quasi-particle density-of-states leads to a clear separation of occupied and unoccupied

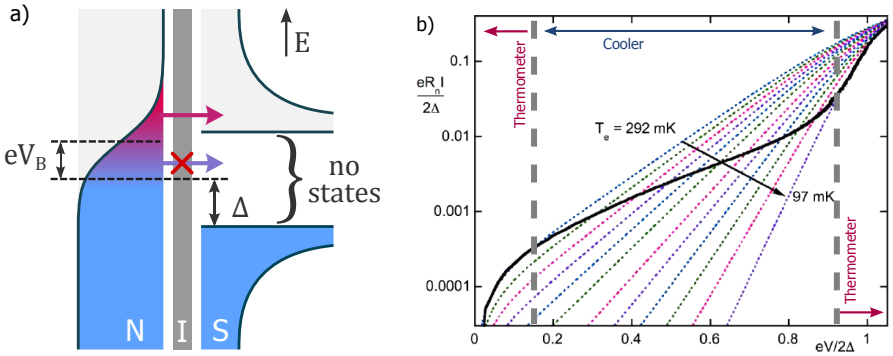

Figure 3: a) Energy schematic of an normal metal - insulator - superconductor tunnel junction. b) Experimental current - voltage relation of an low impedance NIS junctions (black line) as function of the applied bias. Dotted lines give the calculated current - voltage relation of a NIS junctions assuming various fixed electron temperatures in the normal part. (extracted from [123])

states. Electrons can only tunnel out of the normal metal if their energy is high enough to enter one of the unoccupied states in the superconductor. Thanks to this energy-selective tunneling, NIS tunnel junctions serve as sensitive probes of the electron energy distribution in the normal metal [120, 49]. When the electron-electron interaction rates (τ_{e-e}^{N}) in the normal metal exceed the tunneling rate, a local electron temperature is defined and directly given by the measured distribution. Therefore NIS junctions are often used for local thermometry [22, 45, 77].

With increasing tunnel rates (but yet below τ_{e-e}^{N}) the local energy distribution in the normal metal becomes more and more affected by the back-action of energy selective tunneling. In fact, when the junction bias is below the superconducting gap, the back-action can be utilized to cool electrons in the normal metal [86, 101]. As only 'hot' electrons (above the Fermi-energy) are allowed to tunnel out of the normal metal, the electron energy distribution becomes shaper, which translates to a decrease in electron temperature (figure 3b). By adding a second superconductor, in an SINIS configuration, also 'hot' holes are removed which doubles the cooling power of the device [86]. The steady state temperature of the normal part is obtained when the cooling power of the junction is balanced with the incoming heat flux from the normal metal lattice mediated by electron-phonon interaction.

In the limit of a small and weakly coupled island, the charging energy becomes non-negligible and the electron transport may only proceed by sequential tunneling. The integration of a gate electrode turns the SINIS cooler into a SET and makes the manipulation of heat fluxes and matching applications possible. A clear and simple example is the work of Saira *et al.* [132] in which they operate a gated SINIS structure (hybrid SET), visible in figure 4a as heat transistor. The authors show that the optimal cooling power $\dot{Q}^{opt}$ in this device can be manipulated (figure 4b) by a gate dependent

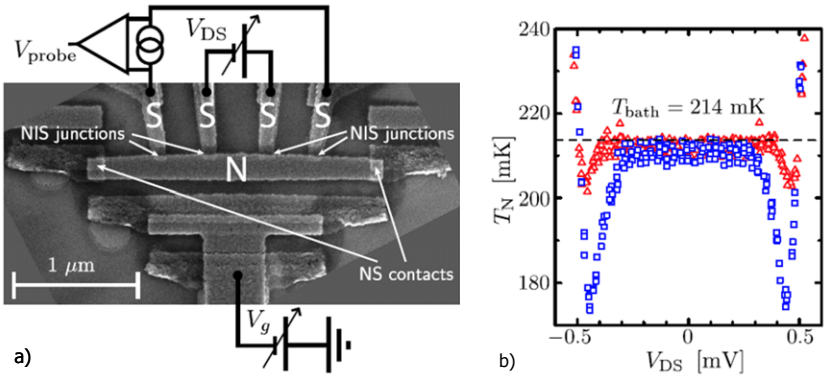

Figure 4: a) Scanning electron microscope image of a heat SINIS heat transistor. Additional SIN junctions serve as local thermometers. b) Electron temperature of the normal island as function of the bias when the gate is open (blue) and closed (red). (extracted from [132])

suppression of the maximum power $\dot{Q}^{opt}_{max}$.

With a modest charging energy of $E_C \approx 50\mu$eV the on-off ratio of the cooling power obtained at $T = 214$ mK was limited to about ≈ 30 percent. However as the maximum suppression grows exponential with E_C, it is expected that full suppression of the heat current becomes possible in the limit of large charging energy. In chapter 3 of this thesis, we will discuss on the operation of heat transistors in the limit of large charging energy ($\gtrsim 10$ meV) as observed in single molecule experiments [109, 150, 12].

The experiment of Saira *et al.* in fact preceded the onset of a new field of experimental physics known as quantum thermodynamics [113]. The previously discussed advances in electron thermometry and temperature control (heating/cooling) provide fertile grounds to study the heat transport in more complicated systems such as Coulomb blockade refrigerators [34], in single conductance channels [57] and Maxwell deamon devices [79, 80].

QUANTUM DOT SPECTROSCOPY

Superconducting - quantum dot hybrid device are interesting from a more fundamental point of view as well, as they allow us to study the hybridization between quantum dot levels and the superconductor in the weak coupling regime. Extensive studies [135, 99, 118, 119] show that in well-coupled quantum dots, the hybridization with the superconducting leads gives rise to Andreev bound states (ABS) that carry the AC and DC Josephson effect in mesoscopic devices. Till present the weak coupling limit has been far less studied. First measurements (figure 5b) of the electron transport through weakly coupled S-QD-S devices indicate the hybridization 'survives' despite the weak coupling [124].

More recently Winkelmann *et al.* [150] utilized the electro-migration technique [110]

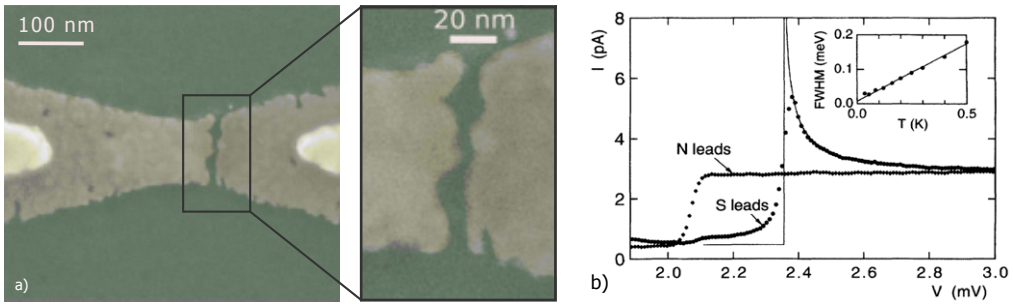

Figure 5: a) Scanning electron microscope image of a nano-gap created by the electromigration process. (extracted from [128]. b) Current-voltage relation of a quantum dot contacted by superconducting electrodes in normal and superconducting state. (extracted from [124])

with aluminium junctions to contact C60 molecules. Building on this and other [105, 108, 83, 128] successful applications in single molecule electronics, we fabricate nano-gaps (similar to figure 5a) by the electromigration of aluminium nano-wires preceded by the deposition of small gold nano-particles. In chapter 4 of this thesis, we will characterize the electron transport though these devices and show how hybridization effects manifest in this weak coupling regime.

Yet, all reports on experiments with hybrid quantum dots in the weak coupling regime are performed under stationary conditions and measure the conductance conveying by the quantum dot quasi-particle states. As we intend to operate our devices as a single electron turnstile, we have a way to breach through this frontier. In fact, the idea to exploit a single electron turnstile as probe of the system dynamics is not new [74, 94, 35]. Recently Maisi *et al.* [95] used a N-S-N turnstile device to accurately probe the lifetime of quasi-particle excitations in a small superconducting island, something which is of enormous interest to quantum computing research [126, 147]. In chapter 6 of this thesis we demonstrate the detection of an adiabatic suppression of the turnstile current in our single level turnstile devices. We show that the suppression is related to the avoided crossing of the discrete quantum dot level and the superconducting gap edge.

Chapter 1

Sample fabrication

As to obtain gated bottom-up quantum dots weakly coupled to superconducting leads by pristine tunnel junctions, we employ the controlled electro-migration of aluminium nano-wires and the deposition of small gold nano-particles. In this chapter we will discuss the lithography and deposition processes required to fabricate nano-wires located on a local back-gate capped with a high-quality insulation layer. Next, we study the deposition of gold nano-particles and discuss the compatibility of various techniques with aluminium electro-migration junctions. In the last section we consider the process electro-migration and demonstrate the relation between the maximum dissipated power and nano-wires thickness.

Chapter contents

Even though the continuing demand in more powerful and smaller integrated chips has resulted in the development of many tools used in nano-fabrication, the fabrication of quantum dots remains a challenging task. The small dimensions needed to observe the quasi-particle level spacing, require nano-meter sized junctions with a strongly coupled gate electrode.

1.1 Gate electrode lithography

For most nano-electronic devices, a gate electrode is on the foundation of their operation. Gate electrodes are used to manipulate the potential landscape in 2DEGs, create inversion layers in FETs, and manipulate the position of charge/level states in single electron transistors or quantum dots. For the last application, the one of our interest, it is important that the gate is sufficiently coupled i.e. it can modulate the electro-chemical potential of the island by at least a few times E_C ($\approx 100\,\mathrm{meV}$).

Therefore, for these devices, the gate coupling can best be qualified by the maximum charge it can induce, $q = C_G V_G^{max}$. This *gate induced charge*, is defined by (1) the capacitance C_G between the gate and the island, and (2) the maximum potential one can apply on the gate, before the gate insulation starts to leak current. While the second parameter is limited by the quality of the gate insulation, the first is determined by the device geometry [23] and the relative permittivity of the gate insulation.

Gate geometry

One can distinguish four different gate geometries: the planer back-gate, local top and back gates and side/plunger gates. Each of these has its advantages for specific devices and disadvantages for others. Planer back-gates are often used in graphene based devices [50], since they provide a large active area and do not require special fabrication[1] steps. However, because of the thick gate oxide (microbonding requires a minimum thickness of 300 nm) the gate coupling is too weak for SETs with high charging energies ($E_c > 1\,\mathrm{meV}$).

Alternatively, one can pattern a gate electrode on top of the device, effectively sandwiching it between substrate and gate. This is traditionally done in FETs [62], where the top gate regulates the inversion layer. But more recently they are also used to define the potential landscape in 2DEGs [46] and nanowires [52]. Even though a top gate would generally provide a good coupling for a SET, this geometry is not compatible with the electro-migration process, which, in our case, will be the last fabrication step. Thirdly, one can position a gate electrode to the side of the device, hence it is called a

[1] Highly doped silicon wafers with thermally grown oxides of specified thickness are commercially available

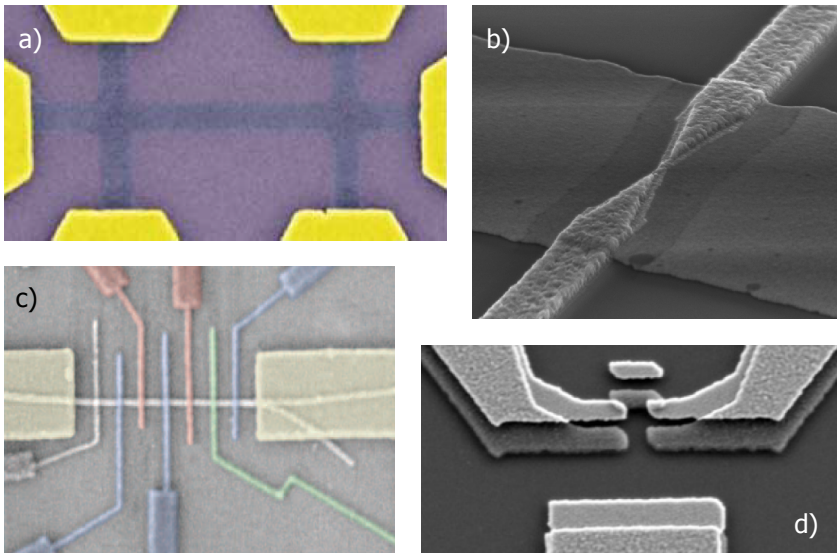

Figure 1.1: Mesoscopic devices utilizing one of the four possible gate geometries. a) Planer back gate [104], b) local back gate, c) top gate [52] and d) lateral gate [117].

lateral gate. While this geometry is compatible with electro-migration, the fabrication of lateral gates with good coupling to the island remains difficult. Primarily because minimizing the separation between gate and island below several tens of nanometers is a challenge, and secondly because the relative permittivity of vacuum is low compared to those of metallic oxides. Nevertheless a lateral gate could provide sufficient coupling for small modulations of the islands electro-chemical potential e.g. RF gate modulation which will be discussed later in this chapter.

Finally one can position a local gate underneath the island [111], which has several advantages for electro-migration devices. Since the gate is local, one can use a very thin gate insulation layer i.e. less then 10 nm thick, while keeping the device compatible with electro-migration. Moreover, the deposition of the gate insulation layer allows one to choose the dielectric constant to be as high as possible. Finally, local back gates are compatible with the use of lateral gates for small RF gate modulations. In conclusion, a local back gate has many advantages for our electro-migration devices, and is therefore our preferred approach.

Lithography process

Our fabrication process begins with the lithography of local gate electrodes. In short, we (1) clean the wafer, after which we (2-5) spincoat two layers of resist and (6) insulate the wafer with deep UV or laser light. After (8) developing the resist, we proceed with (9) the deposition of metal which we finally (10-12) lift off in a solvent. The details of this process are listed in table 1.1.

#	Description	Equipment	Comments
1	cleaning	RIE oxygen plasma	3 min
2	spincoat LOR3A	spincoater	30 s, 2000 rpm
3	bake LOR3A	hotplate	1 min, 170°C
4	spincoat UV3	spincoater	30 s, 4000 rpm
5	bake LOR3A	hotplate	1 min, 130°C
6	DUV exposure	mask-aligner MJB3	40 s, dose 0.12mW/cm^2
7	postbake	hotplate	1 min, 130°C
8	development	MF26A	30 sec
9	metal deposition	Plassys e-gun evaporator	3 nm Ti (0.3 Å/s), 30 nm Au (0.3 Å/s)
10	liftoff (1)	acetone	10 min
11	liftoff (2)	hot RemoverPG	30 min, 70°C
12	rinsing & drying	acetone, ethanol, IPA, N2	
13	cleaning	RIE oxygen plasma	3 min

Table 1.1: The detailed recipe to acquire high quality local back gates by using a bilayer resist technique for DUV optical lithography.

Generally one uses only a single layer of resist for such a lithography, but by using a bilayer resist technique, we can ensure a high quality of the gate electrode. When using a single resist layer, there is some chance the structures will have upstanding edges after lift-off, like in figure 1.2b. These so called 'batman ears' can cause (1) discontinuities in the structures on top of the gate edges and (2) shorted gates (a ohmic connection between the gate and the structures on top of the gate). Batman ears are the result of a resist layer with a finite slope (figure 1.2a), such that there can be metal deposited on the side walls of the resist.

In the bilayer resist technique the lower resist layer is, by design, more sensitive to the developing agent than the top layer, which therefore extends over the lower resist (see figure 1.2c). This resist structure ensures the metallic film on the substrate will never extends over the side walls of the lower resist and the resulting structure will have no upstanding edges. In collaboration with Thierry Crozes, we have developed a bilayer resist process compatible with laser-lithography (figure 1.2d), based on the known process for deep UV. This has allowed us to benefit from the flexibility and automatic alignment of laser-lithography.

Using a local back gate requires the alignment of the following lithography steps. To make precise alignment possible, markers are patterned in addition to the gate electrodes. Corresponding markers in the next lithography steps can be used to align the structures of subsequent lithography steps. For the deep UV process we use 4 different markers to gradually improve the alignment. First a rough alignment is performed on big markers located at the bottom and sides of the wafer. The alignment procedure

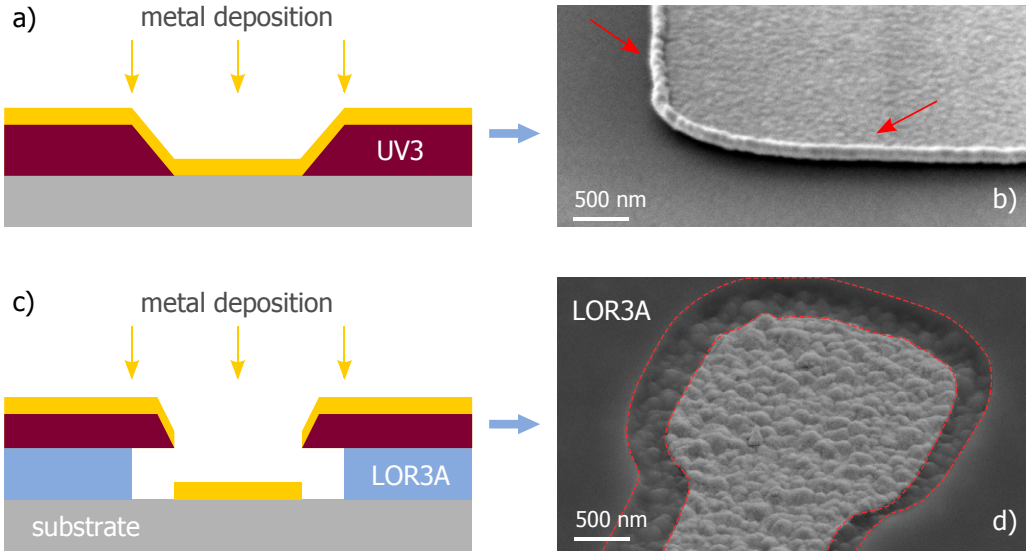

Figure 1.2: The bilayer resist technique (c, d) can be used to prevent the formation of upstanding edges (denoted by the arrows in b) after lift off, which can occur when using a single resist layer (a, b). The undercut in the bilayer resist ensures that the metallic film on the substrate will never extends over the lower resist layer. The red dotted line in (d) shows the separation between the lower resist layer (LOR3A) and the structure.

is finished with two small alignment markers located near every sample. Figure 1.3b shows two smallest alignment markers in the deep UV design. Although the gradual process improves the alignment precision, the process remains difficult and sometimes has to be redone. This contrasts with the alignment process for laser lithography in which, as it turn out, only a single alignment is necessary.

After lift off the wafers are cleaned from any residual resist by oxygen plasma and we continue with the fabrication of the gate insulation layer by atomic layer deposition (ALD).

1.2 Thin gate insulation

Local back gates are often made of aluminium, such that the gate insulation is simply obtained by letting the aluminium oxidise [47]. The resulting oxidation layer is ~ 2nm of Al_2O_3 and is covering all aluminium. Often the aluminium is actually deposited while the substrate is at liquid nitrogen temperature in order to reduce the aluminium grain size and hence the surface roughness. Insulation layers fabricated with this method generally have no leakage up to 2.5 V and provide good coupling. However, since the oxide thickness is naturally limited to about 2 nm [156], its quality is very dependent on the presence of defects and impurities. To acquire high quality gate electrodes, it is therefore of importance to create oxide layers without any defects, which turns out to be difficult and time consuming if done by natural oxidation.

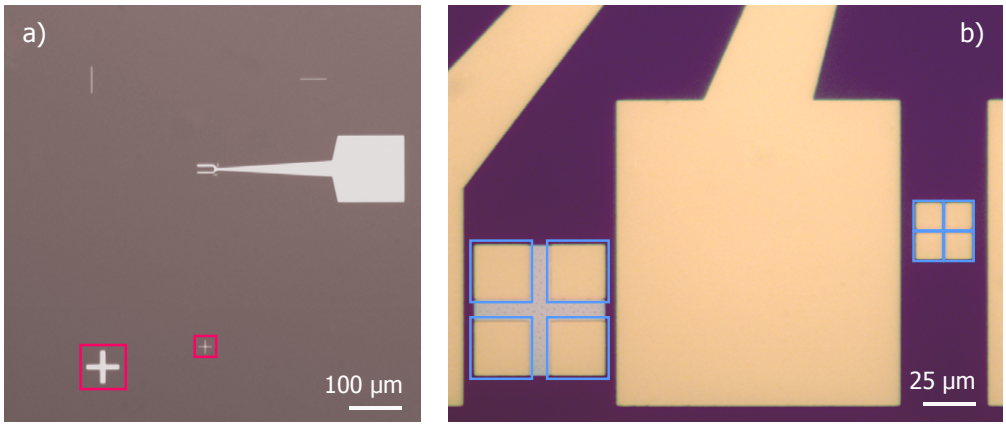

Figure 1.3: The alignment of different lithography steps is achieved by adding complementary markers to the design of subsequent layers. The gate layer (a) contains little crosses (highlighted in pink) that next to be aligned with the four little squares (highlighted in blue in (b)) in the next layer.

Fixed proces parameters	
Parameter	Value
Precursor temperature	20°C
'Tee' temperature	90°C
Chamber temperature	100°C
'Bellow' temperature	150°C

Process recipe		
#	Action	Value
1	TMA injection	0.015 s
2	waiting time	120 s
3	H_2O injection	0.015 s
4	waiting time	120 s

Table 1.2: The ALD process parameters that we used to create our high quality gate insulation layer.

Instead of growing an oxide layer, one can now, due to the development of techniques like atomic layer deposition (ALD) and chemical vapour deposition (CVD), also deposit an oxide layer, atomic layer by layer. These techniques do not only make it possible to deposit an arbitrary thickness and composition of oxide, but also to reduce the defects and impurities concentrations. Also it has been shown by Datta et al. [23] that the increase in gate coupling with decreasing insulation thickness will saturate below about 10 nm. Hence, with ALD one can deposit a thicker (~ 8nm) oxide layer to reduce the gate leakage current and increase the gate breakthrough voltage, while maintaining optimal gate coupling, and thereby maximizing the gate induced charge. Since ALD allows us to deposit an oxide layer thicker than 2 nm and with superior quality and high reproducibly, it is our preferred method to create the insulation layers.

Oxide deposition process

An atomic layer deposition process consists of four steps which are repeated subsequently. During the first and third step a given amount of respectively a precursor and H_2O are introduced into the chamber which is heated to a set temperature. During

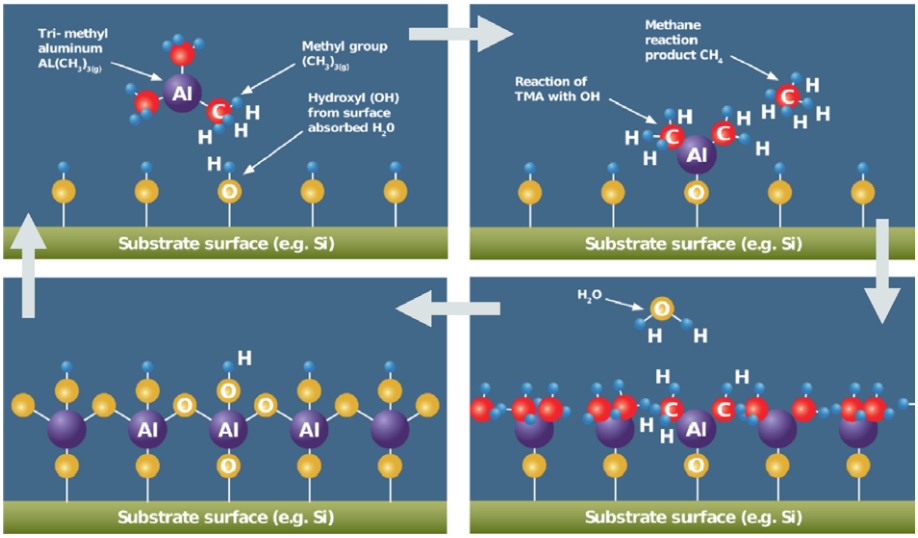

Figure 1.4: The ALD process consists of four consecutive steps that are repeated for a number of times. First a gaseous precursor is introduced in the chamber (a). During a set waiting time, the precursor molecule binds to the substrate and the resulting reaction product (methane) is removed from the chamber (b). Next gaseous H_2O is introduced in the chamber (c) which reacts with the previously introduced precursor molecules, creating an oxide layer. Again the reaction product (methane) is removed from the chamber (d). After 80 cycles the average thickness is about 8 nm.

the second (fourth) step the process waits while the precursor (H_2O) will take part in a self-limiting chemical reaction at the substrate and the reactants can be evacuated from the chamber. To obtain a high quality insulation layer, the oxide has to be amorphous [73] and contain little impurities. In order to meet both requirements one has to optimize the process parameters i.e. the chamber temperature and waiting times. Fortunately, such a process had already been developed at the Neél Institut [148] for Hf_2O_3 oxides and is listed in table 1.2.

Initially, we adopted this process to insulate the gate with 8 nm Hf_2O_3. However, because of an unknown cause, thin aluminium films (t < 30nm) have a strongly increased resistivity when deposited on Hf_2O_3, while for electro-migration it is important to have leads with little electrical resistance. Therefore, instead of using the precursor TDMAH (Hf_2O_3), we used TMA to create a layer of Al_2O_3. Gate electrodes made using this process generally have a breakthrough voltage of about 9 V and show an immeasurable high ohmic leakage resistance, as shown in figure 1.5.

1.3 The electromigration junction

The fabrication of the electromigration junctions is divided into two steps. We save precious e-beam lithography time by using deep UV or laser lithography to pattern bonding pads and contact lines of decreasing size. In the second step, performed by

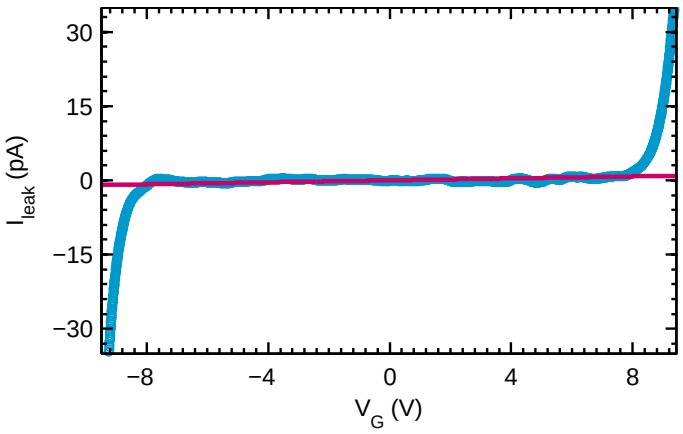

Figure 1.5: The quality of the gate insulation layer can be visualized by gate leakage current as function of the applied voltage (blue circles). The red line corresponds to a 10 TΩ resistance. This shows that the ALD process allows us to create thin and high quality gate insulation layers with a high break-through voltage (8 V) and negligible gate leakage.

electron beam lithography (EBL), these lines are continued into the leads and electromigration junctions.

The process of the first step is identical to the one of the gate (which is in detail described in table 1.1) except now 3 nm titanium and 40 nm gold are deposited. Again a bilayer resist is used, this time to insure a good electrical connection between the two different structures that make up the leads.

Figure 1.6 shows the devices after the second lithography step for both the deep UV and laser lithography processes. The designs are kept nearly identical except for a few differences. First, the DUV alignment markers are removed which allows for bigger bonding pad in the corners. Second, all the alignment markers are only present at the gate layer. Finally, the round shape of the markers (instead of the lines) enable automatic alignment in two directions (instead of one). This is an important improvement since now the calibration of writefields during the e-beam lithography step can be performed on-chip.

Electron beam lithography

Electromigration can be performed best on nanometer sized junctions, such that the process can be executed with precise control (see section 1.5). Ideally the junction are thin and small while the leads have negligible resistance. Both requirements can be easily fulfilled when using the bilayer resist technique designed by Park et.al.[110]. Here the bilayer resist is used to define a fully undercut separation between two electrodes, resembling a bridge-like shape (figure 1.7b). Combined with an angled deposition, such a structure can be used to create thin junctions under the resist bridge (non-zero

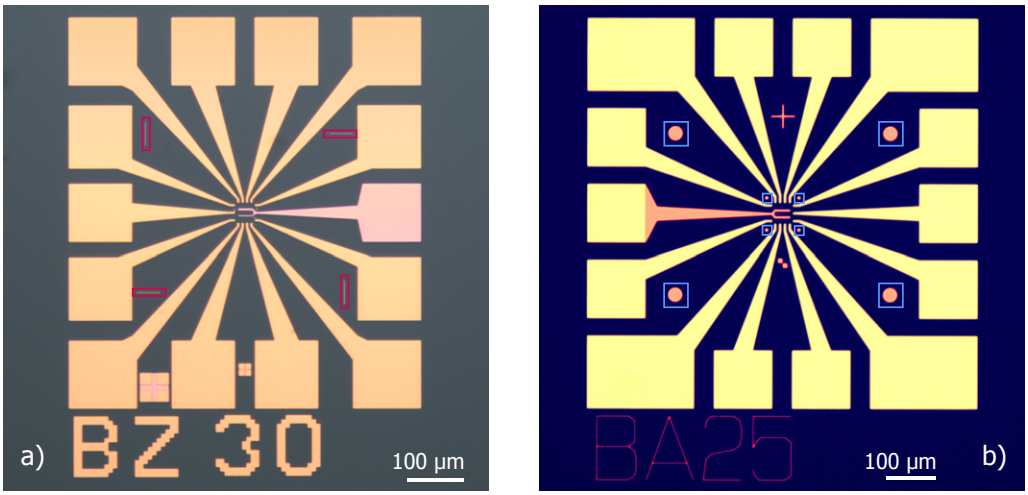

Figure 1.6: The two optical (i.e. DUV (a) and laser (b)) lithography designs, are very similar. In the design for laser lithography we have implemented 8 circular markers (highlighted in pink) that are used for the calibration of writefields and the automatic realignment during e-beam lithography. The circular markers replace the line markers (highlighted in blue) in the DUV design.

angled) contacted with thick metallic leads (zero angle) separated from each other by the width of the resist bridge (figure 1.7c).

To create our electromigration junctions we use electron beam lithography on a bilayer resist. First PMMA/MAA is spincoated which forms a relatively thick (~400 nm) resist layer with an increased sensitivity to electrons. Next, PMMA 2% is spin-coated to form a thin (~50nm) layer of resist with normal sensitivity. The difference in electron sensitivity between the two types of resist, allows us to obtain the large undercut required for the resist bridge. After insulating the structures with a 20 kV focussed electron beam, the resist is developed in a 1:3 mixture of methyl isobutylketon (MIBK) and isopropanol (IPA). To insure a sub-micrometer accurate alignment of the junctions with respect to the gate we use a two-step automatic realignment procedure on the circular markers of every sample.

Just before we proceed with the deposition of the junctions, the substrate is cleaned from any residual resist at the exposed parts using a low power oxygen plasma for about 10 seconds. Next we deposit two thin layers (13 nm) of aluminium under a positive and its opposite angle (~ 23°) followed by a thick layer (80 nm) of aluminium at zero angle without breaking vacuum. The final thick layer decreases the access resistance of the junctions and insures a continuous connection to the bonding pads. Finally the sacrificial parts of the resist are lifted in hot Remover1165 (80°C) during 1 hour. The resulting electromigration junctions are shown in figure 1.8b.

The bow-tie like shape of the junctions, visible in figure 1.8b, is not required for electromigration although is does localize the region where the nano-gap will be formed

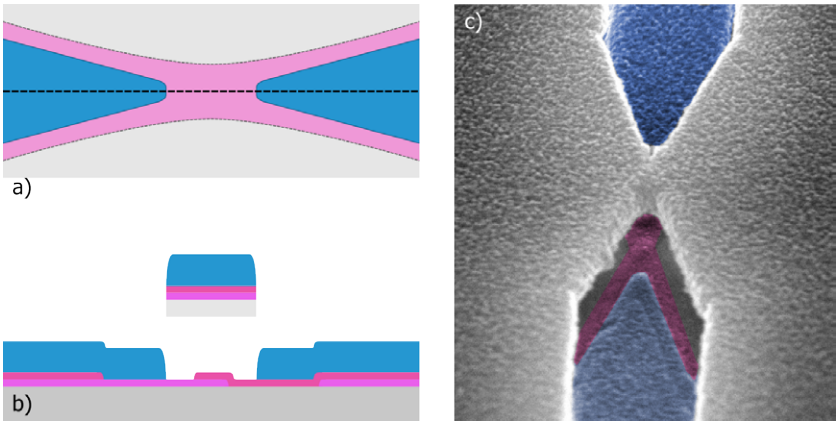

Figure 1.7: (a) Top view schematic representation of the resist structure after the development step. Grey areas are covered by both resist layers, while in the green areas all resist has been removed. Areas highlighted in pink are completely undercut, forming a bridge like structure. (b) Cross-section schematic representation along the dotted line in (a) after metal deposition. (c) Angled scanning electron microscope image of the structure after metal deposition. Underneath the resist bridge one can distinguish the overlap of the two opposite angled depositions.

#	Description	Equipment	Recipe/Comments
1	spincoat PMMA/MAA 33%	spincoater	30 s, 4000 rpm
2	bake	hotplate	5 min, 200°C
3	spincoat PMMA 2%	spincoater	30 s, 1400 rpm
4	bake	hotplate	5 min, 180°C
5	e-beam exposure	MEB	dose 150μC/cm^2
6	development (1)	MIBK/IPA 1/3	30 s
7	development (2)	IPA	1 min
8	cleaning	RIE oxygen plasma	10 s (low power)
9	metal deposition	Plassys e-gun evaporator	13 nm Al (−23°, 1 Å/s), 13 nm Al (23°, 1 Å/s), 80 nm Al (0°, 2 Å/s)
10	liftoff (1)	hot Remover1165	60 min, 80°C
11	liftoff (2)	acetone	10 min
12	rinse and dry	acetone, ethanol, IPA, N2	

Table 1.3: The details of the e-beam lithography process used to create the nano-wires for electromigration.

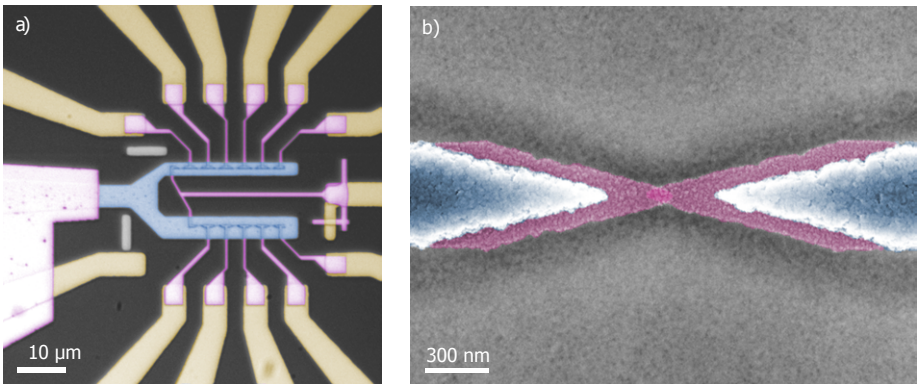

Figure 1.8: A fully fabricated device (a) consists of a gate layer (highlighted in blue), a contact layer (highlighted in pink) and several electromigration junctions (highlighted in green). The electromigration junctions (b) are created by a shadow evaporation. First, two thin layers, ~ 12 nm (highlithed in pink) are deposited under opposite angles (±23°). The angle of deposition needs to be optimized such that there is a small but present overlap between the two layers. Next, a thick layer, ~ 80 nm (highlighted in blue) is deposited under zero angle to reduce the series resistance to the junctions and to ensure a good electrical connection to the contact layer.

[110]. It has been shown by Datta et al. [23] that the lead geometry of a nano-particle based device has a dramatic effect on its gate coupling i.e. the sharper the apex of the contacts, the larger the gate coupling. It is clear from figure 1.9b that this dependence is especially present for small nano-gaps with 'thick' contacts.

RF gate modulation

As will be explained in chapter 5, the driving force of electron pumping in superconducting quantum dots is a fast oscillating gate signal around a static gate potential. This mandatory gate modulation can be achieved in different ways provided that the AC and DC gate electrodes are capacitively coupled. An ohmic connection between the two lines will short the DC gate electrode to ground, since the AC gate line contains an attenuator to thermalize the inner conductor of the coaxial line.

In nano-electromechanical systems (NEMS) and spin qubits [69], an antenna positioned close to the substrate can provide sufficient signal. However in both cases it is not the electrochemical potential of the island which is directly modulated. A more common approach is to add the DC gate and AC gate signal to each other using a bias tee lumped element located at dilution stage of the cryostat. Although this probably gives the largest gate swing, we have chosen two different approaches. In both approaches the necessary AC gate elements are patterned by electron beam lithography in the same fabrication steps as the electromigration junctions.

As pointed out before one can position a small lateral gate close by the junction. Although it is difficult to position the gate very close to the island, a sufficient gate

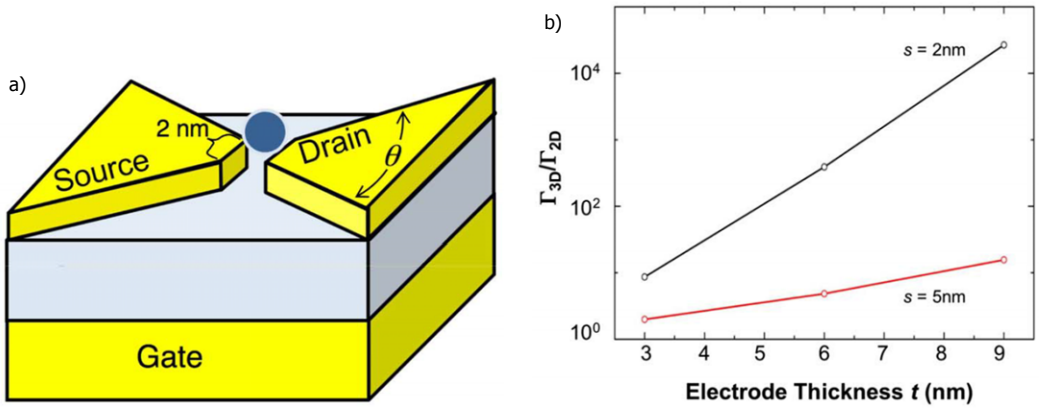

Figure 1.9: Finite element simulations show that the gate coupling strongly depends on the geometry of the leads i.e. the shaper the apex angle, θ (a) of the contacts, the larger the coupling. (b) The difference in gate coupling (expressed by the ratio) between a 3D system (θ = 120∘) and a 2D system (θ = 180∘) increases with the thickness of the contacts. (Extracted from [23])

swing can be achieved as is shown in the work of Pekola et al. [117]. Figure 1.10a shows a SEM image of an electromigration junction equipped with a lateral gate situated ~80 nm from the junction. In the second type of device we use an on-chip large area parallel plate capacitor between the AC gate electrode and DC gate electrode (figure 1.10b), emulating a bias tee element. The capacitive coupling acts like a high pass filter. To ensure a good signal transmission down to 1 MHz we need a sufficiently large capacitance (~ 100 pF). Here we benefit from the already present thin gate oxide which acts as a dielectric spacer between the two capacitor plates which gives us the required capacitance.

In the first approach the lateral gate directly modulates the electro-chemical potential of the island. The coupling is generally weak, and might be even weaker in our case, since the source and drain electrode shield the small island. In the latter case we actually modulate the potential on the local back-gate. Since the back gate is strongly coupled to the island, this approach ensures a good RF modulation of the electro-chemical potential of the island and is therefore our preferred method.

1.4 Gold nano-particle deposition

In the last step before mounting the sample in the cryostat we deposit gold nano-particles on the devices. We do this unlike others [83], before the formation of nano-gaps by electromigration. The contacts to the nano-particles are made of aluminium because of its superconducting property. But like any superconductor aluminium will oxidize if it is exposed to air, which results in poor tunnel junctions. The formation of the nano-gaps by in-situ electromigration ensures pristine and unoxidized gap edges which

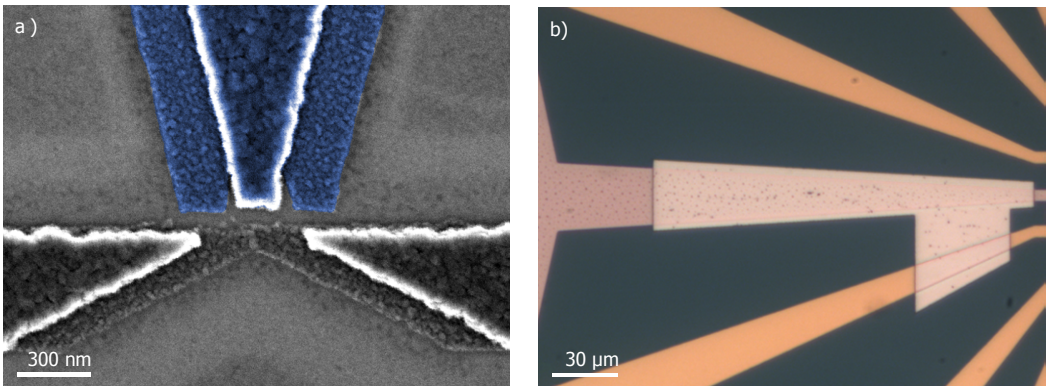

Figure 1.10: a) Scanning electron microscope image of lateral gated junction. As to obtain sufficient coupling to the island, the gate electrode (blue) must be located close to the island. The asymmetric shape of the electromigration junction (pink) is optimized such that the spacing can be decreased to about 80 nm. b) Optical image of the on-chip bias-tee element, which is obtained by a large area structure on top of the gate. The Al_2O_3 layer deposited by ALD acts as a thin dielectric spacer between the gate and the structure on top. Together the system forms a large area parallel plate capacitor ($C \approx 160\,pF$).

are necessary for electron tunneling between gold nano-particles and the contacts.

The deposition of nano-particles is, regardless whether done by metal evaporation [125, 11], growth [12], self assembly [83] or drop-casting [150], a random process. However, with some techniques it is possible to control the particle density and dispersion uniformity. In the course of this thesis we have studied the dispersion properties of three deposition techniques i.e. (1) self assembling nano-particles, (2) spincoating and (3) dropcasting. While the two latter techniques are rather straightforward and will be shortly discussed hereafter, the self assembly of a gold-nanoparticle layer is more complicated and will be discussed in detail in section 1.4.

Both techniques, spincoating and drop-casting[2] are based on the fast evaporation of the nano-particle solvent such that the nano-particles cannot locally congregate (for example at a meniscus). The resulting nano-particle density is however also lower as most of the dispersion is lost in the process. It is therefore necessary to repeat the process several times in order to get sufficiently high particle densities. To further maximize the evaporation of the dispersion we have selected gold-nanoparticles (Nanocomposix NanoXact) that can be re-dispersed in toluene (50 ng/mL), which is highly volatile. These gold nano-particles have a diameter of $\sim 5\,nm$ and are functionalized with dodecanethial molecules. The nano-particles are functionalized with spacer molecules to prevent them from congregating in the solution. Additionally they naturally create a spacing (tunnel junction) between the nano-gap contacts and the gold nano-particles.

Figure 1.11 shows the gold-nanoparticle distributions on the substrate after spin-

[2]In drop-casting a small droplet ($10\mu L$) of nano-particle dispersion is placed on the chip which will be fast dried using a nitrogen gun

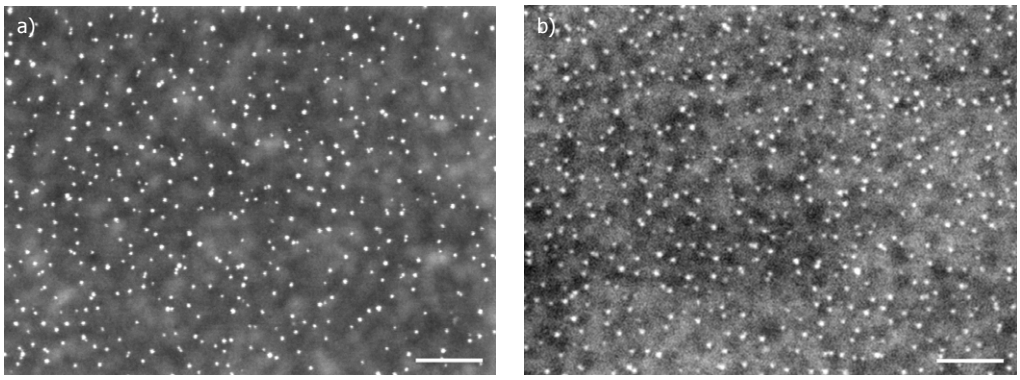

Figure 1.11: Scanning electron microscope images of gold nanoparticles (5 nm) distributed on a substrate after spincoating (a) and drop-casting (b). Under equal conditions the drop-casting technique gives better results than spincoating. The scale-bar in both images represent 50 nm.

coating and drop-casting 10 droplets of $\sim 10\,\mu$L. Although the particle distribution after spincoating looks nicely homogeneous and dense on the substrate, there are actually little nano-particles distributed on top of the electromigration junctions. We do not see such a difference in particle density after drop-casting which makes it the superior deposition technique.

The self assembling monolayer approach

While the drop-casting of gold-nanoparticles works very well, it does have several shortcomings i.e. (1) the particle size has an upper limit of 5 nm and (2) the dodecanethial molecules are very large (about 2 nm). The origin of both limitations is the tendency of nano-particles to aggregate when they are dispersed in a solution. Because the gold nano-particles do not carry an electrical charge, relatively long molecules are necessary to sterically stabilize the suspension.

Another solution is to cover the gold-nanoparticles with an organic acid like citric acid. In suspension the conjugate base caps the nano-particles and gives them an effective charge, making the dispersion more stable. Such gold nano-particles dispersions are commercially available and can be made by the recipe of Frens [37]. In addition to the increased stability of the suspension, the effective charge on the nano-particles can conveniently be used in combination with self assembling monolayers as will be explained in the following.

The self assembling process (figure 1.12) of nano-particles begins with the self assembly of a specific molecule on the substrate. The molecules typically contain a silane group on one end, and an amine group on the other. During a process called silanization (figure 1.12b), the silane group preferentially attaches to the substrate, replacing -OH groups. The result is a highly dense self assembled monolayer (SAM) of molecules with

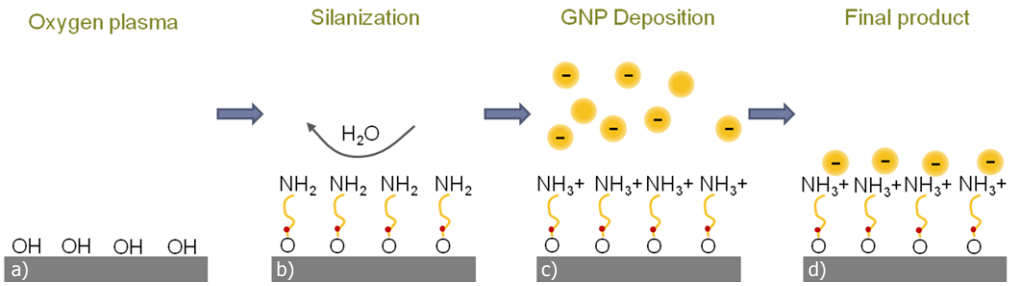

Figure 1.12: A schematic representation of the creation of a dense layer of gold nanoparticle using a self assembling monolayer. First the substrate is cleaned and activated with an oxygen plasma (a) after which APTES molecules self assemble on the substrate (b). Next the substrate is placed in an aqueous gold nano-particle suspension which contains negatively charged nanoparticles (c). The positive change on the substrate attracts the nano-particles where they immobilize (d). The process ends when the attractive force is counterbalanced by the Coulomb repulsion between nano-particles.

their anime group oriented away from the surface. Due to the high affinity of amine towards gold, the nano-particles will get easily immobilized on the surface. Moreover, when the substrate is placed in an aqueous solution, the protonation of the amine groups give the surface a tunable positive surface charge (figure 1.12c), effectively attracting the negatively charged gold nano-particles to the substrate (where they get immobilized). The attractive force of the substrate will be counterbalanced by the Coulomb repulsion between nano-particles and the self-assembly process stops when the two forces balance each other. Figure 1.13a shows the speciation curves of citric acid and APTS as a function of the acidity of the solution. The protonation of APTS can be fully tuned by the pH of the solution. For low pH ($pH \ll pK_{1/2}^{APTES}$) the APTES is fully protonated and will create a maximum positive surface charge. However there is a lower boundary to the pH given by the iso-electric point of citric acid ($pH \approx 2$) i.e. when the gold nano-particles loose their effective charge, and the suspension becomes unstable and turns black.

In various works (e.g. [83]) the self assembled monolayer of amine groups is formed by inserting the sample in an aqueous solution of N-[3-(trimethoxysilyl)propyl] ethylenediamine (APTS), after which it is rinsed and baked at 120°C. Next, the sample is placed in an aqueous gold nano-particle dispersion for 24 hours to deposit the gold nano-particles. Here we show the results of a similar process which only takes about 1-2 hour. First we place the sample in a plasma chamber equipped with mass-flow controllers (Diener Electronic Nano) to form the self assembled monolayer. This process contains two steps: (1) we activate the surface with a short oxygen plasma after which (2) we introduce a controlled flow of gaseous (3-Aminopropyl)triethoxysilane (APTES) in the chamber during 5 minutes while the substrate is heated to 80°C. Finally the sample is put into the aqueous gold nano-particle dispersion for 15-30 minutes after which it is thoroughly rinsed with DI water.

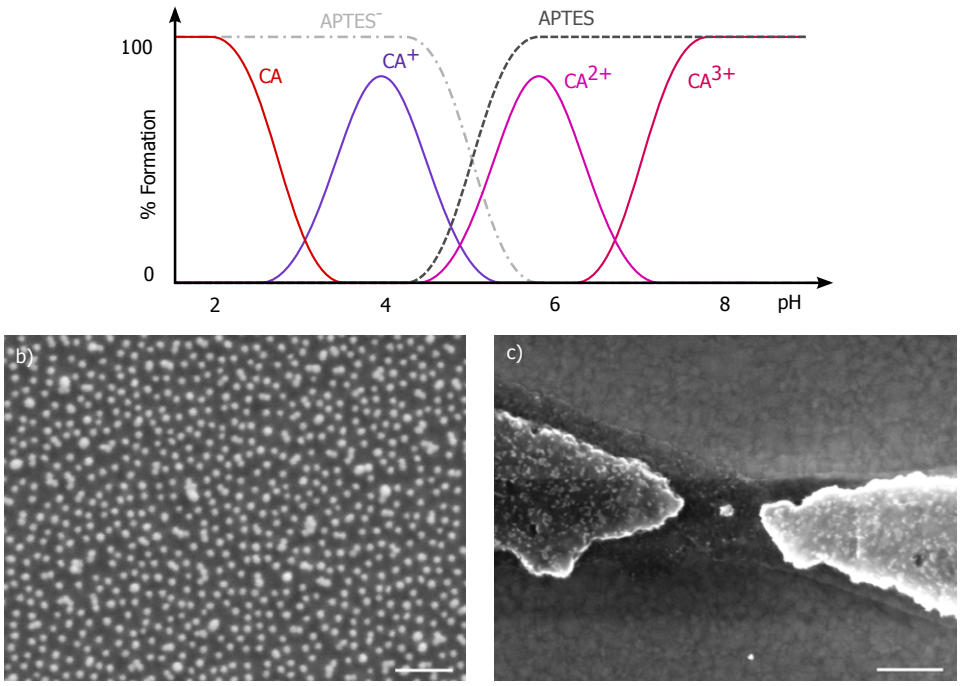

Figure 1.13: a) Speciation curves of APTES and citric acid (CA) as a function of the solution pH give the percentage of formation in a solution. b,c) Gold nano-particles deposited using the APTES self-assembly process with two solution acidities. A low solution pH (2-3) results in a dense GNP distribution (b), while a neutral pH (7) leaves APTES uncharged which results in a low density (c). Scale bar represent 100 nm.

Figure 1.13 shows the surface distribution of nano-particles after identical deposition processes with different dispersion acidities (pH = 2 and pH = 7). The difference in particle density is the direct effect of the solution acidity. A high pH solution (figure 1.13c) minimizes the positive surface charge while it maximizes the Coulomb repulsion between gold nano-particles. We have found that the best results in terms of high particle density and reproducibility are obtained when the nano-particle solution has a pH between 3 and 4. More acidic dispersions do not result in higher densities, but do result in an increased occurrence of clustered particles.

To obtain the best results with our silanization technique, we have studied the nano-particle surface distributions for various combinations of the silanization parameters. The strong effect of the dipersion acidity is eliminated by using a single solution stock with pH 4. We have analysed SEM images by visual inspection and automatic particle recognition. The latter technique allows us to extract for each particle the distance to its n closest neighbours. Figure 1.14 shows the nano-particle surface distribution when varying the plasma time (a, b, c) and APTES dose (d, e, f).

We find no significant effect of the oxygen plasma time on the nano-particles surface distribution. More interesting is the effect of the APTES dose. Increasing the dose

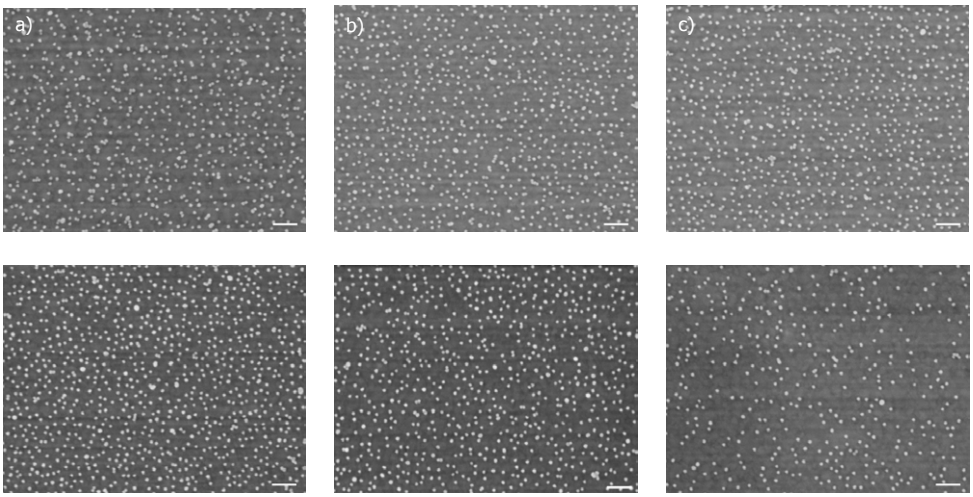

Figure 1.14: Scanning electron microscope images of gold nanoparticles (12 nm) deposited using a self assembling monolayer created with varying silanization parameters. The oxygen plasma time (a, b, c) (APTES dose = 4 sccm) plasma time has little significant effect on the particle density. However with increasing APTES dose (d, e, f) (plasma time = 30 s) their appears to be a little decrease in particle density. The scale bars represent 100 nm.

GNP time	15 min	30 min	60 min
R(before) [Ω]	124	124	124
% ($R < 10\,\mathrm{k\Omega}$)	37.5	35.4	12.5
R(after) [Ω]	1568	2177	3333

Table 1.4: The SAM based gold nano-particle deposition technique has a devastating effect on the electromigration junctions. After the process less than 40 % of the junctions have a resistance lower than 10 $R < 10\,\mathrm{k\Omega}$. Of these junctions the average resistance is more than 10 times higher then before the deposition of gold nan-particles.

beyond a critical value (4 sccm) results in the decrease of particle density. This is probably due to free APTES in the solution that binds to gold nano-particles, but will be rinsed away later on. In addition to the plasma time and APTES dose we have optimized various other silanization parameters.

With the little effect that the silanization parameters have of the surface distribution, one can legitimately raise the question whether the APTES SAM is necessary at all. To answers this question we have studied the contribution of the APTES SAM on the deposition process. Six samples, of which half received the optimized silanization treatment, were placed in the gold nano-particles dispersion for 15, 30 and 60 minutes. Figure 1.15 shows the resulting nano-particle surface distributions. The samples that have the APTES SAM consistently have a higher nano-particle density (7-65 %) and the distribution looks more homogeneous. However for increasing time spend in the gold nano-particle dispersion, the difference in particle density become less.

Directly after the gold nano-particle deposition we have characterized our electromi-

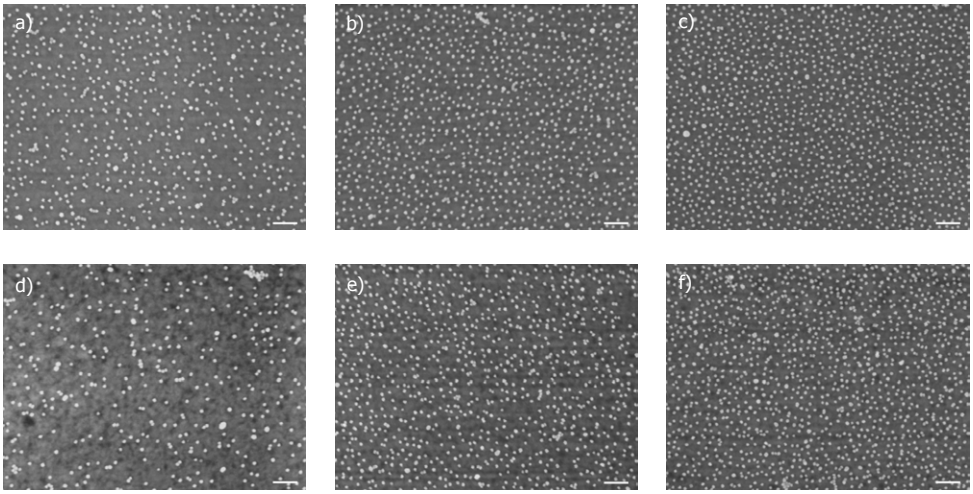

Figure 1.15: Scanning electron microscope images of gold nanoparticles (12 nm) deposited with (a, b, c) and without (d, e, f) the use of a self assembling monolayer and during a varying time in a gold nano-particle suspension. Overall the particle dispersion of the samples with a self assembling monolayer have high particle density and are more homogeneous. However the difference in particle density becomes less when the time spend in the gold nano-particles suspension increases.

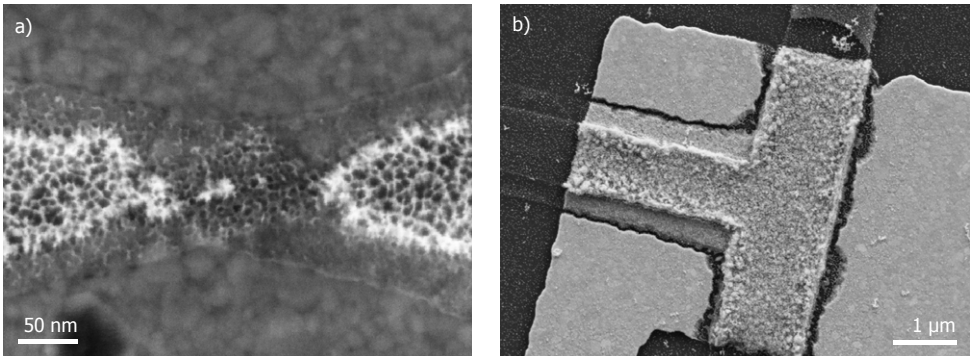

Figure 1.16: The aqueous gold nano-particle solution has a detrimental effect on the aluminium electromigration junctions. (a) The scanning electron microscope image of the electromigration junction shows that the ionic environment attacks and partly dissolve the aluminium. (b) At the connection between the aluminium junctions and the gold contact leads the two metals interact, possibly forming an intermetallic compound. This process is possible enhanced by the ionic environment.

gration junctions by measuring their resistance and by optical inspection. In table 1.4 we summarize the device characterization by showing the percentage of junctions with a low resistance ($R < 10k\Omega$) after GNP treatment and their average resistance before and after GNP treatment. It is clear that gold-nanoparticle deposition by self assembly is not compatible with aluminium electromigration junctions. The reason for the large increase in resistance and the low survival rate is twofold. First the aluminium junctions get attacked in the ionic solution and partially dissolve (see figure 1.16a) which increases their resistance. Second, at the connection between the optical and electron beam lithography, the gold and aluminium interact (see figure 1.16b), possibly forming an intermetallic compound known as white or purple plaque. Without exactly knowing what it is, it is not unreasonable to expect that this causes the low survival rate of the devices.

Unfortunately we have to conclude we can not use this SAM approach with our aluminium electromigration junctions. The SAM technique allows us to fabricate high quality gold-nanoparticle layers of controlled particle density. However it also dramatically decreases the quality of our junctions making them unfit for electromigration.

1.5 Nano-gaps by electromigration

Electromigration (EM) is often utilized to contact molecules [111, 150, 105] because of its easy process, decent success rate and compatibility with a local back-gate. In addition to these raison d'tre, electromigration also allows one to make nano-gaps in-situ. As the surface of any superconductor will oxidise when it is exposed to air, it is important in our devices that the actual tunnel junctions to the gold nano-particles are created and maintained in vacuum. Like this, the ligands on the gold nano-particles form the only barrier between pristine leads and the quantum dot. Therefore electromigration is our designated method for making the nano-gaps to contact gold nano-particles.

Before it was ever used in molecular electronics, electromigration was already known as the cause of interconnect failures in micro-electronic devices [51]. At sufficiently high current densities ($\sim 10^8 A/m^2$) the transfer of momentum from electrons to atoms can result in atomic motion and eventually the breaking of an electrical wire. Park *et al.* [110] were the first that utilized this principle to make nano-gaps. Nano-sized junctions made by shadow evaporation were simply biased with an increasing current while measuring the voltage drop. After breaking they could measure tunnel resistances ranging from 10^5 to 10^{12} in 85 % of the devices indicating a gap-size of about 1 nm. Since this first application of EM to produce nano-gaps, various groups have adopted and improved the electromigration process. Currently different techniques exist among which are active feedback controlled systems [139] and 4 probe EM setups [153]. In section 1.5.1 some of the existing techniques will be discussed, including the method

that we have used. Most electromigration measurements published up to now were actually performed on devices made of gold or platinum. It is believed that these two materials, both not a superconductor, are best used for electromigration because of there noble character and large atomic mobility. However there are examples where electromigration is performed on lead [92] and aluminium [150] electromigration junctions. Since we do need the leads in our devices to be superconducting and there is local experience with aluminium electromigration junction, we have chosen to use aluminium. To illustrate the compatibility of aluminium with EM we show in section 1.5.2 the results of electromigrations performed on 128 aluminium nano-junctions. The high reproducibility in break-voltage and current indicates the compatibility of aluminium with electromigration.

1.5.1 Electromigration procedures

During a traditional electromigration process, electrons driven by an electric field inelastically collide with the atoms in the material, effectively transferring momentum. The process was described by Trouwborst et.el [145] using the thermodynamics of irreversible processes [48]. By ignoring any thermodiffusion and assuming zero difference in electrochemical potential of the electrons, the mass flux due to the atoms is given by:

$$\mathbf{J_m} = -\frac{L_{m,m}}{T}(\nabla \mu^m - Z^* e \rho j) \tag{1.1}$$

where μ^m is the electrochemical potential of the atoms, $L_{m,e}$ and $L_{m,m}$ are phenomenological constants and Z^* is considered as an effective charge of the atoms:

$$Z^* = Z - \frac{L_{m,e}}{L_{m,m}}. \tag{1.2}$$

Note that the second term in the parenthesis in eq. (1.1) is force due to the electrostatic field i.e. $\mathbf{F}^* = eZ^*\mathbf{E}$, and can be decomposed into two parts by using eq. (1.2):

$$\mathbf{F}* = eZ_{es}\mathbf{E} - eZ_{wind}\mathbf{E}. \tag{1.3}$$

Hence the atoms in the metal experience two forces, both determined by the current density: (1) the normal electrostatic force due to the electric field and a second force, the so called 'electron wind' due to the imparting electrons. Since often the electron wind is much larger than the electrostatic forces, the atoms move in the direction of the electrons.

Although this model results in a nice short equation illustrating the driving force behind electromigration, it does not show the dynamics of the EM process. In addition to a high current density also a minimum atomic mobility is required. Because the

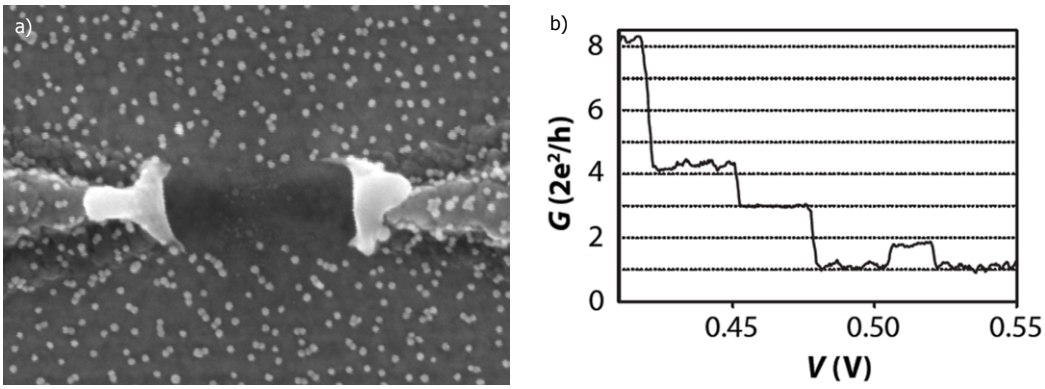

Figure 1.17: (a) A scanning electron microscope image of a fused electromigration junction. When during electromigration the local temperature becomes too high the process spins out of control and the junction 'explodes'. (b) When the electromigration process develops controlled and without excessive heating the junction conductance steadily decreases until it becomes quantized just before it enters the tunnel-regime. (extracted from [127])

atomic mobility is (exponentially) dependent on the local temperature one can expect a critical temperature at which the atomic mobility is high enough and the electromigration process will start. Unfortunately, once the process is started the local temperature can continue to increase due to increased Joule heating and when the temperature becomes too high the wire may actually fuse violently (see figure 1.17). Therefore a good control of the local temperature (or power dissipation) during electromigration is essential, which turns out to be a challenging problem.

In the work done by Park *et al.* [110] the electromigrations were performed on bow-tie shaped wires made by ebeam lithography and shadow evaporation. This allowed the authors to create the small junctions (200 nm wide and 10 nm thick) necessary for high current densities, while maintaining a small access resistance. The nano-wires were electromigrated by means of a slowly increasing current bias until breaking point. In this situation, during the electromigration the Joule heating of the junction $P_J = I^2 R_J$ will increase as the junctions cross-section decreases and its resistance increases. It would be better to voltage bias the junctions since at constant voltage the Joule heating $P_J = U^2/R_J$ will decrease with increasing junction resistance [153].

To further improve control over the electromigration process Strachan *et al.* [139] developed a method that gradually breaks the junction during successive voltage ramps. While increasing the voltage bias, the junction conductance is monitored. Whenever the conductance has decreased with a setpoint percentage, the voltage is quickly lowered by 100 mV, after which a new voltage ramp is started. With this method Strachan *et al.* are able to measure a quantized conductance just before the junction resistance enters the tunnelregime. It has been shown that this feedback controlled method actively regulates the temperature such that the electromigration occurs at constant temperature

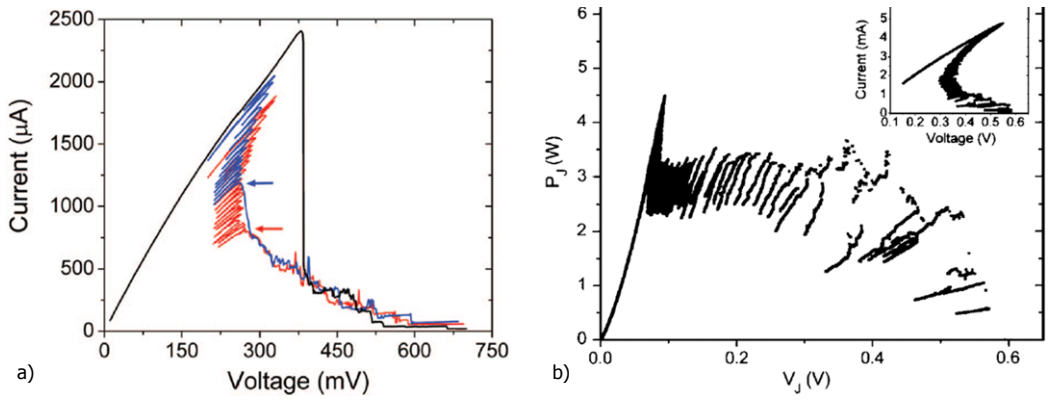

Figure 1.18: The feedback controlled electromigration process developed by Strachan *et al.* [139] gradually break the junction during successive voltage ramps. (a) Whenever the feedback system is disabled in the bistable region the current will not follow the constant power curve. Instead it will drop quickly to the lower current branch (black trace). (b) The onset of electromigration during such a process follows a constant power curve which indicates there is a critical temperature at which the electromigration process starts. (Figure are extracted from [32])

[32] (see figure 1.18b).

As stated before, when voltage biased, the electromigration process will take place with decreasing power dissipation and will auto-stop whenever the dissipated power does not heat the junction beyond this critical temperature. This self-limiting behaviour removes the necessity of the time consuming feedback controlled system. This is only valid however when the total circuit resistance in series with the junction is smaller than the junction resistance (typically 10-30 ohm). In case this condition is not satisfied, the series resistance (R_S) creates a bistable branch in the I(V) curves of constant junction power as is shown in figure 1.19a for two values of R_S. This can easily be understood by expressing the total dissipated power in terms of a constant junction power ($P_c = I^2 R_J$) as is done in eq. (1.4).

$$I^2 R_S + P_c = I V_T \tag{1.4}$$

It is clear that this equation will have two solutions whenever $V_T > 2\sqrt{R_S R_T}$, where V_T is the voltage over the complete circuit. In the belly of the bistable branch, when $V_T = 2\sqrt{R_S R_T}$, the current is single-valued ($I = \sqrt{P_c/R_S}$), and the resistance of the total system is $2R_S$, indicating that at this point R_J is equal to R_S. To exemplify the condition for bi-stability one can again use eq. (1.4), this time expressing the constant junction power in terms of the junctions resistance and voltages i.e. $P_c = V_J^2/R_J$. It can be easily verified that this equation only has single-valued solutions when $R_J > R_S$.

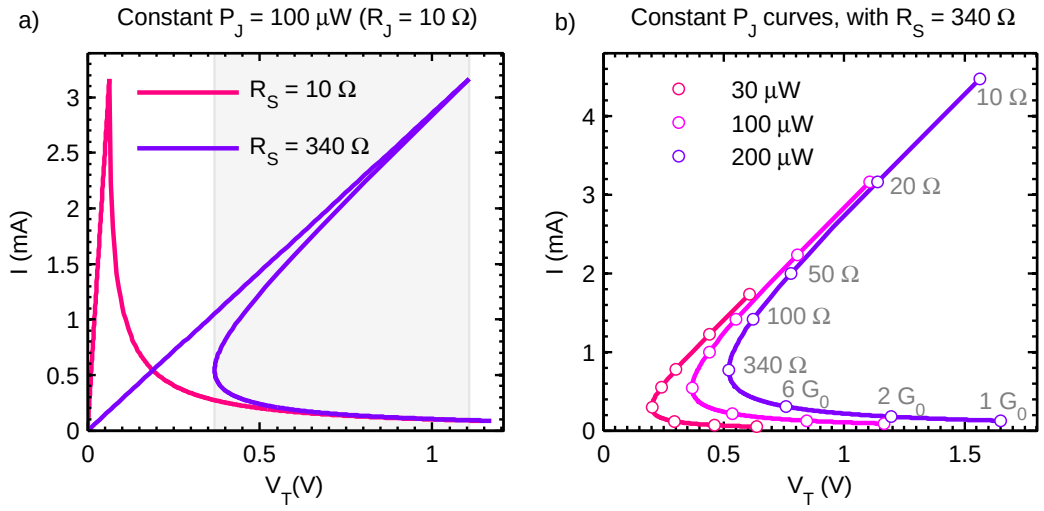

Figure 1.19: (a) When there is a resistance in series with the electromigration junction, for which $R_J < R_S$, the $I(V)$ curves for constant junction power become bistable within a certain voltage regime (grey region). (b) Along the $I(V)$ curves for constant junction power the junction resistance increases from its initial value into the tunnelling regime as is pointed out by the open circles. Note that at the belly of the bistable region the junction resistance equals the series resistance.

$$I^2 R_S + 4\frac{R_S}{R_J}\left(\frac{R_J}{R_J + R_S}\right)^2 V_T^2 = IV_T \tag{1.5}$$

In figure 1.19b the $I(V)$ curves with constant P_J are plotted for three different powers. Along the curves the junction resistance increases from its initial value into the tunnelling regime as is pointed out by the open circles. Equivalent $I(V)$ curves are traced out during a feedback controlled electromigration, indicating that the feedback system actively bypasses the bi-stability induced by $R_S > R_J$. Moreover, since with the feedback controlled electromigration measurements the EM onset follows the constant power $I(V)$ curves (see figure 1.18), one can conclude that electromigration starts at a critical power (that is, local temperature).

It was first shown by Esen *et al.* [32] and later by Trouwborst *et al.* [145] that the active feedback system is indeed only required when the series resistance in the circuit is larger then the junction resistance. When electromigration is executed in this regime without the feedback system the percentage of samples with a measurable resistance after EM decreases with increasing series resistance. The origin of this decreasing yield can be understood by considering the dynamics of this electromigration process. Before the electromigration starts, the majority of the applied voltage drops over the series resistance. However when the electromigration begins (i.e. when the junction is heated up to the critical temperature) the increase in R_J causes the voltage drop over the junction to increase, thereby increasing the local Joule heating and thus the

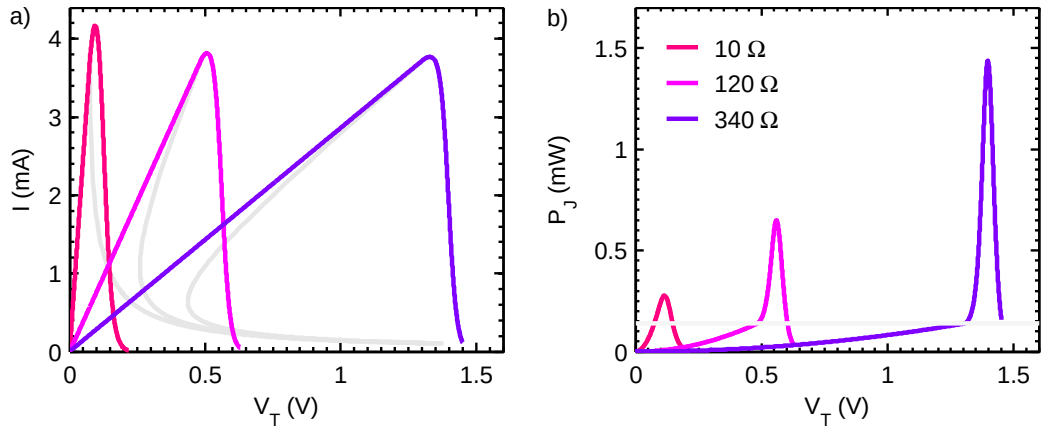

Figure 1.20: Calculated $I(V_T)$ (a) and $P_J(V_T)$ (b) curves for different R_S (10, 120 and 340 Ω) using our simple model given by eq. (1.6). (a) The $I(V_T)$ curves (colored) show the typical current drop when the electromigration process starts. Note that in the case of $R_S = 340\,\Omega$ the current drop extends beyond the end of the iso-power line. (b) Due to the increase in R_J, the applied voltage will be located more and more over the junction. This voltage increase causes a temporary increase of dissipated power P_J.

electromigration speed. The result can be a thermal run-away with disastrous outcome [145].

Although it is impossible to simulate an actual electromigration we can illustrate the effect of a large series resistance by assuming an arbitrary time profile for the junction resistance. More precisely, we model the junction resistance by:

$$R_J(t) = \begin{cases} R_0 & P_J(t) < P_c \\ R_0 + \mathrm{e}^{\alpha(t-t_c)} & P_J(t) > P_c \end{cases} \tag{1.6}$$

where t_c is the time when the power dissipation in the junction becomes higher than the critical value P_c. By using this junction resistance profile and assuming a slowly increasing applied bias voltage ($\dot{V}_T = 30 mV/s$) we can calculate the power dissipated in the junctions during the electromigration. In figure 1.20 we show the resulting $I(V_T)$ and $P_J(V_T)$ curves for three different values for R_S. In these calculations we have used the following values: $R_0 = 10\,\Omega$, $P_c = 140\,\mu$W and $\alpha = 2.5\,\Omega$/t. Figure 1.20b shows that for increasing R_S the burst of dissipated power just after the start of electromigration becomes larger, even though the current through the junction decreases. When the power dissipated in the junction becomes to large (i.e. $P_J < P_F$), the local temperature can increase up to the melting point of the metal and the junction will be fused.

In the calculations above we have (for graphical purposes) taken an unrealistically low value for the time constant α, which is the reason why also in case of $R_S = R_0$ the dissipated power shortly continues to increase after the onset of electromigration. When we use a more realistic time constant i.e. $\alpha = 100\,\Omega$/t we find that the maximum power

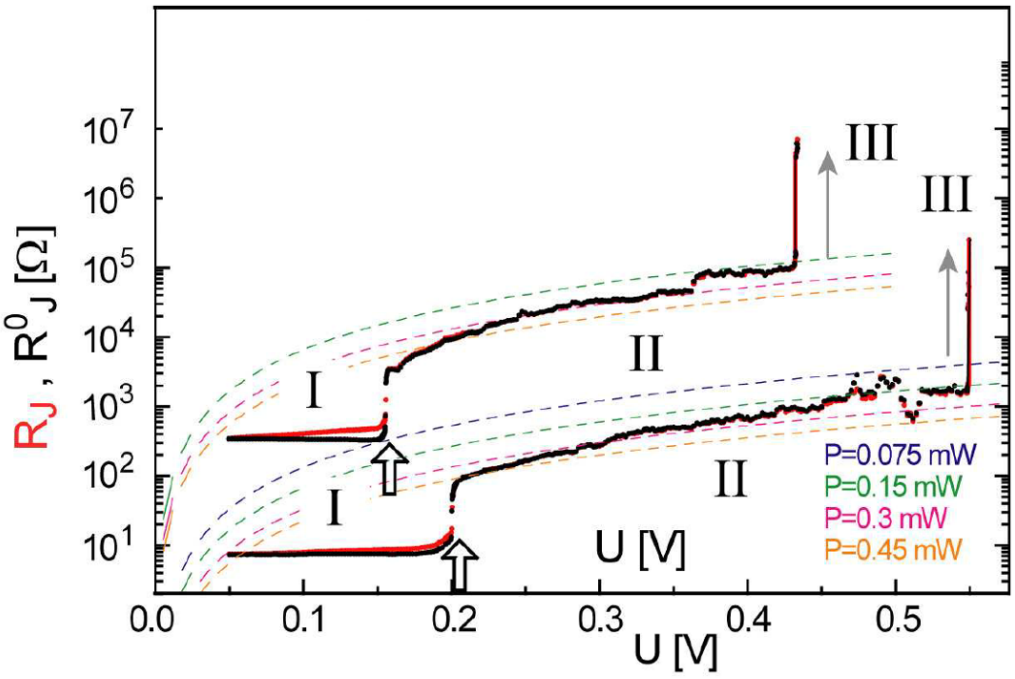

Figure 1.21: By using a four probe measurement setup, Wu *et al.* where able to measure the junction resistance during electromigration (R_J) and at zero bias (R^0_J) at any time during the eelctromigration process. (a) During the process three regimes can distinguished. In the first regime (I) the resistance increase of the junction is only due to local heating (R_J increases while R^0_J stays constant) i.e. the electromigration process has not been started yet. The second stage (II) starts with a sudden increase of both resistances, after which they become equal. During the second regime (the electromigration process) both resistances slowly continue to increase while the dissipated power in the junction slowly decreases. Actually R^0_J becomes a bit larger than R_J, which indicates the transport becomes quasi-ballistic. In the third regime (III) both resistances jump into the tunnelregime and electromigration ends. (Extracted from [153])

reached during electromigration decreases linearly with decreasing series resistance until it saturates at the critical power for $R_S < R_0$, proving the auto-limiting property of electromigration when R_S is smaller than R_J.

When during electromigration the power dissipated in the junction stays below P_F the process might be very violent but remains controllable. When the electromigration begins, the current rapidly drops until the lower branch in the bistable regime is reached and electromigration process slows down. This can be seen in figure 1.18. Sometimes the bi-stable regime actually extends over all junction resistances below $1/G_0$, and when the electromigration starts, it will quickly end with R_J vastly in the tunnelling regime. Of course we can not see this in our simple model since we assume a certain junction resistance profile.

It is now clear that a significant series resistance can make a controlled electromigration nearly impossible. Unfortunately it is not always possible to reduce R_S below the junction resistance, especially in cryogenic setups where extensive filtering is required.

Instead of using the time consuming feedback controlled electromigration process, one can also perform the electromigration in a four probe configuration [3] as presented by Wu et.al [153]. The samples is voltage biased by one pair of leads, while the voltage drop of the junction is measured with the second pair. A fast feedback system regulates the applied voltage such that the measured voltage drop over the junction slowly and uniformly increases, thereby effectively bypassing the effect of any series resistance. This approach on electromigration allowed Wu et.al to measure the difference between the equilibrium resistance (zero bias) and active resistance of the junction during the electromigration process (see figure 1.21). Their measurements confirm (1) the existence of a critical temperature to start electromigration and (2) the decrease in dissipated power during the electromigration process. Furthermore the measurements indicate the existence of a quasi-ballistic regime during the electromigration process, which can be expected when the effective size of the junction becomes less then the inelastic scattering length.

In conclusion, the controlled electromigration process passes through 3 phases. Initially the junction will be Joule heated until it reaches a critical temperature (typically 400 K) and the electromigration is triggered. Once started the process will evolve with decreasing power dissipation and reaches a quasi-ballistic regime. Finally the junction resistance makes a jumps as the nano-gap is formed. To achieve this course, electromigration can be performed best by applying a slowly increasing voltage bias provided that the series resistance in the circuit is less than the junction resistance. When it is not possible to fulfil this latter condition (e.g. in cryogenic setups), one can resort to active feedback systems as presented by Strachan *et al.* and Wu *et al.*

1.5.2 Our approach

Low temperature transport measurements, especially electron pumping experiments [116], generally requires significant filtering on the measurement lines which inevitably increases the series resistance in a cryogenic setup. Performing a slow and controlled electromigration is in such a situation impossible unless one uses one of the active feedback systems discussed in the previous section. But since we are using 5 nm gold nano-particles, we actually need a fierce (but controlled) electromigration such that the resulting gap will be large enough to fit the particle. A large series resistance can therefore be beneficial to our needs.

To break our nano-wires, we apply a slowly increasing voltage bias over the junction while simultaneously measuring the current (see figure 1.22a). A fast feedback algorithm (developed in the lab by E.Bonet, C. Thirion and R. Picuerel), executed by an

[3] Measuring samples in a four probe configuration is a well known technique to remove the resistance contribution of the junction leads and measurement lines

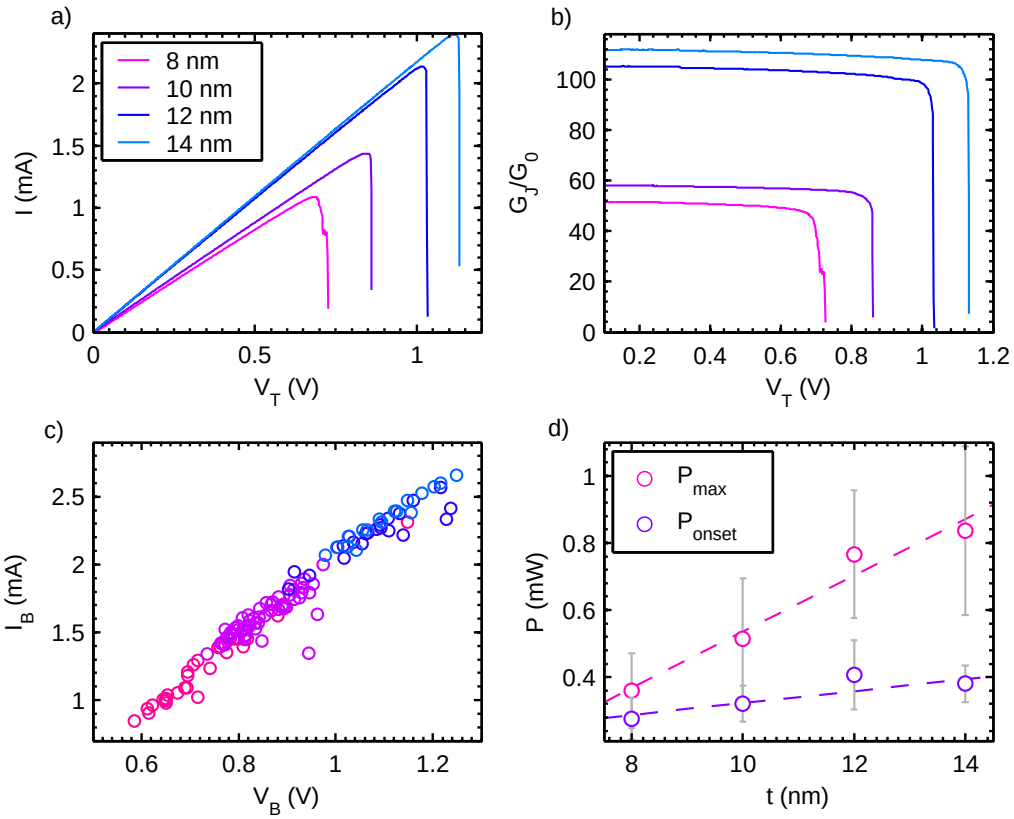

Figure 1.22: (a, b) The $I(V)$ (a) and $G(V)$ (b) traces of 4 (out of 128) selected electromigrations of aluminium junctions with varying thickness (8, 19, 12 and 14 nm). In none of these device we have observed the quantization of conductance. (c) The $I(V)$ points at the onset of electromigration of 128 junctions. With decreasing junction thickness the electromigration starts at lower voltage and current. (d) The extracted maximum power during electromigration (pink circles) and the power at the onset of electromigration (purple circles). The dotted lines are a linear fit based on the four data point.

ADwin ProII, evaluates the conductance (figure 1.22b) of the system and puts the bias voltage to zero as soon it detects a conductance below an arbitrary threshold value. Due to the fast electronics we can stop the electromigration process within $10\,\mu s$ which is faster than our typical electromigration process ($40\,\mu$s as deduced from the number of measured points after the onset of electromigration). However this method does not remove the bi-stability caused by a large series resistance like any of the feedback systems discussed above. Since we do have a significant line resistance in our cryostat ($170\,\Omega$), we need to take special care to prevent excessive heating in our junctions during the electromigration process. This can be done by a proper design of the nano-wires as will be explained below.

In previous section we have shown that during the electromigration process the dissipated power in the junction increases due to the increase in voltage over the junction as its resistance increases. The amount by which the junction voltage increases is given by $I_c R_S$, where I_c is the current present at the start of the electromigration process. This critical current is determined by the local dissipated power necessary to heat the junction beyond the critical temperature such that the electromigration process is triggered. It can therefore be reduced by either increasing the electrical resistivity of the junction or by decreasing the critical power. The latter can be achieved by decreasing the junction cross-section area which reduces the heat transport out of the junction through the leads. Figure 1.22c shows the current (I_c) and total voltage (V_B) at the onset of electromigration of junctions with different thickness. A clear increase in I_c with increasing junction thickness is visible, especially for the devices with a lower thickness. At the onset of electromigration the junction resistance is still small which implies that the total voltage (V_B) at this point is nearly equal to $I_c R_S$. The increase in V_B with increasing junction thickness therefore indicates that the amount by with the dissipation increases during electromigration increases with increasing junction thickness. This is confirmed by figure 1.22d which shows the measured power dissipated in the junction at the onset of electromigration (purple data points) and the maximum during electromigration (pink data points). The increasing difference with thickness indicates an increase in dissipation during electromigration with increasing thickness. Moreover, the increase in the dissipated power at the onset of electromigration (purple data points in figure 1.22d) shows that the dissipation at the onset of electromigration is indeed proportional to the thickness of the junctions. In conclusion, the use of junctions with a very small cross-section area (typically 100 nm wide, and 8-14 nm thick) made out of aluminium allows us to prevent excessive heating during our electromigration process.

In all electromigrations that we have performed in our cryogenic setup, we have never seen conductance quantization like other groups [139, 105, 18]. This is not surprising since our total line resistance ($340\,\Omega$) is very large. However, this does not

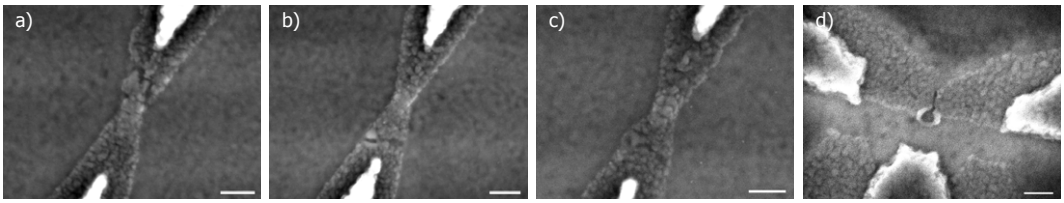

Figure 1.23: Scanning electron microscope images of aluminium junctions after electromigration. Often it is difficult to observe the nano gap, even by SEM.

exclude the controlled formation of large nano-gaps. Figure 1.23 show SEM images of some nano-gaps after electromigration. The gaps are well defined and often show little signs of the fusing effect. After electromigration over 95 % of the junctions show tunnel-currents with a zero-bias resistance between 100 kΩ and 10 GΩ. This high succes rate and small variation in break voltage show we can create aluminium electromigration junctions with a high reproducibility.

Chapter 2

Cryogenic transport setup

The electron transport measurements presented in the following chapters are all conducted in a highly filtered inverted dilution cryostat. In this chapter we will shortly discuss the cryogenic operation of our dilution refrigerator, after which we will focus on the electronic wiring. As to acquire a low-noise electronic setup, compatible with the electro-migration technique electro-migration, we designed and installed a double-shielded sample cavity and measurement wires.

Chapter contents

Experiments with mesoscopic or quantum devices generally require cryogenic temperatures and a low noise electrical environment. Most experiments deal with small electrical signals can be drowned easily by electrical noise. Johnson-Nyquist thermal noise is reduced by measuring at low temperatures. To remove the remaining noise (e.g. external radiation sources and thermal radiation from the hotter parts in the cryostat) a careful design of the electronic setup is necessary. The cryogenic temperature is in our experiments further required in order to put the aluminium leads in our samples in a superconducting state.

At the beginning of my thesis I inherited an old 'inverted' dilution cryostat (Sionludi) originally wired for STM experiments. After removal of all electronic wires (except the thermometry wires), we have installed a new sample stage, a three-axes magnetic coil and low noise wiring compatible with in-situ electromigration. First I will shortly discuss the cryogenic operation of the dilution refrigerator after which we continue with the electronic wiring and filtering.

2.1 Cryogenic operation of a Sionludi

The Sionludi (a verlan for dilution) is an a-typical dilution refrigerator designed and fabricated locally (Institut Néel, Grenoble). While normally a dilution refrigerator is inserted top-down into a liguid ^{4}He bath, the Sionludi is mounted on top of a liguid ^{4}He tank. The peculiar design offers a fast cooldown time and a spacious and easily accessible experimental stage, especially convenient of cryogenic AFM/STM experiments. As the refrigerator is located in a room temperature environment instead of a liguid ^{4}He bath, extensive thermalization and shielding at various temperature stages and a good vacuum are required to minimize the heat load to the cold stage. Moreover, the absence of exchange gas during pre-cooling between the cold stage and a 4K reservoir demand for a alternative precooling method which is achieved by the circulation of mixture through both stills and the mixing chamber as will be discussed. Despite the inverted geometry of the Sionludi, its cryogenic operation is nearly identical to any other dilution refrigerator.

The cryostat (figure 2.1) is positioned inside a large vacuum chamber which is mounted on a table top above a large liquid helium tank. Two separate circuits, a closed ^{4}He/^{3}He mixture circuit (primary circuit) and an open liquid ^{4}He circuit (secondary circuit), cool the inner parts of the cryostat. The ^{4}He circuit provides large 4 K cooling power (~ 4 mW) and essentially replaces the conventional liquid helium bath. Liquid ^{4}He from the underlying tank, which is operated at an overpressure, is pushed up into a reservoir (figure 2.1f) located at the 4 K stage of the cryostat. The cold ^{4}He vapours from this reservoir are passed through a large counter flow heat exchanger (pointed out by the green arrow in figure 2.1a) where they gradually cool the incoming mixture flow

in the primary cooling circuit as well as the hotter stages (~20 K and ~80 K) of the cryostat. The two 'hot' stages are used to position gold plated copper shields necessary to isolate the 4 K stage from thermal radiation.

The ^{4}He/^{3}He mixture in the closed primary circuit cools the cold stages (1K, 200 mK and 50 mK) of the cryostat, initially to 4 K but to lower temperatures when condensing. During the initial cool down from room temperature to 4 K a large ^{4}He flow is passed through the secondary circuit. Simultaneously the ^{4}He/^{3}He mixture is circulated through the primary circuit to cool the 1 K stage and dilution stage to 4 K. A significant mixture flow is necessary since these cold stages are well thermally isolated from the 4 K stage. The primary circuit contains a dedicated part, called fast injection, to pass a large mixture flow directly into the mixing chamber (bypassing still 1) onwards through the primary circuit . Before entering the mixing chamber (figure 2.1d) the mixture from the fast injection line is cooled by the large counter flow heat exchanger (red arrows in figure 2.1d) and is thermalized at the 1 K stage. Once the cold stages are thermalized to 4 Kelvin they can be cooled further by condensing the ^{4}He/^{3}He mixture in the mixing chamber and the stills (figure 2.1b and figure 2.1c). Exact details of this condensation step are well described in the thesis of Norbert Moussy [100]. After condensing, the cryostat (without experimental wiring) will reach a stable base temperature of about 50 mK (80 mK with experimental wiring). In this stage the operation is like other dilution refrigerators and is well described in the thesis of Stefan Thiele [141].

2.2 A low noise electronic setup

Experiments with mesoscopic devices usually involve the measurement of small electrical currents and voltages. A careful design of the electrical connections between the sample at base temperature and the outer connectors of the cryostat at room temperature are of paramount importance to the performance of the experimental setup. Before installing the measurement wires in a cryostat, one has to take various principles into account. Obviously the thermal load to the base temperature stage induced by the wires should be kept to a minimum. Furthermore, the wires should be shielded to reduce the pick-up of noise and thermal radiation. Finally, one should carefully thermalize and filter the wires to remove high frequency signals that can disturb the thermal equilibrium of electrons. Although these principles are very much connected to each other, they will be discussed separately in the coming paragraphs. In addition to these principles of cryogenic transport measurements, we need the setup to be compatible with our electromigration process which requires a low wire resistance and large bandwidth (typically 1 MHz).

Although a large number of measurement wires is preferable due to the statistical

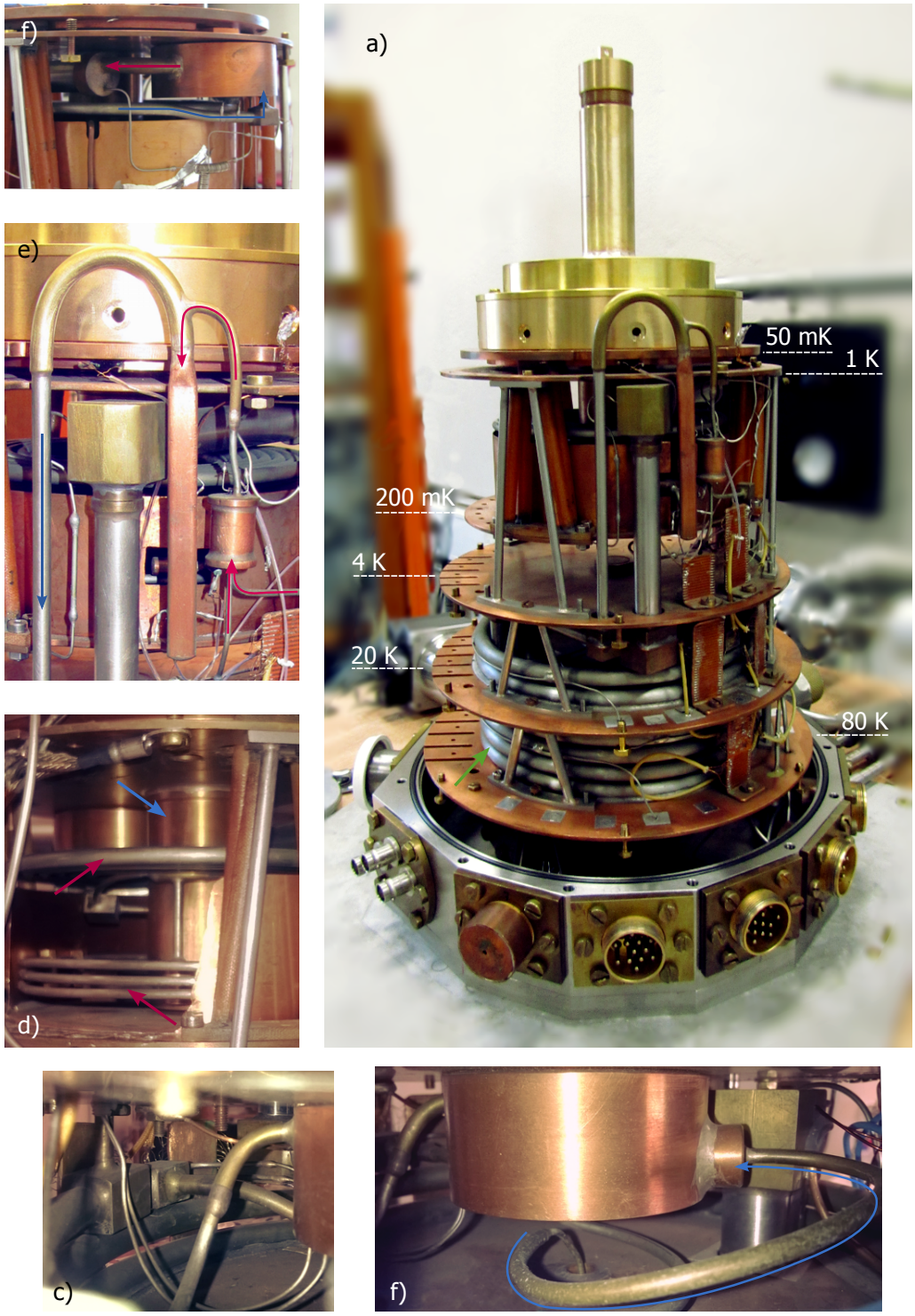

Figure 2.1: Cryogenic parts of our Sionludi. a) The inverted geometry of a sionludi requires extensive shielding at various temperature stages. f) Liquid helium is pushed into the cryostat from below (blue arrow) and enters the 4K reservoir. e) Cold helium vapours exit the 4K reservoir and go through the 4K counter flow heat exchanger to recovery. d) The mixture enters the mixing chamber (blue arrow) through two counter flow heat exchangers (red arrows), each connected to a separate still (c, b).

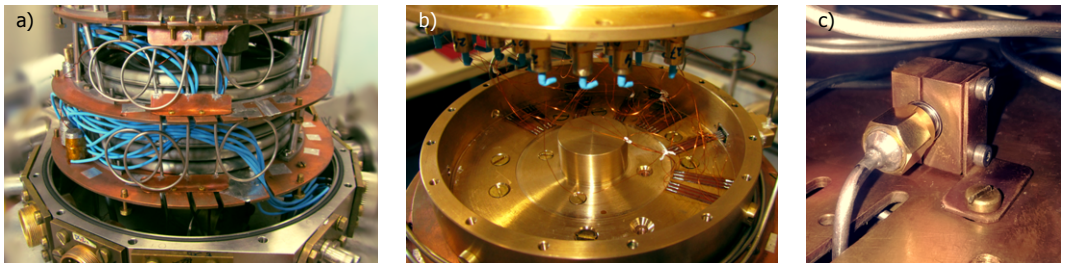

Figure 2.2: a) 27 measurement wires are divided into three capillaries, each filled with Eccosorb [31]. Capillaries shield the wires from radiation, while the Eccosorb filters the high frequency noise on the lines. b) Between the capillaries and the Thermocoax[140], the wires are thermalized at base temperature inside a massive shielded box. c) To thermalize the center conductor of the RF lines, we use -10 dBm attenuator at 4K, solidly clamped in copper.

nature of our experiment, we have to be cautious with the thermal load we induce on the cold stage. Any additional (with respect to the cryostat without experimental wiring) heat load will lead to an increase of the final base temperature depending on the cooling power characteristics of the bare cryostat. The incoming heat flux per wire and shielding capillaries can be kept to a minimum by using materials with low heat conductivity (steel, constantan, manganin or CuNi clad superconducting NbTi), small cross-section and thermal anchoring at intermediate temperatures. The latter can be achieved by adjusting the length between temperature stages, such that the heat flux can be compensated by the available cooling power (at the lower temperature stage). Note however that the wire resistance will increase as the length increases (especially for high resistivity materials), which complicates the electromigration process.

The shielding capillaries can significantly add to the total induced heat load on the cryostat. Nevertheless they are vital to the thermal equilibrium of the electrons in the wires. Unshielded wires act like antennas and absorb and re-emit radiation. Absorption of radiation can excite electrons out of thermal equilibrium. Relaxation may occur by re-emitting a photon or by electron-phonon interaction. As latter process is strongly temperature dependent the electron and phonon bath are essentially thermally isolated from each other at low temperature ($T < 1\text{K}$) and each may be characterized by its own temperature. The absorption of radiation by electrons in the wire can therefore easily lead an elevated electron temperature while can be much hotter than the phonon bath. Shielding capillaries helps isolating the wires from the thermal radiation emitted by the hotter parts of the cryostat.

Black-body radiation (THz) as well as any radiation from the outside world (wifi, tele-communication etc) can propagate along the wires even though they are shielded. The capillaries may isolate the wires, but will not block the radiation propagation inside. Feed-through lumped-element filters can be used to block the radiation up into the GHz regime but fail at higher frequencies. To filter the wires from the high

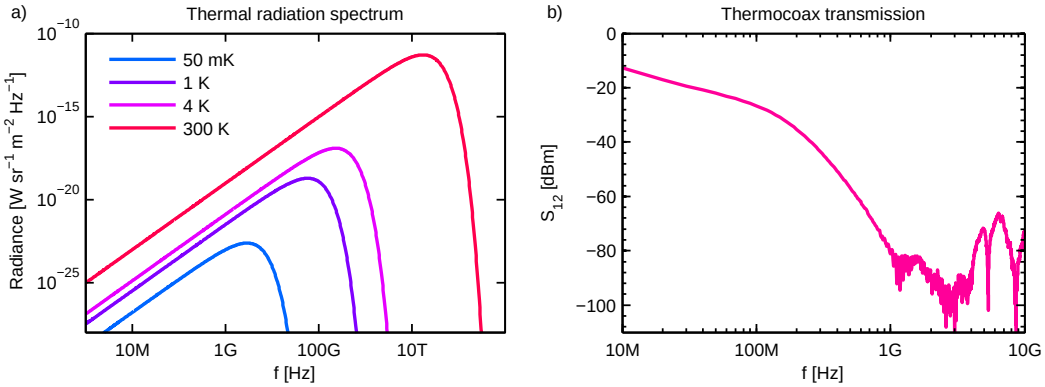

Figure 2.3: a) The thermal radiation spectrum at various relevant temperature. At 50 mK the thermal radiation peaks at about 1 GHz. b) Measured transmission of a 2 meter long thermocoax wire. The attenuation becomes maximal above 1 GHz.

frequency black-body radiation often lossy transmission lines are favoured. The high frequency attenuation in these lines is either based on a dissipative dielectric, e.g. (ferromagnetic) metallic powders (Eccosorb [8]), or a dissipative conductor e.g. Thermocoax [140, 158]. Alternatively one can use superconducting twisted pair wires tightly enclosed in a dissipative copper tape as proposed by Spietz [138]. The attenuation of all lossy transmission lines starts at quite high frequencies (> 1GHz) and depends on the length on the line (typically 1 m). Obviously one can best position the filters at the cold stage of the cryostat just before they enter the sample stage. This ensures thermal re-emission is minimum and the wires will be thermally anchored to base temperature.

We have installed three CuNi capillaries (see figure 2.4) of 1 m length from ambient temperature to base temperature, each containing 9 constantan wires of 0.2 mm-diameter ($R \approx 135\Omega$). The capillaries are filled with Eccosorb to filter the thermal radiation. While the shields are thermally anchored at each intermediate temperature stage, the wires are only directly thermalized at base temperature. The capillaries are equipped with a micro sub-d connector [6] fitted in a home-made brass shield at the cold stage side. At the room temperature side, the wires are connected to a shielded 12 pin Jaeger connector. The shielded base temperature stage (see figure 2.5) is divided into two chambers i.e. the initial cavity (1) where the constantan wires are thermally anchored and a 'clean' sample cavity (2). Two meter long Thermocoax wires provide a filtered feed-through into the sample cavity. The measured signal tranmission (figure 2.3b) shows a strong attenuation above 10 MHz. Copper wires connect the Thermocoax to the thermalized constantan wires on one side and a pin spring-connector at the sample stage on the other. The large heat conductivity of copper ensures a proper thermalization of the sample to base temperature. We haven't used any low frequency cutoff filters to maintain the large bandwidth necessary for electromigration. After electromigration we can optionally filter the lines with external feed-through pi filters

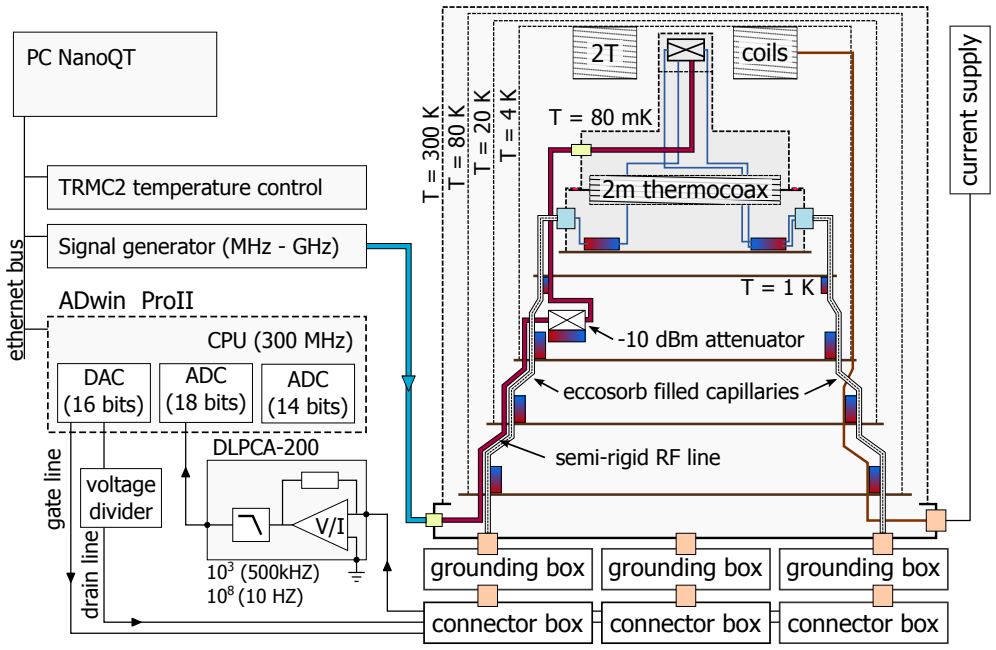

Figure 2.4: A schematic of our measurement setup including the wires in the cryostat.

with a limited bandwidth (< 100kHz).

Besides these 27 DC lines, we have installed 3 broadband AC lines (red thick lines in figure 2.4). From the SMA connectors at the outside of the cryostat to 4 K stage we have used a 80 cm semi-rigid coax cable with a stainless steel center and outer conductor. At the 4 K stage, the center conductor is thermalized by a 10 dBm attenuator firmly enclosed in copper blocks. Between the 4 K and the base temperature stage we have used a 40 cm long semi-rigid coax cable with a stainless steel outer conductor (0.52 mm thick) and a silver plated copper beryllium center (0.51 mm-diameter). At the base temperature stage, a 10 cm semi-rigid copper coax cable with a copper outer conductor connects the line to a SMP receptacle with limited detent to the stage stage (figure 2.6a).

In the upper end of the 'clean' sample cavity we have mounted the sample stage (see figure 2.6a). It consists of a thick (3 mm) brass plate in which we have mounted the 27 pin spring-connectors and the three SMP receptacles. The mass of the brass plate ensures good thermalization of the RF ground which is necessary to sink the heat produced by the RF signals. We have designed a mating sample carrier (figure 2.6b) PCB at which we position three SMP receptacles with full detent. Circular pads provide space for the 27 pin spring-connectors. The copper backplane of the PCB is connected to the gold plated groundplane by vias. The PCB is glued with silver epoxy to a brass plate (1 mm thick) with a thread on the back for handling. The

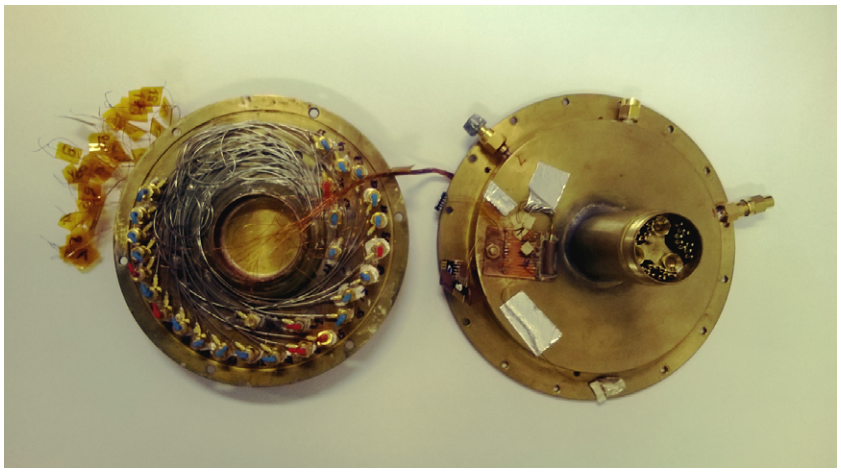

Figure 2.5: The cold stage consists of two chambers separated from each other by a solid brass disk through which the 27 thermocoax wires go (left). The upper part of the cold stage (right) contains the sample stage.

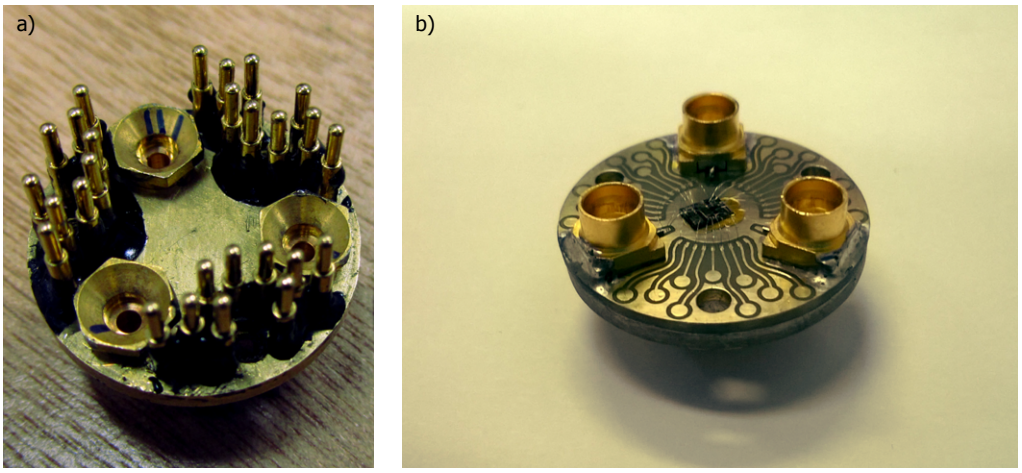

Figure 2.6: The sample stage (a) is made of a thick brass disk on which 27 spring-pin connectors and 3 SMP receptacles are mounted. The three SMP connectors ensure a good alignment of the 27 spring-pins with respect to the sample carrier (b).

three SMP receptacles on each side are connected by male-male SMP adaptors. The snap-in connections provide sufficient force to keep the spring connectors compressed and ensure a good alignment of the 27 spring-connectors.

2.3 Data aquisition

It is a good practice in the Néel Institute to integrate all measurement elements (e.g. amplifiers, voltage devices, low pas filter etc) into a single device which can be connected directly to the outer Jaeger connectors of the cryostat. The compact and shielded environment reduces the risk of ground loops that can couple noise into the measurement setup. We have however chosen for the simpler approach of isolated elements since the development of such a dedicated box can be time consuming. Only in the case of current biased measurements we used a dedicated box since we could benefit from a pre-existing current-biasing box which was developed by Laetitia Pascal and well described in her thesis [112].

For the majority of our measurements we voltage bias the sample (optionally through a home made voltage divider) and measure the current using a commercial current amplifier (Femto DLPCA-200) with variable gain. The voltage signals are provided and read-in by an ADwin ProII system equipped with one voltage DAC (16 bit) card and two voltage ADC (18 and 14 bit) cards. The ADwin system contains a fast (300 MHz) digital signal processor (DSP) which can be programmed to real-time analyse (ADC) and control (DAC) all voltage signals. While the DSP can be programmed for virtually anything, we mostly used a program developed in the lab by E. Bonet, C. Thirion and R. Piquerel that gives the ADwin system various functionalities e.g. sweeping voltages, lock-in measurements and fast feedback electromigration. This particular ADwin program can be controlled by mating home made computer software called NanoQT in which complete measurement schemes can be coded in a JavaScript based language. Originally NanoQT could, besides an ADwin, communicate with any equipment with and TCP connection. Due to the opensource nature of the software we were able to add GPIB support, making it compatible with the older equipment in the lab, like signal generators and lock-in amplifiers.

Chapter 3

Stationary transport properties of QD junctions

In the chapter we discuss theoretical frameworks that describe the electron and heat transport in weakly coupled mesoscopic structures. First we discuss the concept of charge states and use the master-equation approach to calculate the electron transport through a metallic island tunnel coupled to normal or superconducting leads. In the latter case, we solve the master-equation while accounting for the heat transport, as the gapped density of states of superconducting leads results in energy-selective tunneling. We find that maximum heat extraction is obtained at a gate-dependent bias and is exponentially suppressed away from the charge degeneracy points. Next we consider the electron transport through a quantum dot weakly coupled to superconducting leads. The combination of a large level spacing on the quantum dot and the superconducting gap in the leads suppresses thermal energy fluctuations in the device and inelastic scattering on the quantum dot. As a consequence, the electron transport becomes dominated by the tunnel coupling (hybridization) and a first-order perturbation approach is no longer adequate.

Chapter contents

Electron transport through mesoscopic structures can often be well described by assuming free non-interacting electrons moving in an electron gas at an elevated energy with respect to the interacting ground state [103]. This picture, known as the Fermi liquid theory, greatly simplifies the description of electron transport through structures, since Coulomb interactions can be ignored. However there are some situations e.g. the localization of charges, in which one can not ignore the Coulomb interaction between electrons. A simple example is found in small metallic structures, connected by tunnel junctions where the energy cost to add/remove electrons depends on the number of electrons present.

3.1 The single electron transistor

With decreasing structure size and contact area, the transport of electrons becomes dominated by single electron charging effects. A higher contact resistance increases the typical time between two successive tunnel events which may become larger than the typical electron diffusion time. In this regime the number of electrons in the island can be considered as quantized. A smaller size on the other hand decreases the device capacitance such that charging the structure by a single electron comes with a significant energy cost. Together these two properties make it difficult for electrons to enter/leave the structure. At a sufficiently low temperature there are in fact little electrons in the system that have enough energy to enter/leave the structure and electron transport is blocked. As the blockade is caused by the Coulomb interaction between electrons on the structure, it is know as Coulomb blockade. A simple example in which the two properties, i.e. small size, and large contact resistance, are combined is the single electron transistor (SET).

In a single electron transistor (figure 3.1) a small metallic island is connected to two metallic reservoirs (leads) by tunnel barriers ($G_T < G_Q$). A third electrode (gate) is capacitively coupled to the island such that it can modify the electrostatic potential of the island but there can not be any exchange of electrons between the two. The transport of electrons through this system can easily be described by an equivalent capacitance circuit. In this model, developed by Korotkov *et al.* [78], the island is coupled to the leads and gate by capacitors of constant value C_s, C_d and C_g. From electrostatics we know that an additional charge on the island accumulates some electrostatic energy which can be expressed in terms of the capacitance of the island. Moreover, the additional charge on the island must be, due to the quantization of charge, an integer amount of electrons N. We can combine this in the expression for the electrostatic energy of the island,

$$E = \frac{1}{2C}(Ne)^2 = E_C N^2, \tag{3.1}$$

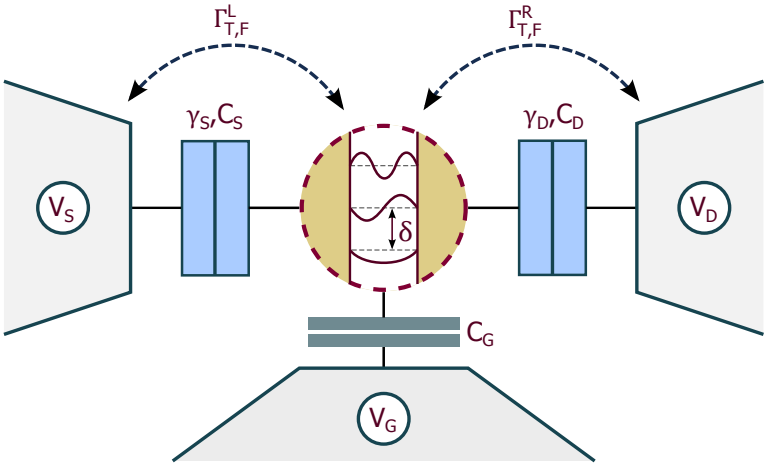

Figure 3.1: In a single electron transistor, a small metallic island ($\delta = 0$) or quantum dot ($\delta \neq 0$) is connected by three terminals. Current can pass through the device by two tunnel junctions that are characterized by their capacitance $C_{S,D}$ and transparency $\gamma_{S,D}$. The third electrode (gate) is only capacitively coupled to the center and allows independent manipulation of the electrostatic potential of the island.

from which we can see that the addition of one electron to the island will increase its electrostatic energy by the characteristic energy E_C, known as the charging energy. In order to transfer an electron from the leads to the island, the electron must have enough energy to provide this charging energy. From this expression it can also be understood why the island has to be small in order to observe charging effects, i.e. E_C is inversely proportional to the capacitance which decreases with decreasing island size.

The charge on the island can be manipulated by applying non-zero potentials to the different electrodes. It turns out that the gate can be used to add (remove) charges to (from) the island. The total electrostatic energy of the island coupled to a source, drain and gate is given below, in which the work performed by the sources is taken into account.

$$E = E_C\left(N - \frac{q}{e}\right)^2 - \frac{q^2}{2C_\Sigma}. \tag{3.2}$$

The charging energy E_C and the *gate induced charge*, q used in eq. (3.2) equation are given by

$$E_C = \frac{e^2}{2C_\Sigma}, \quad q = \sum_i C_i V_i,$$

where $C_\Sigma = C_S + C_D + C_G$, is the total capacitance of the island due to the three capacitors. The gate induced charge is not of integer value; it is a continuous parameter, proportional to the applied potentials e.g. the gate $q \propto C_G V_G$.

From figure 3.2a it is visible that for all possible values of N we get a series of shifted

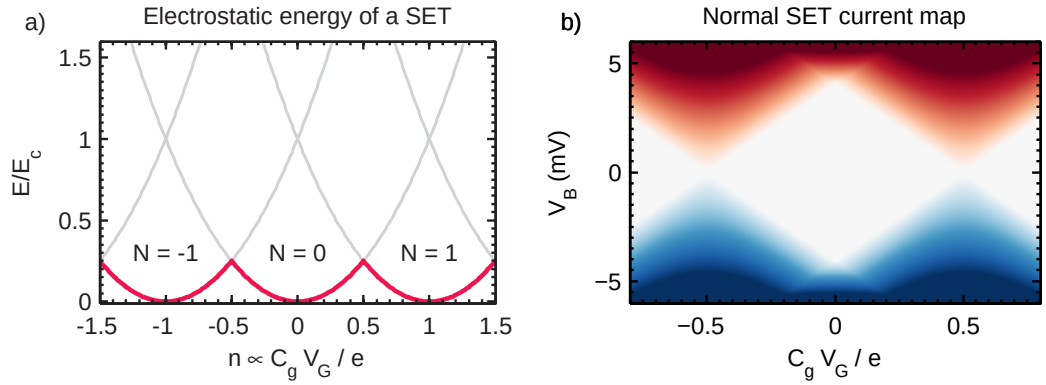

Figure 3.2: a) The electrostatic energy of the island depends the number of additional charges on the island. For each value of the additional charge, the electrostatic energy is a parabolic function of the gate induced charge The red curve denotes the island ground state. b) The current map, i.e. $I(V_B, V_G)$, of a single electron transistor shows diamond shaped areas in which the current is zero. (T = 100 mK, E_C = 2.0 meV)

parabolas representing the various charge states of the island. Between the low-lying intersections with neighbouring parabolas the island has a minimum energy related to a fixed number of charges N. When q is of integer value, the energy difference with any of the neighbouring parabolas is equal to the charging energy and charge transport is blocked. However, when q moves away from such a point, the energy difference becomes less, until the point where $q = n \pm 1/2$ and two parabolas intersect. Here the island can be in either of the two charge states and sequential transport of electrons through the island is possible. If q is moved any further, the island will remain in the new charge state with minimum electrostatic energy and transport becomes blocked again. This illustrates how we can manipulate both the island's charge state and the charge transport through the island, just with the applied potential to the gate.

In the previous paragraph it was assumed that the island always resides in the charge state with minimum electrostatic energy. However, when there is enough energy available, the charge state of the island can become different. By taking into account that the island is connected to two leads at different non-zero electrostatic potential (i.e. non-zero bias), we can define four different processes in which the transfer of a single electron changes the charge state of the island i.e. the addition of an electron from the source or drain and the extraction of an electron to the source or drain. For each of these processes, the energy difference between the final and initial state of the total system can be determined. Note that in these processes an electron is also added (extracted) to (from) the leads at an energy cost eV ($-eV$), which has to be taken into

account.

$$\begin{aligned} \text{from (to) the source :} \quad & \mu^{S}_{F(T)}(N) = E(N \pm 1) - E(N) \mp eV_S \\ \text{from (to) the drain :} \quad & \mu^{D}_{F(T)}(N) = E(N \pm 1) - E(N) \mp eV_D \end{aligned} \tag{3.3}$$

Because we assume only a weak coupling between the leads and the island, these single-electron transfers occur randomly and are characterized by a energy dependent *transfer rate* $\Gamma(\mu)$, which can be interpreted as the probability per unit time for this event to occur. Since each of these processes changes the charge state of the island from one into another, a simple master equation approach can be used to calculate the probability that the island is in a given charge state P_N.

$$\begin{aligned} \frac{dP_N}{dt} = \quad & P_N(t)\left(\sum_{i=S,D}\Gamma\big(\mu^i_F(N)\big) + \Gamma\big(\mu^i_T(N)\big)\right) - \\ & P_{N-1}(t)\sum_{i=S,D}\Gamma\big(\mu^i_T(N-1)\big) - P_{N+1}(t)\sum_{i=S,D}\Gamma\big(\mu^i_T(N+1)\big) \end{aligned} \tag{3.4}$$

The master equation given by eq. (3.4) relates the change in the probability to find the island in a given charge state to the transfer rates between the charge states. These transfer rates can be decomposed into all rates *to* and *from* the given charge state, and are given by the probability of being in a certain charge state multiplied by the rate at which which electrons tunnel to and from the island. In case of a stationary system the evolution of the probabilities becomes zero and the system can be solved easily under the condition $\sum_n P_n = 1$. Actually, when one writes eq.(3.4) in matrix from, the solution of the system can be obtained by a simple matrix inversion. Once the probabilities are known, the current through the island is given by the difference of electrons entering and leaving one of the leads.

$$I = e\sum_n P_n\left(\Gamma\big(\mu^k_T(N)\big) - \Gamma\big(\mu^k_F(N)\big)\right) \qquad k = S, D \tag{3.5}$$

The only remaining task is the calculation of all possible single-electron transfer rates. Since a small tunnel coupling between the leads and the island is assumed, it is reasonable to start from Fermi's Golden rule using the tunnel Hamiltonian as perturbation. This Hamiltonian, given in eq. (3.6) in operator form, simply describes the transfer of an electron from a lead to the island as the creation of an electron with energy ν_I in the island and the annihilation of an electron with energy ν_L in the lead. The complex conjugate term represents the transfer of an electron in the opposite direction.

$$H_T = \sum_{\nu_I\nu_L} t_0 c^\dagger_{\nu_L} c_{\nu_I} + h.c. \tag{3.6}$$

When we substitute this Hamiltonian into Fermi's Golden rule and sum over all possible configurations that belong to the initial and final charge states, we obtain the following expression for the transfer rate of electrons from a lead to the island[1]:

$$\Gamma_{L\to I}(\mu) = \frac{4\pi t_0^2}{\hbar}\int_{-\infty}^{\infty} f_L(E)n_L(E)\big(1-f_I(E-\mu)\big)n_I(E-\mu)dE. \tag{3.7}$$

In this equation f_L (f_I) is the Fermi-Dirac distribution on the lead (island), n_L (n_I) is the density of states of the lead (island) and μ is the characteristic energy difference of the process which is in the case of elastic tunneling given by eq. (3.3). The transfer rate of electrons in the opposite direction is given by a similar equation.

$$\Gamma_{I\to L}(\mu) = \frac{4\pi t_0^2}{\hbar}\int_{-\infty}^{\infty} \big(1-f_L(E)\big)n_L(E)f_I(E-\mu)n_I(E-\mu)dE \tag{3.8}$$

In these rate equation we have taken the Fermi-Dirac distribution to describe the occupation probability distribution of the island. This is justified because we have assumed that the tunnel rate is low and there is enough time between tunnel events for electrons to relax to a quasi-equilibrium with the island[2].

Now the rate equations and the electrochemical potentials of the four single-electron transfer processes are known, one can calculate the current through the device for any combination of applied potentials. Figure 3.2b shows the colormap of the current through a device with normal leads and island (i.e. constant density of states) as a function of the gate and bias. The white diamond shaped areas indicate the absence of current and are known as Coulomb diamonds. Within these regions the number of additional electrons on the island is constant and the transport of electrons is Coulomb blockaded.

3.2 Electron transport though hybrid devices

The framework introduced in the previous section also allows us to calculate the current through an (normal) island connected by superconducting leads. Instead of a constant density of states, one has to use a superconducting density of states in eq. (3.7 and 3.8). It turns out that such a hybrid device shows interesting thermo-electric properties and can be used as a heat transistor. Before we can discuss on this interesting feature of hybrid SETs, we will shortly introduce the microscopic theory of superconductivity developed by Bardeen, Cooper and Schrieffer.

The origin of the BCS theory is the discovery that the Fermi liquid becomes unstable

[1] A well explained and detailed derivation can be be found in [14] (page 155-157)

[2] This assumption is generally valid for single electron transistors coupled to normal lead. However there are devices, where one can not assume thermal equilibrium. Interesting examples can be found in experiments by Pothier *et al.* [120] and Pekola *et al.* [114]

below a critical temperature. Cooper showed that a small but finite attractive potential between electrons, mediated by electron-phonon interactions, causes a phase change under the formation of bound s-wave electron pairs, known as Cooper pairs[3]. The new ground state can be described by the BCS Hamiltonian,

$$H_{BCS} = \sum_{k,\sigma} \xi_k c^\dagger_{k\sigma} c_{k\sigma} + \sum_{kk'} V_{kk'} c^\dagger_{k\uparrow} c^\dagger_{k\downarrow} c_{\prime k\uparrow} c_{k'\downarrow} \tag{3.9}$$

where the first term describes the free electron states (quasi-particles) with energy ξ and the second term accounts for the attractive potential between electrons which leads to the formation of Cooper pairs. Next, BCS argued that the fluctuations around the expectation value of ground state (given by $\langle c^\dagger_{k\uparrow} c^\dagger_{k\downarrow}\rangle$), must be small due to the vast number of Cooper pairs that participate in it. Therefore it is justified to simplify this Hamiltonian to its mean-field form given by

$$H_{MF} = \sum_{k,\sigma} \xi_k c^\dagger_{k\sigma} c_{k\sigma} - \sum_{k} \Delta_k c^\dagger_{k\uparrow} c^\dagger_{k\downarrow} + \Delta^*_k c_{\prime k\downarrow} c_{k'\uparrow} \tag{3.10}$$

where $\Delta_k = -\sum_{kk'} V_{kk'} \langle c_{\prime k\downarrow} c_{k'\uparrow}\rangle$. From here there are two ways to solve the mean-field Hamiltonian i.e. the original variational method[4], and by the Bogoliubov transformation which we will shortly discuss.

The mean field Hamiltonian in equation 3.10 can be diagonalized by the unitary Bogoliubov transformation of the operators c and $c^\dagger$ (eq. 3.11). The off-diagonal elements disappear by choosing u_k and v_k such that they satisfy the relation $\Delta^*_k v^2_k - \Delta_k u^2_k - 2\xi v_k u_k = 0$

$$\begin{pmatrix} \gamma_{k\uparrow} \\ \gamma^\dagger_{k\downarrow} \end{pmatrix} = \begin{pmatrix} u^*_k & v_k \\ -v_k* & u_k \end{pmatrix} \begin{pmatrix} c_{k\uparrow} \\ c^\dagger_{k\downarrow} \end{pmatrix}. \tag{3.11}$$

After the transformation the mean field Hamiltonian takes the simple form of two terms. One is the condensation energy of the BCS ground state and the second is equal to the Hamiltonian of non-interacting quasi-particles with an energy given by

$$E_k = \sqrt{\xi^2_k + |\Delta_k|^2}. \tag{3.12}$$

With this solution one can calculate various important parameters of the superconductor, like the superconducting order parameter Δ, the critical temperature T_c and their temperature dependencies. Here we will focus on the density of states of the

[3]The two electrons participating gain energy by forming a pair. The energy gained is given by $\Delta E = 2\omega_D exp\big[-\frac{2}{Vn(\varepsilon_F)}\big]$, where ω_D is the Debye frequency of the phonons, V is the attractive interaction strength and $n(\varepsilon_F)$ is the density of states of the metal at the Fermi energy. Using Heisenberg uncertainty relation, the energy can be related to an average distance between the two electrons forming the pair. This distance is known as the phase coherence length in a superconductor.

[4]A detailed coverage of the methods is given by Tinkham [144]

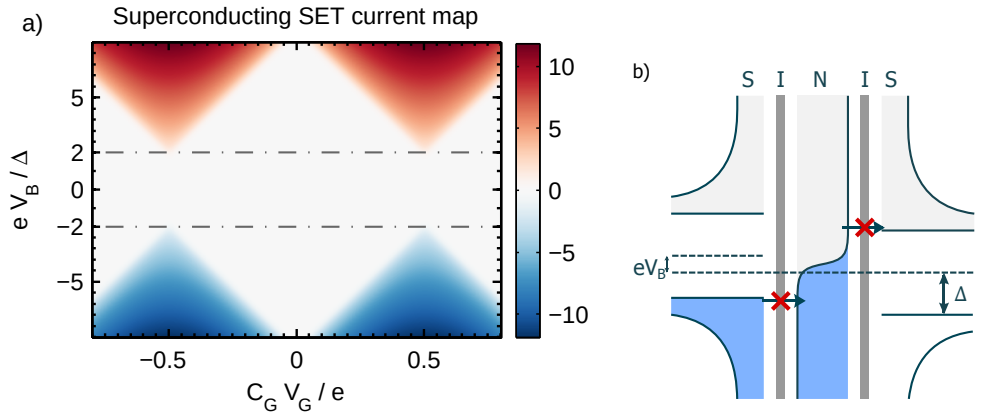

Figure 3.3: a) The current map of a superconducting single electron transistor. The gap in the superconducting density of states results in an additional area of zero current i.e. $V_B < 2\Delta$. (T = 200 mK, E_C = 0.7 meV, R_N = 33kΩ) b) The superconducting density of states results in energy selective transport of electrons. In a sandwich structure bias at $V_B < 2\Delta$ only hot electrons can tunnel out of the normal center, while hot holes are removed. (blue indicates occupied states)

quasi-particles (free un-bound electrons) and Cooper pairs. The latter is rather simple. Since Cooper pairs are bosons, Pauli's exclusion principle does not apply and they can all join in a macroscopic quantum state of the Fermi-energy. The quasi-particle density of states can be obtained by the notion that electrons in the normal state have a constant density of states $N(0)$ around the Fermi-energy. This leads to the following result for the superconducting density of states $n_S(E)$

$$\frac{n_S(E)}{N(0)} = \frac{|\Delta|}{\sqrt{E^2 - \Delta^2}}. \tag{3.13}$$

Since there are two types of particles in superconductors i.e. the quasi-particles that behave like free non-interacting electrons and the Cooper-pairs located at the Fermi-energy, the current through a device consists of the transport of both individually. At zero bias the Cooper-pair transport gives rise to a non-dissipative current, known as supercurrent. At non-zero bias the supercurrent is modulated in time due to the AC-Josephson effect and the time-averaged supercurrent will be zero except for specific bias voltages when so-called multiple Andreev reflection can take place. The discussion of Andreev reflections and the description of superconductivity in mesoscopic structure is however outside the scope of this thesis. In the remaining part of this chapter we will only discuss the transport of quasi-particles in the tunnel coupling regime. Using the BCS density of states in eq. (3.7 and 3.8), it is possible to calculate the current and charge state occupation probabilities of a superconducting single-electron transistor (SSET). In figure 3.3a the current through a superconducting SET is shown on color map. Compared to the normal SET (see figure 3.2b) there is an additional region

where current is blocked i.e. $V_B < 2\Delta$. This a direct consequence of the gap in the superconducting density of states, which becomes clear if we look at the energy diagram of a metallic normal island between two superconductors as presented in figure 3.3b. Here we have assumed that the superconducting gap is larger than the thermal energy energy in the superconductors ($\Delta > k_B T_S$), such that all electrons states in the lower BCS branch are occupied and all states is the upper branch are empty. When the bias is below 2Δ and the thermal energy of the island is small ($k_B T_N \ll \Delta - eV_B$), there are nearly no electrons on the island that can enter the superconductors. Likewise there are no electron states available at the island and the sequential tunneling of electrons is blocked. With increasing applied bias, the amount of electrons that can tunnel between the island and the superconductors increases according to the thermal distribution on the normal island until $V_B > 2\Delta$. Beyond this point, sequential tunneling will still increase with temperature, but is less and less dominated by the thermal distribution of the electrons of the island. In conclusion one can state that the electron transport below $V_B = 2\Delta$ is strongly dependent on the temperature of the normal island. Above $V_B = 2\Delta$, the temperature dependence becomes weaker and the electron transport is almost fully determined by the applied bias.

3.3 Heat flow in a hybrid device

To this point we have assumed that the electrons that tunnel into the island spent enough time (dwell time) there to interact and come to thermal equilibrium with the Fermi-sea of the island. This implies that during the dwell time, the electron dissipates (extracts) energy to (from) the other island electrons. When the Fermi sea is in good thermal contact with a thermal reservoir i.e. in the limit of infinite electron-phonon coupling with a phonon bath, the electron temperature will always be equal to the phonon temperature (equilibrium). However, when the electron-phonon interaction is finite, the heat dissipated (extracted) by the transport of electrons has to be taken into account. In this case, the current has to be calculated with the requirement that the following heat balance is satisfied:

$$\frac{dT_e}{dt} = \kappa V\left(T_e^5 - T_{ph}^5\right) + \phi_{et} = 0. \tag{3.14}$$

The heat equation in eq. (3.14) relates a change in electron temperature to the sum of all heat fluxes. Here we only take the two leading contributions into account. The first term in this equation represents the energy exchange between the Fermi sea and the phonon bath at temperature T_{ph}, due to the electron-phonon interaction (characterized by the electron-phonon coupling parameter κ) in a volume V. The second term, ϕ_{et}, accounts for the heat transfer due to electrons that tunnel to and from the island. The

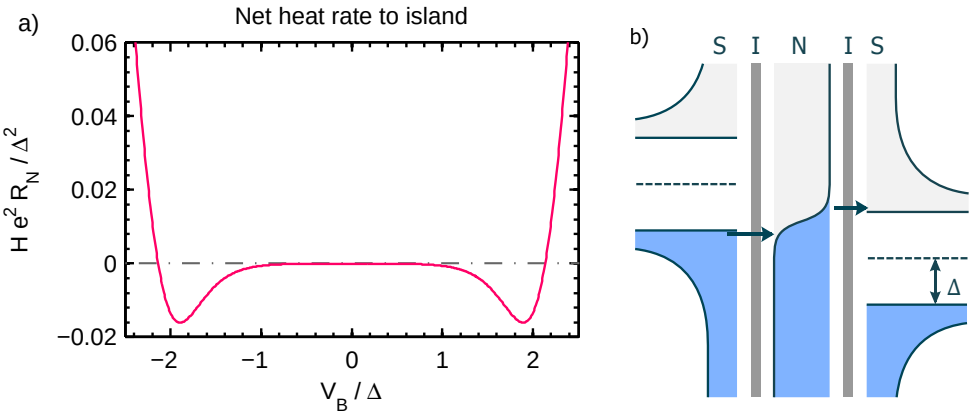

Figure 3.4: a) Net heat flow out of the normal island as function of V_B. Negative flow indicates electronic cooling of the island. (T_{base} = 200 mK, E_C = 0.7 meV, R_N = 33kΩ) b) Heat can be removed from the normal part of an superconductor-normal metal tunnel junction when the applied bias is below Δ.

contribution of this heat flux is given by the weighted sum of the following heat rates:

$$H_{L\to I}(\mu) = \frac{4\pi t_0^2}{\hbar}\int_{-\infty}^{\infty}(E-\mu)\cdot f_L(E)n_L(E)\big(1-f_I(E-\mu)\big)n_I(E-\mu)dE \tag{3.15}$$

$$H_{I\to L}(\mu) = \frac{4\pi t_0^2}{\hbar}\int_{-\infty}^{\infty}E\cdot\big(1-f_L(E)\big)n_L(E)f_I(E-\mu)n_I(E-\mu)dE, \tag{3.16}$$

where $H_{L\to I}$ ($H_{I\to L}(\mu)$) gives the heat added (subtracted) to the island. These equations are identical to eq. (3.7, 3.8), except for the extra energy term in the integrand which accounts for the energy transfer between two objects (at different electro-chemical potential) due to electron tunnelling events. In figure 3.4a the difference between the two rates ($H_{L\to I}(\mu) - H_{I\to L}(\mu)$) is plotted for an SIN tunnel junction as function of eV. It can be seen that at high bias ($eV > \Delta$), heat is deposited into the normal part of the junctions, while at low bias ($eV < \Delta$) heat is actually removed from the normal part i.e. the normal part is cooled by the superconductor[5]. This non-equilibrium cooling can be illustrated best by an energy diagram of a SIN junction biased just below the superconducting gap Δ as shown in figure 3.4b.

From this diagram it becomes clear that, as a direct consequence of the superconducting gap, only hot quasi-particle excitations can tunnel into the superconductor, which will result in a lower electron temperature on the normal part. This concept of electronic cooling in SIN junctions was proposed and experimentally verified by Nahum *et al.* [101]. One can anticipate that the extraction of heat out of the normal part will be doubled when it is sandwiched between two superconductors as was shown experimentally by Leivo *et al.* [86]. At optimal bias ($V_B^{opt} = 2\big(\Delta - 0.66k_BT_N\big)/e$) hot

[5]The total work done by the source is still equal to IV_B. While the source remove heat from the normal, they dissipate heat in the superconductors [122]

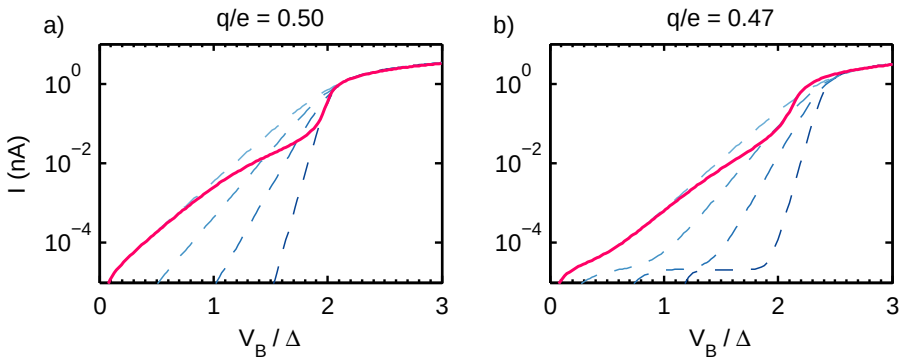

Figure 3.5: Electronic cooling of the normal island in a superconducting SET is visible in the sub-threshold current. The solid lines is the numerical self consistent solution of the master equation and heat balance equation. The dashed lines give the $I(V_B)$ curves of the system at constant normal island temperature (isotherms). (radius = 100 nm, $\kappa = 2.3 \cdot 10^9$, $R_N = 33\text{k}\Omega$, $T_{bath} = 200$ mK, $E_C = 0.7$ meV)

quasi-particles are extracted from one side, while at the other side the hot quasi-holes are filled. However, since the normal island is only coupled by tunnel junctions, can expect to observe charging effects as the capacitance of the device decreases. This poses the question how the electronic cooling in SINIS junctions is affected by the charging energy in the regime where $E_C > k_B T_N$. In recent work by Saira *et al.* [132] it was shown that the electronic temperature of the normal island of a superconducting SET can be well regulated by the gate potential. At optimal bias the heat flow out of the normal island is significantly suppressed when the gate is detuned from a charge degeneracy point.

In the above experiments the temperature of the normal island is often probed by additional SIN junctions whose positioning can form a practical challenge, especially for small normal islands. Alternatively one can directly extract the temperature of the normal island from the full $I(V_B)$ curves of a SINIS junction as was shown by Rajauria *et al.* [123]. The ability to perform a likewise analysis of the $I(V_B)$ curves of a superconducting SET would enable the study of heat transport through a small normal island. In this thesis we have self consistently solved the master equation (eq. 3.4) and heat equation (eq. 3.14) numerically in order to obtain the $I(V_B)$ curves of a SSET when the heat transport is taken into account. Figure 3.5 shows the $I(V_B)$ relations at (left panel) and just besides (right panel) the charge degeneracy point of a SSET with $E_C = 0.7\,\text{meV}$. The solid line results from the full self consistent solution, while the dashed lines are solution of the bare master equation assuming different island temperatures. Each crossing with an isotherm gives the electronic temperature of the normal island. At non-zero gate detuning (right panel), the $I(V_B)$ become affected by the charging energy and the cooling power is suppressed. The results in the left panel replicate the results of Rajauria *et al.* [123] up to some factor. In the right panel

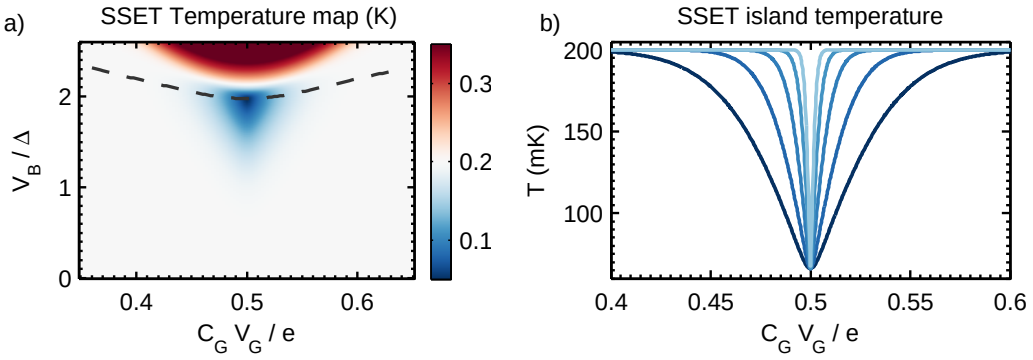

Figure 3.6: a) The temperature of a (spherical) normal island in a superconducting SET shows the electronic cooling by the superconducting leads (radius = 100 nm, $\kappa = 2.3 \cdot 10^9$, $R_N = 33\text{k}\Omega$, $T_{bath} = 200$ mK, $E_C = 0.7$ meV). The cooling is most pronounced around the charge degeneracy point and just below Δ. b) The temperature versus gate induced charge shows the localized character of the electronic cooling in a superconducting SET. With increasing charging energy the cooling becomes more localized (from dark to light blue: $E_C = 0.6$, 1.2, 2.4, 4.8, 9.6 meV).

however, we observe quite a different behaviour, but the effect of electron cooling still clearly visible.

Furthermore we can numerically calculate the electronic temperature map as is shown in figure 3.6a. It shows that electronic cooling is only locally present around at the charge degeneracy point and optimal bias V_B^{opt} where it is maximal. At these points the voltage drop between the island and both superconductors is smaller than Δ and both SIN junctions contribute to the electronic cooling. Similar to Saira *et al.* we observe the strong suppression of the electronic cooling at optimal bias when the gate is detuned from a charge degeneracy point. Further analysis of the minimum temperature of the normal island shows that the optimal bias (denoted by the dashed black line) itself increases with the detuning of the gate. Still it is not equal to $V_B^{opt} + 4E_C(n_g - 0.5)/e$, which would correspond to the optimal alignment (in the context of electronic cooling) of one of the leads with respect to the normal island. While electronic cooling is optimized for one junction, it is counterbalanced by heating due to the other junction. As to obtain optimal cooling of the island, heat must be extracted by both junctions simultaneously.

Finally we look at the effect of an increasing charging energy on the electronic cooling. Figure 3.6b shows the electronic temperature of the island at (classical) optimal bias as a function of gate for various charging energies. The minimum electronic temperature is equal for all charging energies and is obtained at the charge degeneracy point. Moreover we observe that the gate-space of electronic cooling decreases exponentially with increasing charging energy which is consistent with the exponential suppression of the heat flow in the SET off-state as reported by Saira *et al.* [132]. This implies that in the limit of large charging energy, e.g. in quantum dots, cooling

will become practically impossible as one needs a very high gate coupling parameter. Besides this practical limitation, the electronic cooling of quantum dot is also affected by the confinement of the electronic wave-function.

3.4 Quantum dot conductance by first-order perturbation

In very small structures, i.e. when the lateral size becomes smaller than de Broglie wavelength of the electrons, the spatial confinement of the electron wave functions becomes dominating. In this case the density of states of the structure is no longer continuous, but becomes discrete. The electrons around the Fermi-energy can be described by the particle-in-a-box model. Quantum mechanics dictates that only wave functions with an energy belonging to a set of discrete energies can exist in the potential well. The eigenenergies of these single-particle states are separated by a mean energy spacing δ which is inversely proportional of the spatial size L of the confinement potential e.g. $\propto 1/L^3$. When the mean energy spacing of electrons on the island of a SET becomes larger than its thermal energy (i.e. $\delta > k_B T$), the electron transport through the structure (now called a quantum dot) will become affected by the quantum confinement. In this case we can no longer use the eq.(3.4) to calculate the electron transport, but we have to solve the master equation for the so-called many-body states of the quantum dot[7].

Obviously the particle-in-a-box model describes only a single particle, while quantum dots generally contain many hundreds (thousands) of valence electrons. Therefore one has to describe the electron transport through a quantum dot in terms of its many-body states. Provided that the electrons can been seen as non-interaction particles, the many-body states are given by all unique distributions of N electrons over the available single-particle states of the particle-in-a-box model. Because electrons are fermions, any single-particle level may contain up to two electrons (spin up, spin down); more than two electrons is forbidden by the Pauli exclusion principle.

In second quantization representation, many-body states are given by the occupation enumeration of the all levels. When the orbital levels are labelled by index k, and the occupation of a level is given by n, the many-body states are represented by the set $\{n_k\}$. The energy of the state is given by $\sum_k E_k n_k$ and the number of participating electrons is $\sum_k n_k$. In this framework, the addition (extraction) of an electron to (from) a level k is obtained by the creation (annihilation) operator $c_k^\dagger$ (c_k) acting on the many body state of the quantum dot. For example, the excitation of an electron from level k to level k' is given by an annihilation operator c_k, followed by the creation operator $c_{k'}^\dagger$, i.e. $c_{k'}^\dagger c_k |\chi\rangle$.

Formally, to describe the transport of electrons through a quantum dot coupled to

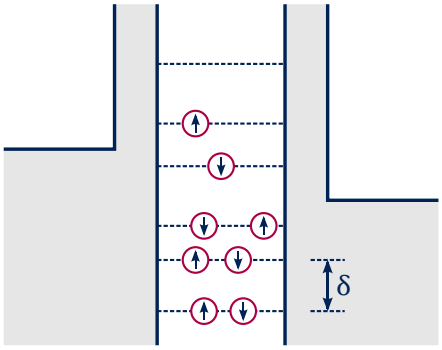

Figure 3.7: The small size of a quantum dot confines the electrons in a small space. This results in a non-zero level spacing. Each level can be filled by zero, one (spin up or down) or two (spin up and down) electrons.

leads, one has to consider the full system as given in eq. (3.17).

$$H = H_L + H_R + H_T + \left(\sum_k t_k c_k^\dagger c_k + E_C N^2 - eV_g N\right) \tag{3.17}$$

Here the first two terms represent the leads, the third describes the single-electron tunnelling between the dot and the leads (as introduced by eq(3.6), and the final term accounts for the many-body state of the quantum dot subjected to a large charging energy. By assuming weak coupling between the quantum dot and the leads, one can use a first order perturbation approximation to derive the following master equation [143] which describes the electron transport up to the first order in the tunnel coupling.

$$\frac{dP_{|\alpha\rangle}}{dt} = \sum_{|\beta\rangle \vee \setminus |\alpha\rangle} P_{|\beta\rangle}\Gamma_{|\beta\rangle\to|\alpha\rangle} - P_{|\alpha\rangle} \sum_{|\beta\rangle \vee \setminus |\alpha\rangle} \Gamma_{|\alpha\rangle\to|\beta\rangle} \tag{3.18}$$

The master equation relates the change in the occupation probability of a given many-body state $|\alpha\rangle$ to the transition rates to and from state $|\alpha\rangle$. The transitions between states are the result of single electrons tunnelling between the leads and the quantum dot. The energy difference μ of the total system due to the transfer of an electron is given by the difference in electrostatic energy μ_{ES} (as given by eq. 3.3) plus the energy difference $\mu_\delta = E_{|f\rangle} - E_{|i\rangle}$ between the initial ($|i\rangle$) and final ($|f\rangle$) state of the quantum dot. The latter is simply equal to the associated single electron level spacing. In the limit of weak coupling between the quantum dot and the leads, the single electron transfer rates can be determined by Fermi's Golden rule:

$$\begin{aligned}\Gamma^T(\mu) &= 2\pi t_0^2 \int_{-\infty}^{\infty} f(E)n(E)\delta(\mu)dE. \\ \Gamma^F(\mu) &= 2\pi t_0^2 \int_{-\infty}^{\infty} (1-f(E))n(E)\delta(\mu)dE,\end{aligned} \tag{3.19}$$

where $\delta()$ is the Dirac delta function. The validity of Fermi's Golden rule is determined by the energy dependence of the states in the lead i.e. the density of available states can only change very little with respect to the tunnel coupling. In the case of a quantum dot coupled to normal leads, this translates to the requirement that the tunnel coupling should be much smaller than thermal energy of the quantum dot ($t_k \ll k_b T$). In the case of intermediate coupling, i.e. when the aforementioned condition is not valid, one has to take into account the broadening of the discrete states due to the finite coupling. This will be the subject of the next section.

3.4.1 Electron thermalization rates

Once all possible transition rates are known, one can obtain the occupation probabilities in steady state by matrix inversion[6]. Next, the current through the quantum dot can be calculated using the obtained probability distribution. Figure 3.8a shows the conductance map of a quantum dot with 4 single electron levels weakly coupled to two normal leads. One can clearly identify the regions of zero current due to Coulomb blockade. Outside the Coulombs diamonds there are additional regions of zero differential conductance, separated by clear lines of non-zero differential conductance. Each of these lines corresponds to an increase (decrease) in current due to a change in the number of single particle level located between the Fermi energies of the leads. Previously, in the description of charge transport through an island[7], we assumed that the electrons on the island remained in thermal equilibrium regardless of the charge transport. This is reflected by the use of a Fermi-Dirac distribution in the rate equations (3.7, 3.8), which dictates the thermal occupation of levels. In the case of a quantum dot however, the master equation dictates the occupation probability of the many-body states. This justifies the question, where and how thermal equilibrium is introduced in the master equation for a quantum dot. The answer is simple; it isn't. There are no terms in the Hamiltonian given in eq. (3.18) that include thermalization. This reduces the validity of the numerical results presented in figure 3.8a to the strongly non-equilibrium limit where the electron tunneling rate Γ_{et} is much larger the the thermalization rate Γ_{th} ($\Gamma_{et} \gg \Gamma_{th}$). To impose thermal equilibrium on the system, one can use the Gibbs distribution in the grand canonical ensemble to calculate the occupation probabilities, instead of solving the master equation. This, on the other hand, will not take into account the effect of single-electron transport. To account for both, Beenakker *et el.*[7]

[6] Although theoretically it should be possible to solve the master equation for any set of single electron levels, there is a practical limit on the number of levels due to the computational power of an ordinary computer. To solve the equation, one normally writes the master equation in matrix form such that the solution can be obtained by matrix inversion. The size of the matrix is given by $N = 2^M$, where M denotes the number of single electron levels. Obviously it is just the large size of the matrix that limits the number of electron levels to about 8

[7] From here on we will refer to *island* as an object with zero level spacing but finite charging energy.

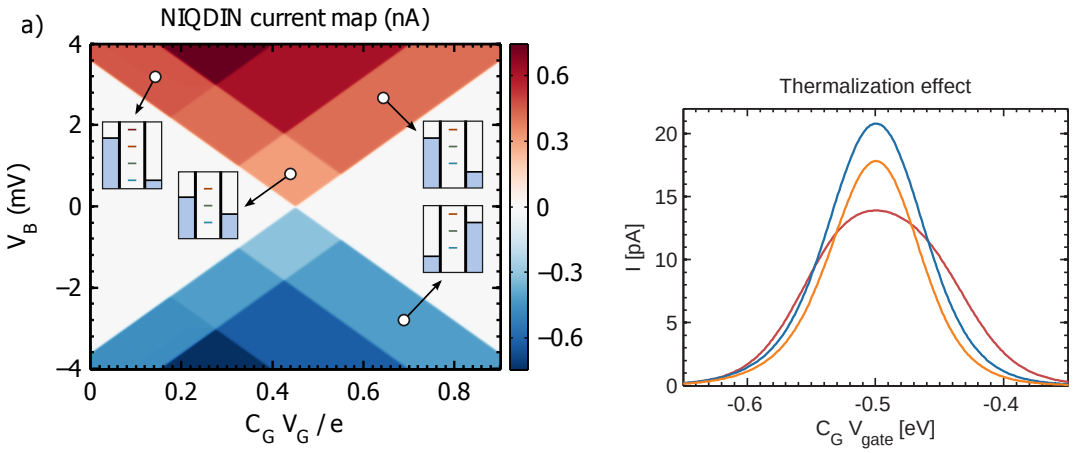

Figure 3.8: a) Current map of a normal — quantum dot device showing areas of constant current. Each area corresponds to a different number of electron levels between Fermi-energies in the leads (illustrated by insets). ($\Delta\delta$ = 0.8, 1.0, 1.2 meV. b) The conductance peak at charge degeneracy is affected by the thermalization processes of the quantum dot. At fast thermalization $\Gamma_{th} \gg \Gamma_{et}$, the state occupation $P_{|\alpha\rangle}$ is given by the Gibbs distribution in the grand canonical ensemble (blue curve). In the opposite limit (red curve), $P_{|\alpha\rangle}$ can be calculated by the master equation (eq. 3.18). In the intermediate regime (orange curve) one can use the equation of Beenakker *et al.* (eq. 3.20) to obtain $P_{|\alpha\rangle}$.

solved the master equation for a quantum dot weakly coupled to normal leads, under the condition that the state occupation probability is given by the Gibbs factor plus some small bias dependent correction which is given by:

$$\text{const.} + \frac{eV}{k_B T} \sum_{k=1}^{\infty} n_k \left(\frac{\Gamma_k^R}{\Gamma_k^L + \Gamma_k^R} - \frac{\mu_L - \mu_{QD}}{\mu_L - \mu_R} \right). \tag{3.20}$$

The first term in this equation, a constant, takes care of the re-normalization of the probability distribution. The sum in the second term runs over all single-electron levels of the quantum dot, where n_k is the level occupation of the state and $\Gamma_k^{L,R}$ are the single-electron tunnelling rates from level k on the dot to the leads. Eq. (3.20) is valid when all single-electron tunnelling rates remain smaller than the temperature and the mean level spacing ($\Gamma_{et} \ll k_B T < \delta$); a condition which is easily satisfied when the quantum dot is weakly coupled to normal leads. Note that the correction term becomes zero when $\Gamma_k^R / \left(\Gamma_k^L + \Gamma_k^R\right) = \eta$ for all k which implies that the level occupation is then fully determined by the thermal processes on the dot. As to illustrate the effect of energy thermalization on the electron transport through a quantum dot, the current in plotted as a function of the applied gate in two extreme situations: $\Gamma_{th} = 0$ (red) and $\Gamma_{et} \ll \Gamma_{th}$ (blue) (figure 3.8b).

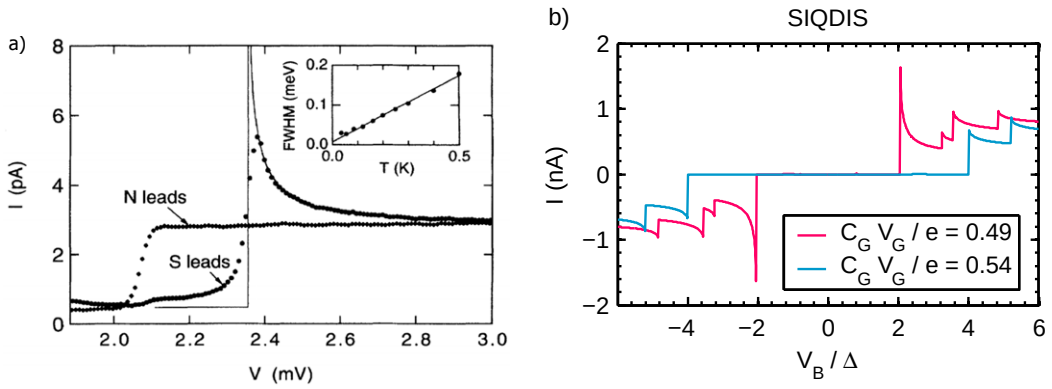

Figure 3.9: a) The current through a superconducting-quantum dot device as a function of the applied source-drain bias as measured by Ralph *et al.* [124]. b) The current trace shows replicas of the superconducting density of states at each inclusion of a 'channel' between the two Fermi-energies of the leads. In the first order approximation this results in non-physical singularities. The peak height is maximal at charge degeneracy (red curve), when the two coherence peaks of the leads are aligned with a single level.

3.4.2 SUPERCONDUCTOR — QUANTUM DOT DEVICES

By using the superconducting density of states in eq. (3.19), we calculate the electron transport through a quantum dot coupled to superconducting leads. Figure 3.9b shows the current through the quantum dot as a function of the applied source-drain bias. At each new inclusion of a single-electron level between the Fermi energies of source and drain, the superconducting coherence peaks are replicated. This is a direct consequence of the discrete density of states on the quantum dot and was experimentally observed by Ralph *et al.* [124]. Despite the reasonable correspondence with the experimental data (see figure 3.9a), the presented theoretical framework is unable to describe the electron transport through a superconductor-quantum dot-superconductor device accurately. Especially around the replica's of the superconducting coherence peaks, the measured current deviates from the numerical result. The cause of this failure has its origin at Fermi's Golden rule used to calculate the single electron tunnel rates.

3.5 Hybridization at non-vanishing coupling

At the basis of the fore-going description of electron transport, we made the assumption that the tunneling of electrons could be considered as a weak perturbation of the system. Using the first order perturbation approximation, the full Hamiltonian can be written in a master equation form in which the transition rates are given by Fermi's Golden rule. Often in literature the validity of this approach is expressed in relative terms of the thermal energy $k_B T$ of the quantum dot and the tunnel coupling Γ i.e. $\Gamma \ll k_B T$. In fact this condition only applies specifically to a quantum dot coupled to normal leads. The general validity condition of the Fermi Golden rule requires that the variation in

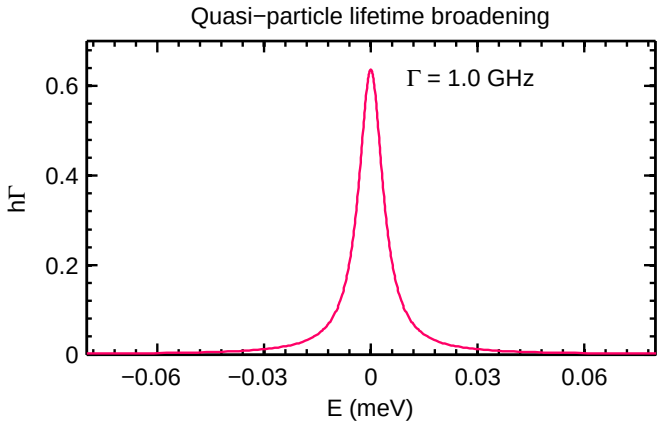

Figure 3.10: A single discrete level broadens when it is coupled to a continuum density of states. The typical width of the broadening is inversely proportional to the coupling strength.

the density of the final states in the leads is small compared to the tunnel coupling [20]. The origin of this condition can be illustrated nicely by regarding the so called *lifetime broadening* of the single-electron levels on the quantum dot which is a consequence of the finite tunnel coupling with a continuum density of states. A detailed derivation of the decay of discrete states can be found in Cohen-Tanoudji *et al.* [20], where they solve the system to infinite order in the perturbation theory. Here we will just reproduce the general reasoning of this derivation.

The unperturbed system to be considered is given by a single discrete state $|\phi_i\rangle$ and a set of states $|\alpha\rangle$ which form a continuum. Both are eigenstates of the unperturbed Hamiltonian H_0. Initially at time $t = 0$, we assume that the system is in the discrete eigenstate $|\phi_i\rangle$. Each final state $|\alpha\rangle$ is characterized by its energy E. We now add a constant perturbation T to the Hamiltonian, which only couples between $|\phi_i\rangle$ and $|\alpha\rangle$ i.e. $\langle\alpha|T|\phi_i\rangle = t_0$. Consequently the state $|\phi_i\rangle$ is no longer an eigenstate of system, and will evolve in time according to the new *perturbed* Hamiltonian i.e. $i\hbar|\dot{\psi}(t)\rangle = H|\psi(t)\rangle$. The probability of finding the system in the initial state $|\phi_i\rangle$ is simply given by the projection $|\langle\phi_i|\psi(t)\rangle|^2$. Under the assumption that the final states $|\alpha\rangle$ are available and their density $n(E)$ varies smoothly over $T \sim t_0$, the probability is given by $e^{-\Gamma t}$, where Γ is defined as

$$\Gamma = \frac{2\pi}{\hbar}\int dE|\langle\alpha|T|\phi_i\rangle|^2 n(E)\delta(E = E_{|\phi_i\rangle}). \tag{3.21}$$

Note that this equation is just the Fermi Golden rule for the tunnel rate between a single electron level and the lead. Equivalently one can get the probability of finding the system in the continuum state $|\alpha\rangle$ by the projection of the state $|\psi(t)\rangle$ on $|\alpha\rangle$ which is given by:

$$|\langle\alpha|\psi(t)\rangle|^2 = |\langle\alpha|t_0|\phi_i\rangle|^2 n(E)\left|\frac{1 - e^{-\Gamma t/2}e^{i(E-E_{|\psi_i\rangle}-\delta E)t/\hbar}}{\frac{1}{\hbar}(E - E_{|\psi_i\rangle} - \delta E) + i\frac{\Gamma}{2}}\right|, \tag{3.22}$$

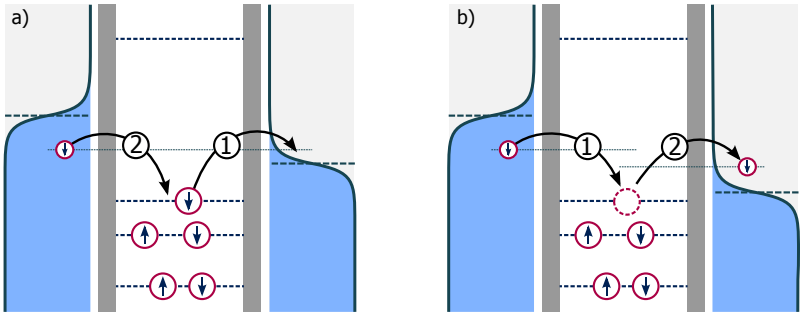

Figure 3.11: Higher order tunnel processes are leading when sequential tunneling is blocked by the charging energy. In second order processes, known as cotunneling, electrons can tunnel to and from the quantum dot, even if energy conservation is temporarily violated, provided that a second event 'restores' the quantum dot state. Cotunneling can be both elastic (a) or inelastic (b).

where δE is a shift in the single-electron level due to the coupling known as the Lamb shift[8]. The probability defined by eq. (3.22) gives the energy distribution of the final states after the decay of a discrete state into the continuum. This distribution, also known as the spectral density of the quantum dot, is shown in figure 3.10 for a discrete level coupled to a normal (constant) density of states. The typical width of the Lorentzian peak is proportional to the decay rate Γ, which clarifies the term *lifetime broadening*. In this picture, considering a discrete level coupled to normal leads, it becomes clear why Fermi-Golden rules applies in the limit when the thermal energy is much less than the coupling. In this regime the distribution of final states remains sharp as compared to the thermal variation of the Fermi-Dirac distribution.

However, if the discrete state is coupled to a superconducting density of states, its lifetime varies strongly as $E_{|\psi_i\rangle}$ approaches the superconducting gap edge. In the approach discussed above, $\Gamma \propto n_S(E = \Delta)$ diverges and the condition of validity of the Fermi Golden rules breaks down. In order to accurately describe the system beyond the first order approximation, one can to take into account higher order processes such as cotunneling (second leading order in the tunnel coupling). In principle such a system can be solved using the master equation approach [75]. Hereto one has to (1) expand the master equation up to higher order and (2) derive the tunnel rates using the T-matrix formalism. Although the higher order master equation is beyond the scope of this thesis [9], cotunneling itself can be described rather intuitively as the transfer of an electron from one to the other lead, through the virtual occupation of an intermediate state on the quantum dot. Figure 3.11 shows a schematic of a possible cotunneling process. An electron from an occupied level on the quantum dot can,

[8] When the continuum density of states is just a constant, like in normal metals, the Lamb shift reduces to zero.

[9] Possible starting points are: [28] (chap 4), [143]

even though energy conservation forbids it, spend some time (given by Heisenberg uncertainty relation) in the lead on the right. During this time, an electron from the other lead can tunnel into the, now unoccupied, level, resulting in the net transfer on an electron. Such virtual processes can either by elastic or inelastic and may in same cases involve spin flips (Kondo effect). If the electron spin is neglected, one can attempt to determine the cotunneling rates by inserting the tunnel Hamiltonian into the second order term in the T-matrix. However, the obtained rates diverge as the energy of the initial or final state become equal to the intermediate state energy. This divergence again arises because the perturbative approach does not take into account the lifetime broadening of the discrete [30].

An alternative approach is to calculate the electron current through a quantum dot by means of (non-)equilibrium Green functions. The use of Green functions allows one to solve the system beyond the perturbation approach. Although we won't detail the derivation, we will discuss the resulting equations and focus on their physical implications. Often these equations are obtained by representing the quantum dot by the Anderson model, which is just a two level (spin up/down) system. Using non-equilibrium Green functions, Meir *et al.* [98] derived the current-voltage relation for an Anderson quantum dot coupled to two normal leads. The resulting equation, which is essentially identical to the Landauer-Büttiker equation, expresses the current as an integral of the thermal occupation in the leads and the spectral density of the quantum dot *in presence of the leads*. Based on the same approach Levi Yeyati *et al.* [88] have derived a similar equation for an Anderson quantum dot coupled to two superconducting leads. Their result applies to the transport of quasi-particles between the two superconductors and is given by:

$$I(V) = \frac{4e}{h}\int_{-\infty}^{\infty} dE \frac{t_L n_L(E-\mu_L) t_R n_R(E-\mu_R)}{(E-\epsilon)^2 + \left(\sum_{i=L,R} t_i n_i(E-\mu_i)\right)^2} \times \Big(f_L(E-\mu_L) - f_R(E+\mu_R)\Big), \tag{3.23}$$

where n_i and f_i are respectively the superconducting density of states and the Fermi-Dirac distribution of the leads and ϵ is the energy of the bare quantum dot level. Using eq. (3.23) we can calculate the current through the quantum dot as a function of the applied bias and gate potentials. Figure 3.12a shows the current as a function of the applied source-drain bias for different coupling strengths. Notice that the $I(V) \propto n_S(E+eV)$ near the superconducting coherence peak is smeared as Γ increases. This is a result of the coherent (higher order) transport processes that can have both a positive and negative contribution to the current. Similar features are observed near the charge degeneracy points in quantum dots coupled to normal leads[75].

In the derivation of eq. (3.23), Levi Yeyati *et al.* have included only the continuum

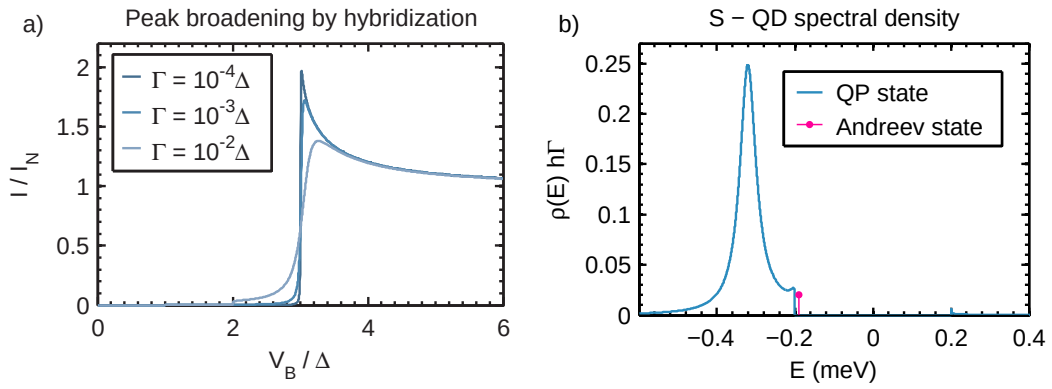

Figure 3.12: a) Current though a single level coupled to two superconductors as a function of the applied source-drain bias calculated with eq. (3.23). Increasing tunnel coupling softens the coherence peak. b) The spectral density of a single level is significantly altered when it is coupled to a superconducting density of states, i.e. (1) there is a broadened quasi-particle (QP) state and (2) a persistent discrete state (Andreev state) that remains bound in the superconducting gap.

part of the quantum dot's spectral density. It turns out there is also a discrete state (see figure 3.12b) appearing from the Green functions known as an Andreev state. The properties of this discrete state that is bound below the superconducting gap edge, will be discussed extensively in the next chapter as it is responsible for the non-stationary current in a superconducting single electron level turnstile.

Chapter 4

Stationary transport experiments

In this chapter we present measurements of the electron transport through quantum dot — superconductor hybrid devices performed under stationary conditions. A detailed study of the coherence peak broadening at Coulomb threshold shows that the electron transport is dominated by the quantum dot – lead hybridization whiled despite the weak tunnel coupling which is about equal to the thermal energy. The presence of sub-threshold resonances parallel to the CB diamond edges is consistent with earlier predicted higher-order Cooper-pair - electron (CPE) cotunneling processes.

Chapter contents

The presence of superconducting contacts in quantum dot devices significantly alters the electron transport through the quantum dot. In the strong coupling regime, the superconductivity of the lead introduces Andreev bound states in the spectral density of the quantum dot which can carry a supercurrent [53]. This mesoscopic proximity effect of quantum dots in the strong coupling regime has been studied thoroughly in the recent years [135, 118, 25, 72, 66, 119, 15]. Recently Winkelmann *et al.* [150] utilized the electromigration technique with gold-coated aluminium nano-junctions to contact C60 molecules. As opposed to pure aluminium junction, Al/Au leads result in a relativekly strong coupling to the quantum dot, which allowed the study of interplay between superconductivity and the Kondo effect in a single molecule.

Superconducting - quantum dot devices in the weak coupling regime have received much less attention. In the first report on the electron transport through weakly coupled S-QD-S devices, Ralph *et al.* [124] show the dramatic change in the $I(V_b)$ curves due to the superconducting density of states in the leads. The charging energy and level spacing in these devices remain limited as the quantum dot are obtained by metal clustering during top-down deposition.

In the work of this thesis we study the effect of superconducting (aluminium) contacts on the quantum transport through small gold nano-particles (~ 4 nm). In the weak tunneling regime, one can expect to obtain a spectral resolution which is not limited by the electronic temperature, provided that the superconducting gap is larger than k_BT. We will show that in this regime, the spectral resolution becomes limited by the hybridization between the superconducting coherence peaks and the single electron levels on the quantum dot, as was previously predicted [88]. The electro-migration process described in section 1.5 allows us to obtain pristine superconductor - quantum dot - superconductor devices. The statistical nature of electro-migration results in devices with varying lead - quantum dot coupling strengths.

4.1 Device zoology

The superconducting contacts to the quantum dots are fabricated by the in-situ electro-migration of aluminium nanowires in cryogenic vacuum at 4K. To avoid the necessity of breaking the vacuum after electro-migration, which will result in the instantaneous oxidation of the nano-gaps, we deposit gold nano-particles prior to the electro-migration. Directly after electro-migration we characterize the junctions by measuring the current at a fixed small bias voltage (typically 5 mV) as a function of the gate voltage. The resulting traces can be categorized in three different groups. In most cases the junctions show a small, but gate-independent current over the full gate range (-9V to +9V). The zero-bias resistance of these devices ranges from hundreds of kiloohms to various gigaohms. Although the possibility of a nano-particle well tuned far from its degeneracy

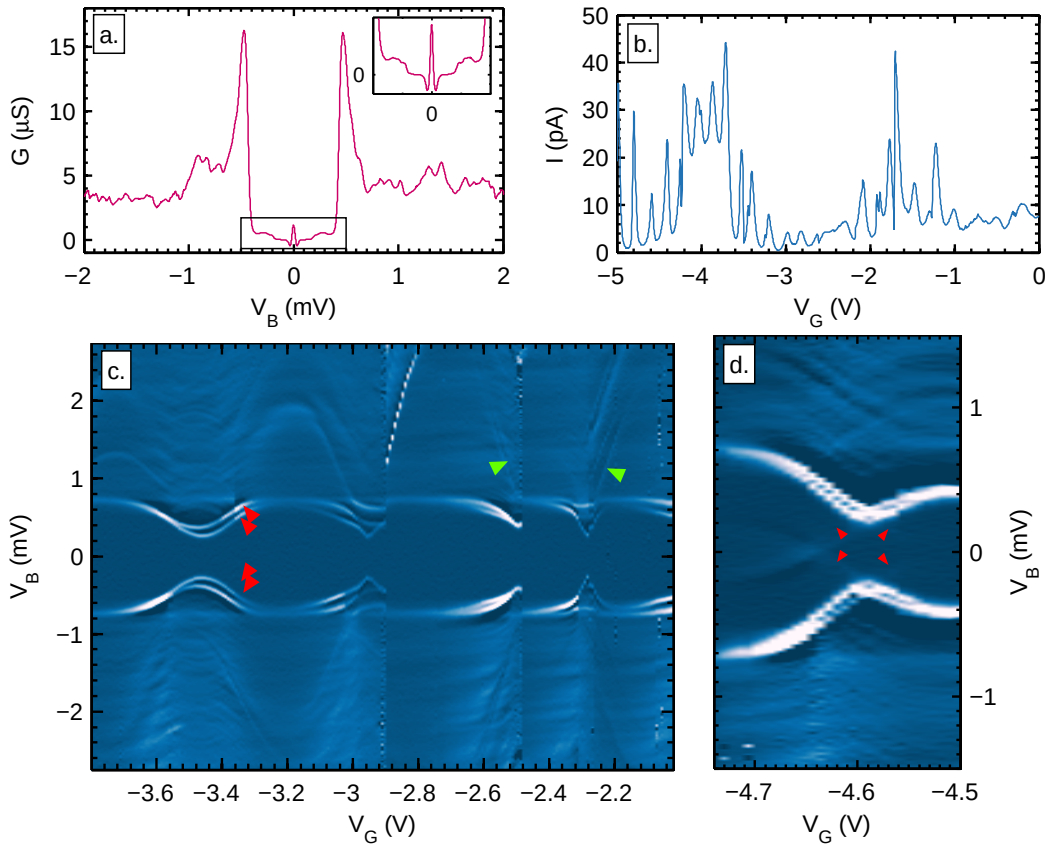

Figure 4.1: a) Example trace showing the gate independent conductance profile (numerical derivative) of a SIS tunnel junction (T = 100 mK) with signatures of Josephson current and multiple Andreev reflections. b) DC current trace in another device (V_B = 3 mV, T = 4 K) as function of gate voltage, which shows strong and closely spaced current oscillations. Further conductance measurements at 100 mK (c, d) reveal the existence of Andreev bound states (indicated by the red arrows) and faint resonances (green arrows) of a quantum dot in Coulomb blockade.

points can not be ruled out, it is more likely that these devices are just tunnel junctions. This goes generally with the observation (at T = 100 mK) of a gate-independent critical current and signatures of multiple Andreev reflections in the more conductive junctions (see figure 4.1a). About equally often, the traces show a gate dependent current drowned in many randomly occurring jumps. Repeating the measurement in these cases generally results in completely different gate traces. This instability of the current is possibly the result of many gold nano-particles in the vicinity of the nano-gap. The random charging of nano-particles mutually effects their conductance. In about 4 percent of all 322 measured junctions, the traces show a reasonably stable and reproducible gate dependent current. Again these 14 devices can be categorized into three sub-groups.

We have measured three devices that show very broad peaks as a function of the gate. The current maps of these devices (measured at T = 100 mK) show vague

Coulomb structures with a significant conductance in the Coulomb diamonds and a suppression of current in the superconducting gap between $\pm 2\Delta$. A small charging energy of about 10 meV and the absence of single electron levels point to a large island in between the superconducting leads. We have not observed an increase of the gap in the conductance, which indicates that the islands are not superconducting.

In yet another gourp of three devices we observed strong oscillations in the device conductance as a function of the gate at 4K (see figure 4.1b). Although the oscillations look very similar to Coulomb oscillations, additional measurements of the conductance at base temperature reveal a more complex picture involving the formation of Andreev bound states in a quantum dot coupled to a superconducting reservoir [135, 84, 118, 25, 119]. Figure 4.1c shows a differential conductance map in which the Andreev states are clearly visible (indicated by red arrows). The existence of two close lying bound states of similar behaviour could indicate of the presence of two nearby quantum dots [119]. On the right side of the figure one can distinguish the faint slanted lines (green arrows) indicating the Coulomb diamond and exited states of a weakly coupled quantum dot ($\delta \approx 400\mu eV$). In a different gate regime, but on the same device, we observe yet another set of Andreev bound states (see figure 4.1d). There are two bright resonances (4 when taking into account the symmetry around zero bias) that extend down to $|V_b| \approx 0.2\,\mathrm{mV}$, from where they are continued by much weaker resonances crossing at zero bias (indicated by the red arrows). Unfortunately these samples could not be studied in more detail. The Andreev bound states are most likely formed due to a strong coupling between the quantum dots and one of the superconducting gap-edges (which makes phase biasing impossible). The coupling between the second superconducting lead and the quantum dots is much weaker and can thus be considered as a superconducting tunnel probe with which we measure the spectral density of the quantum dot. Kumar *et al.*[84] have reported results of a similar measurement, which are consistent with our observations.

In the remaining 8 devices (third sub-group) we observe sharp and stable Coulomb peaks at T = 4K as shown in figure 4.2. In most cases there are conductance peaks of various heights, as is illustrated by the inset in figure 4.2. This might indicate the existence of multiple particles (in parallel) in the nano-gap, which can be expected due to the dense nano-particle dispersion used. The presence of many particles is in principle not problematic, provided that it does not result in an unstable electrostatic environment. Additional measurements at 100 mK of the conductance around the Coulomb oscillations show clear Coulomb diamond structures (see figure 4.3). In this chapter we shall characterize the electron transport through these 8 devices of interest.

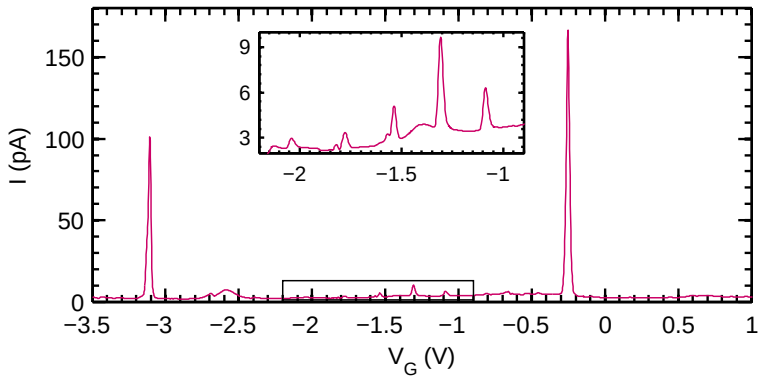

Figure 4.2: Example DC current trace (V_B = 3 mV, T = 4 K) as a function of the gate voltage. The $I(V_G)$ curve show sharp Coulomb oscillations. Often there are peaks of various shapes and height present, which might indicate the co-existance of multiple gold-nanoparticles inside the nano-gap.

4.2 Quantum dot Coulomb blockade analysis

The mapping of the device conductance at low temperature as a function of both the gate and bias source-drain potential can reveal a great amount of information about the device parameters. In weakly coupled devices, these maps will shows the typical Coulomb diamonds of zero conductance separated by regions of finite conductance. From the shape of the Coulomb diamonds one can determine the asymmetry in the capacitive coupling of the source and drain electrodes, the gate coupling parameter, the charge degeneracy points and the charging energy of the particle [7, 142].

The two slopes of a diamond are given by $\beta = C_G/\left(C_D + C_G\right)$ (positive slope) and $\beta' = C_G/C_S$ (negative slope). The asymmetry in the capacitive coupling of the source and drain can be expressed by the ratio of the source and drain capacitance which is given by:

$$\frac{C_D}{C_S} = \beta'\left(\frac{1-\beta}{\beta}\right) = S_C. \tag{4.1}$$

The gate coupling parameter, which expresses the effective change in island potential per unit volt applied to the gate electrode, is related to the diamond slopes by $\alpha = C_G/C_\Sigma = \left(\beta'^{-1} + \beta^{-1}\right)^{-1}$. For small quantum dot devices, the gate coupling strength ranges from less than one percent up to several percent's depending on the gate insulation used [108]. In single electron transistors with a large normal island, the gate coupling is generally much stronger due to the larger size of the island.

Together the source-drain asymmetry and the gate coupling parameter are helpful tools in the identification of Coulomb diamonds in case there are many different particles present between the source and drain electrode. Each particle is characterized by its

#	E_C^{min}	R_{SH}	α	C_D/C_S	I_+, I_-	γ_l, γ_r
	meV	MΩ			pA	GHz
A	35	135	0.35	0.45	3.70 / 2.8	0.047, 0.021
B	10*	26	0.03	1.03	1.77 / 1.82	0.016, 0.018
C	50*	500	0.05	0.70	166 / 92	7.94, 0.596
D	120*	1000	0.09	1.07	290 / 250	3.232, 2.06
E	70*	480	0.27	0.35	4.08 / 1.31	...
F	12*	790	0.10	3.00	3.91 / 1.48	...
G	2.5*	5	...	0.31	250 / 178	3.93, 1.29
H	50	17	...	...	1.37	...

Table 4.1: Charging energy, shunt resistance, gate coupling, capacitive asymmetry and tunnel coupling (in rates) to the source and drain leads derived from the current at large positive and negative bias. For some devices (denoted by the asterisks), only a lower bound on the charging energy can be given. Data is extracted from various measurements on 8 different devices performed at $T \approx 80$ mK.

capacitances to the three electrodes, resulting in distinct diamond shapes. Based on the analysis of the diamond slopes one can identify and group the diamonds belonging to the same particle. Once the Coulomb diamonds are identified, one can extract the charging energy from the size of the diamond i.e. the horizontal (vertical) extent of a Coulomb diamond is given by $E_{add}/(\alpha e)$ ($4E_{add}$), where the addition energy, E_{add} is given by the sum of the charging energy E_C and the level separation δ, i.e. $E_{add} = 2E_C + \delta$.

Figure 4.3 shows a selection of conductance maps at low temperature ($T \approx 100$ mK) of the 8 selected devices in the superconducting state. Often we are not able to measure the full extend of a diamond as the accesible gate range (determined by α and the gate break-through voltage) is too small compared to the large charging energy. In these cases we center the measurement range at the charge degeneracy point. The maps clearly show slanted lines that are characteristic to Coulomb diamonds. The superconducting gap in the leads appears as a strong suppression of the conductance at small bias i.e. $I \approx 0$ when $eV_B < 2\Delta$. In the majority of the devices, we observe a finite (instead of zero) conductance inside the Coulomb diamonds (but at $|eV_B| > 2\Delta$). This current can be attributed to either direct tunneling between the leads characterized by a shunt resistance R_{SH}. In the next section we will address this feature in more detail. In the conductance maps with an asymmetry in the Coulomb diamonds we observe a small displacement between the two opposite apexes of the conductive regions as can be seen in figure 4.3d. This is a direct consequence of the current suppression due to the superconducting gap in the leads which becomes apparent with asymmetric capacitive coupling of the leads to the quantum dot. The true charge degeneracy point lies in the middle of these two apexes.

In table 4.1 we list the values of the charging energy, the asymmetry in the capacitive coupling with the leads and the gate coupling parameter of the 8 selected devices. There

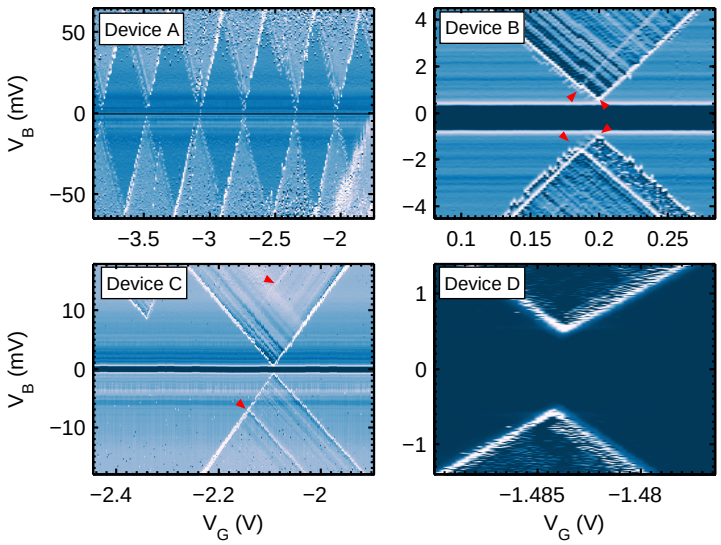

Figure 4.3: Color maps of the differential conductance measurement in four devices (A, B, C, D) at base temperature ($T \approx 80$ mK). Coulomb diamonds measured in most devices (denoted by an astrix in table 4.1), e.g. (b-d), extend beyond the scope of the measurements. Additional slanted lines (indicated by red arrows) outside the Coulomb diamonds observed in some devices indicate single quantum dot levels (excitations) with an energy spacing that varies between 2 and 10 meV.

is quite some variation between the device parameters as can be expected due to the electro-migration process. In all devices we observe a large charging energy ($E_C \gg 1$ meV) and a small capacitive asymmetry that does not exceed a factor 3. For only two devices we were able to measure to full extent of the Coulomb diamonds. For the other devices we quote a lower bound on the charging energy given by the maximum source-drain bias that we have applied. On average the gate coupling is about 5 percent, which is consistent with the presence of a small nano-particle between the lead. In two devices (A and E) we observe a remarkably high coupling (> 0.25). In these cases we possibly measure the transport through a weakly coupled aluminium, though not superconducting, grain.

Besides the capacitive parameters of a device, the conductance map can also reveal the energy spacing between the single electron levels of the quantum dot. The levels appear in the conductance map as lines parallel to the diamond edges. The energy spacing between the first unoccupied level (the diamond edge) and higher energy levels is given by $e\Delta V_b - 2\Delta$, where ΔV_b is the source-drain bias at which the lines of the higher energy levels and the diamond edge intersect. In 7 of the 8 devices that we have studied, we observe some clear lines (indicated by the arrows in figures 4.3b and 4.3c and running parallel to the Coulomb diamond edge. The energy spacing between these lines lies between 1.5 and 10 meV but varies strongly from sample to sample. The observed level spacing $\delta = \frac{2\pi^2\hbar^2}{mk_F V}$ (where V, m and k_F are respectively the QD

volume, electron mass and Fermi momentum) corresponds to gold nano-particles with a diameter between 2.9 and 5.4 nm [149], which is consistent with the gold nano-particles that we have used. In addition to these clear lines, we also observe many equally spaced but faintly visible lines with a much smaller energy spacing of about 170 μeV on average. The origin of these lines is most likely found at the vibrational modes of the nano-particles [108].

4.3 Tunnel couplings and broadening of the transport features

Possibly the most striking feature in the electron transport through superconductor - quantum dot - superconductor devices is the replication of the superconducting coherence peaks at every inclusion of a new transport channel between the Fermi-energies of the leads [124]. Following the sequential tunneling model, the shape of the replicas is identical to the BCS coherence peaks and therefore has infinite height. Any rounding of the peaks measured in experiments may therefore be related to external effects such as the noise in the environment or non-equilibrium excitations [124]. However it was shown by Levi-Yeyati *et al.* [88] that the peaks are also rounded by coherent effects due to the interaction (hybridization) between the quantum dot level and the superconducting density of states in the leads (see section 3.5). In the 8 devices that we have studied in detail, we observe different currents ranging from a few pA to 0.3 nA (see table 4.1), which can be an ideal basis to study the effect of the coupling strength on the 'coherence peak' shape in the $I(V_B)$ curves.

4.3.1 Characterization of sub-threshold conductance

In some devices however, we observe a significant gate-independent device conductance within the Coulomb diamonds. In order to study the tunneling coupling between the leads and the quantum dot, the nature of this current contribution has to be characterized such that it can be taken into account. As inelastic cotunneling can be eliminated[1] and elastic cotunneling is accounted for in the model of Levi-Yeyati, we focus on the possible current contribution from direct tunneling between the superconducting leads. Such a shunt current is possible as the electro-migration gap most likely has a varying size along the trench. Assuming that the shunt current is described by a simple SIS model we fit the sub-threshold current with the following equation

$$I(V) = \phi(\sigma_N) * \frac{1}{eR_N} \int n_l(E) n_r\big(E - eV\big)\Big(f_l(E) - f_R\big(E - eV\big)\Big) dE, \qquad (4.2)$$

in which the tunnel current between two superconductors (characterized by their Fermi-Dirac distributions f_i and density of states n_i) is convoluted with a Gaussian distribu-

[1] The conductance is constant with bias as opposed to conductance resonances at non-zero bias

tion $\phi(\sigma_N)$ to account for white voltage-noise (see figure 4.4a). Since the sub-threshold current can have contribution from both elastic cotunneling and the direct SIS shunt, we only fitted the sub-threshold current measured far away from the charge degeneracy point as to suppress the contribution from elastic cotunneling.

However, as for most devices it is difficult to obtain a decent fit of the data, we construct a reference curve that represents the SIS shunt. This is done by taking the average of various $I(V_b)$ curves measured far from the charge degeneracy point. In order to obtain a value for the shunt resistance we fit the linear part beyond $eV_b = 2\Delta$ (see table 4.1). In the following analysis of the measured current traces at (or close to) the charge degeneracy points, we have corrected the current according to the SIS shunt resistance in order to study the current flowing solely through the quantum dot.

4.3.2 Tunnel coupling by tail-current analysis

When the current through the device is supported by a single spin degenerate electron level, one can determine the coupling strength to the lead electrodes from the measured current through the device in the on-state. The relation between the current at large bias and the coupling is given by:

$$\begin{aligned} I_+ &= 2e\frac{\gamma_l\gamma_r}{2\gamma_l+\gamma_r} \\ I_- &= -2e\frac{\gamma_l\gamma_r}{\gamma_l+2\gamma_r}, \end{aligned} \tag{4.3}$$

where $\gamma_{l,r}$ is the bare coupling strength to the left and right electrodes. These equations are obtained by solving the master equation (eq. 4.3.2) for a single spin degenerate electron level [13]. In the derivation it is assumed that the bias is much larger than k_BT, and the density of states in the leads is constant. This latter condition is in the case of superconducting leads only valid far beyond the superconducting coherence peaks.

The positive and negative single electron level current and the coupling to the leads are listed in table 4.1. In the devices E and F, we can not determine the coupling rates. In these devices, we measure a positive and negative current with a ratio > 2, which indicates that the current is not supported by a single spin-degenerate conduction channel. It is possible that in these devices the level spacing is much smaller than the induced noise by the environment.

4.3.3 Analysis of the coherence peak broadening

As the coupling strength and asymmetry are now known, we can cross-reference the coupling parameters to the shape of the first coherence peaks measured at charge

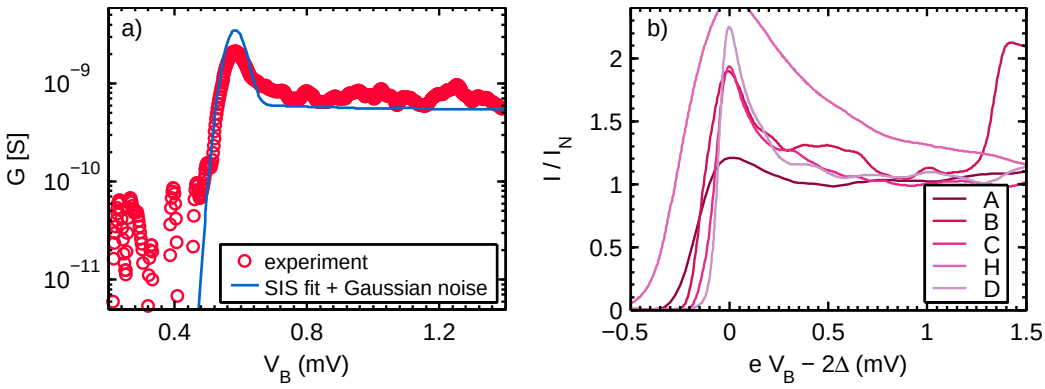

Figure 4.4: a) SIS shunt conductance as a function of bias, (partly) responsible for the non-zero conductance inside the Coulomb diamonds (see figure 4.3). The $I(V_B)$ of the SIS shunt can be fitted by a model for a SIS tunnel junction convoluted with Gaussian noise ($R_{Sh} \approx 1.9\,\mathrm{G}\Omega$, $\sigma_N \approx 30\,\mu eV$). b) Normalized (to the 'normal state' current) $I(V_B)$ traces measured at the charge degeneracy point of 5 different devices ($T \approx 80$ mK) showing replica's of the superconducting coherence peak. The light-to-dark color-coding corresponds to decreasing tunneling coupling.

degeneracy. In figure 4.4b we show the normalized current (corrected from any shunt current) as a function of V_B for 5 selected devices. The curves are light-to-dark color-coded according to decreasing tunneling coupling. Although we do observe a qualitative difference between the peaks, similar to the peak rounding that we expect from level-lead hybridization *et al.*, we can not identify a clear relation with the coupling strength. In order to further study the peak shape, we fit the $I(V_B)$ traces of devices C and D with three models which each represent a possible origin of the peak broadening i.e. 1) voltage-noise, 2) photon-assisted tunneling and 3) the level-lead hybridization.

Peak broadening by voltage noise

The starting point of the first two models is the current-voltage relation derived from the master equation of a single level system as is given by eq:

$$I = \frac{2e}{h}\tilde{\gamma}_l\tilde{\gamma}_r \frac{f_l(\epsilon,\mu) - f_r(\epsilon,-\mu)}{\tilde{\gamma}_l\big(1 + f_l(\epsilon,\mu)\big) + \tilde{\gamma}_r\big(1 + f_r(\epsilon,-\mu)\big)}. \tag{4.4}$$

In this equation[2] we have used the effective tunnel coupling $\tilde{\gamma}_i$ between the level (characterized by its electro-chemical potential ϵ) and leads which is given by $t_o^i n_i(\epsilon,\mu)$, in which t_0 is the matrix element of the tunnel Hamiltonian and n_i is the lead density of states. We assume that the electrons in the leads are well thermalized and can be described by a Fermi-Dirac distribution f_i centred around the electro-chemical potential of the leads $\mu = \pm\frac{eV}{2}$. The final current-voltage relation of the first model ('Seq+Noise') is obtained by the convolution of eq. 4.4, in which we take a pure BCS density of states

[2]Note that equation 4.3 can be obtained from this equation at high positive and negative bias.

to describe the leads, and a Gaussian profile to account for the white voltage noise characterized by its standard deviation σ_N, which is taken as a fitting parameter.

Photon-assisted tunneling and Cooper-pair breaking

In the second model ('Seq+Dynes') it is assumed that the peak shape is broadened by photon-assisted tunneling and/or Cooper-pair breaking. Both processes can give rise to an effective broadening of the coherence peaks. In the former process, electrons that normally have insufficient energy absorb a photon from its dissipative environment and enter the empty branch of a superconducting lead. It was shown by Pekola *et al.* [115] that this environment-assisted tunneling results in the sub-gap conductance of SINIS devices and can be well described by an effective broadening of the superconducting density of states, identical to the Dynes model which is normally used to describe the peak broadening by a finite Cooper-pair recombination time. In a similar way, we can account for the photon-assisted tunneling in our system by substituting the effective lead density of states $n^D(E)$ (as given in eq. 4.5), characterized the Dynes parameter η (taken as fitting parameter), into eq 4.4.

$$n^D(E) = \left| \Re \left(\frac{E + i\eta\Delta}{\sqrt{(E + i\eta\Delta) - \Delta}} \right) \right| \tag{4.5}$$

Quantum dot - lead hybridization

Finally, in the third model ('Hybrid') we use the current-voltage relation of Levi-Yeyati *et al.* [88] which accounts for the hybridization of the quantum dot level and the superconducting leads. In this model there are no additional fitting parameters besides the superconducting gap Δ and the tunnel coupling γ. The electro-chemical potential ϵ of the quantum dot level is in principle not an independent parameter as is it determined by both the gate and bias potentials. To account for the contribution of the applied bias we use the previously obtained capacitive asymmetry i.e.

$$\epsilon = \epsilon' + \frac{eV_B}{2}(1 - \alpha)\left(\frac{1 - S_C}{1 + S_C}\right), \tag{4.6}$$

where $S_C = C_D/C_S$ is the asymmetry in the capacitive coupling and ϵ' is the gate dependent detuning of the quantum dot level with respect to the charge degeneracy point. Furthermore we can reduce the number of fitting parameters by using the coupling asymmetry obtained from the analyses of the Coulomb diamond shape.

Discussion of the fit results

Figures 4.5a and 4.5b show the measured data and the best fitting curves obtained by the models. To illustrate both the sub-threshold current and the peak shape we present

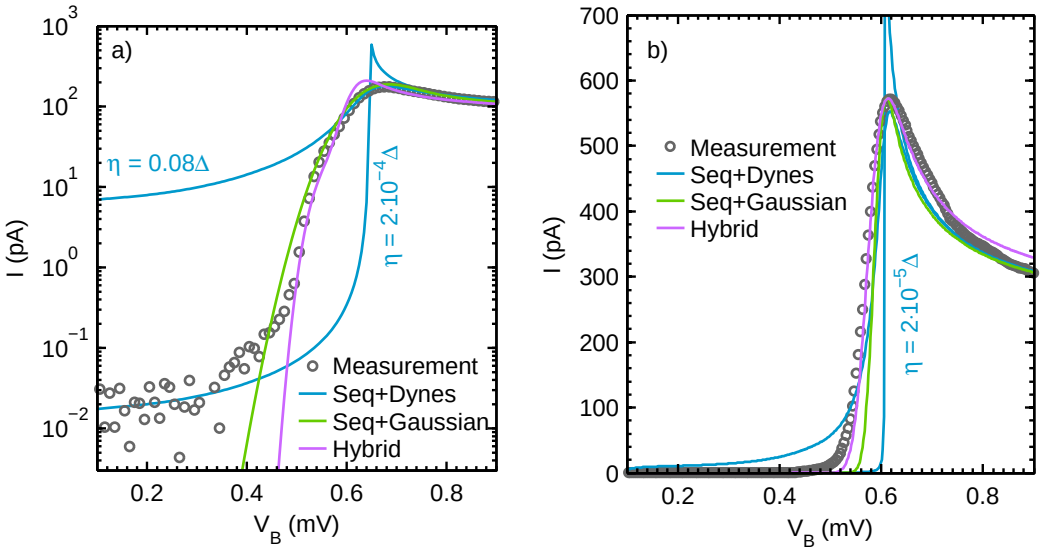

Figure 4.5: Sub-gap current and the coherence peak shape of device C (a) and device D (b). The $I(V_b)$ curves are fitted with three models that can explain the peak broadening and non-zero sub-gap current. The fit parameters for both device are listed in table 4.2

the results of device C and D differently i.e. for device C on a log scale (figure 4.5a) and for device D on a linear scale (figure 4.5b). The fit parameters for both device are listed in table 4.2. In the following discussion we will focus of the fit quality of the subgap current and the coherence peak.

First of all, it is visible that 'Seq+Dynes' model clearly fails to fit the data around the peak and below the current threshold. The observed broadening of the peak requires such large Dynes parameter that the sub-threshold current becomes much larger than observed (indicated by blue arrow in 4.5a). Optimizing the fit in for the sub-gap regime shows that the sub-gap current is limited by noise. This put an upper bound to the Dynes parameters i.e. $\eta < 10^{-5}\Delta$. We can thus conclude that our measurements are are not dominated by the device environment. This statement is of utmost importance if the device is used as an single level turnstile [115, 159, 90] as we will do in chapter 6.

The 'Seq+Noise' model shows a better correspondence with the data, especially around the coherence peak, but strongly overestimates the sup-gap current. Additionally for device C we need an unrealistic high noise value of 50 μeV to fit the peak shape, which is inconsistent with the previously obtained value ($\approx 30\mu eV$) from the fit of the SIS shunt.

Finally we observe that the 'Hybrid' model gives the best correspondence with the data. The broadening of the coherence peaks is captured reasonably well without results in an overestimated sub-gap current. This indicates that the broadening in the transport features are dominated by the quantum dot-lead hybridization rather then temperature or inelastic scattering events [1]. We can further improve the fit by

Model, device	$\Delta\,[\mu\text{eV}]$	$(\gamma_l, \gamma_r)/\Delta$	$\sigma_N\,[\mu\text{eV}]$	η/Δ
Seq+Noise, C	265	0.04, 0.0053	50	n.a.
Seq+Dynes, C	265	0.04, 0.0053	n.a.	0.03
Hybrid, C	270	0.032, 0.0042	n.a.	n.a.
Seq+Noise, D	265	0.035, 0.043	30	n.a.
Seq+Dynes, D	265	0.035, 0.043	n.a.	0.03
Hybrid, D	260	0.023, 0.028	n.a.	n.a.

Table 4.2: Parameters of the three models used to fit the $I(V_b)$ curves shown in figure 4.5.

included a small amount of voltage noise ($\sigma_N \approx 20\mu eV$) modelled by the convolution of the 'Hybrid' model with a Gaussian distribution.

In both devices we obtain a coupling strength from the 'Hybrid' model fit which is lower than what we obtain by the current analyses at large bias (eq. 4.3.2). At this point it should be reminded that eq. 3.23 is derived based on the Anderson model which is solved by the use of Green functions. In such a model, the charging energy is incorporated in an effective level spacing of the Anderson dot. This however, does not fully take into account the sequential nature of the transport in the weak coupling regime and consequently the occupation probability P_α of the 'resonant' level which is in fact dependent on the bias. Therefore, to further improve the hybrid model, one could take into account the average occupation probability $P_\alpha(V_B)$, as was proposed by Kang [63].

4.3.4 Coherent sub-threshold current

The correspondence between the data and the 'Hybrid' model becomes even more striking when we fit the full $I(V_B)$ traces of device D at various gate positions close to the charge degeneracy point. In the sub-threshold regime the current is determined by the SIS shunt and elastic cotunneling. As we have subtracted the contribution of the SIS shunt, any leftover sub-threshold current is related to elastic cotunneling which is taken into account by the 'Hybrid' model.

Figure 4.6 shows the measured $I(V_B)$ traces (in red) before subtracting the current contribution by the SIS shunt as to illustrate the difference between the gate-independent SIS shunt (dash-doted line) and the coherent sub-gap. Traces obtained by fitting the 'Hybrid' model are added to SIS shunt and shown in blue. All fitting curves are obtained with equal fitting parameters except the level detuning with the gate. In order to obtain this set of fitting curves, we had to use slightly different values for the asymmetry in the capacitive and tunnel coupling (respectively 0.85 and 0.09 instead[3] of

[3]The asymmetry in the capacitive coupling was obtained form the Coulomb diamond analysis. The asymmetry in the tunnel coupling was obtained from fitting the $I(V_B)$ traces at charge degeneracy.

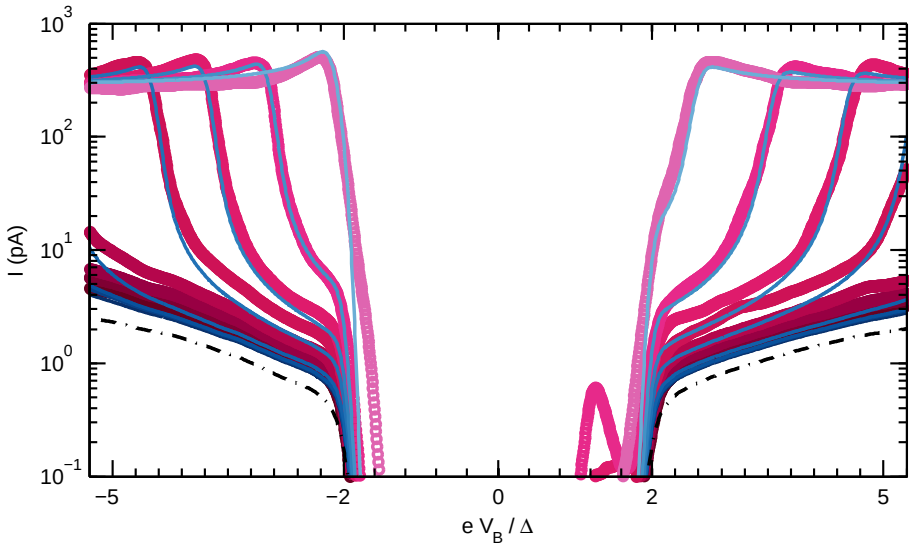

Figure 4.6: Sub-gap current at varying detuning (ΔV_G = −10.8, −9.3, −7.8, −6.3, −4.8, −3.3, −1.8, −0.3 mV) from the charge degeneracy point as a function of V_B. Measured traces in device C (in red) are fitted with the 'Hybrid' model shown in blue ($T \approx 80$ mK). All fit parameters, except the gate detuning, are equal for each curve (S_D = 0.096, (γ_l, γ_r) = $(0.033\Delta, 0.039\Delta)$, Δ = 285 μeV, σ_N = μeV). The dash-dotted lines represents the experimental SIS-shunt which contribution was accounted for in the fitting procedure.

0.81 and 0.03) and the coupling strength (0.025Δ instead[4] of 0.023Δ). Overall we find a good correspondence between the measured data and the obtained fitting curves. Close to the charge degeneracy point, the fitting curves overestimate the sub-gap current a little, but with increasing detuning from the charge degeneracy point this overestimation becomes less and we obtain an excellent correspondence. This decreasing difference between the observed and modelled sub-threshold current can possibly be attributed to the over-simplification in the 'Hybrid' model as was previously discussed.

Hybridization and tunnel coupling asymmetry

Another interesting feature in the $I(V_b)$ traces is the evolution of the peak shape with increasing detuning from the charge degeneracy point as shown in figure 4.7 on a linear scale. In device D (figure 4.7a) we observe a decreasing peak height as we detune the gate further away from the charge degeneracy point. The decrease in peak height is similar on positive and negative bias. In device C (figure 4.7b) we observe a more dramatic change in the peak shape when we detune the gate. The coherence peak at positive bias nearly disappear when the gate is tuned below the charge degeneracy point, while the coherence peak at negative bias below more pronounced. The dramatic modification of the peak shape is due to the asymmetry in the tunnel coupling. When the single electron level is aligned on one side with the coherence peak of the strongly

[4]The tunnel coupling was obtained from fitting the $I(V_B)$ traces at charge degeneracy.

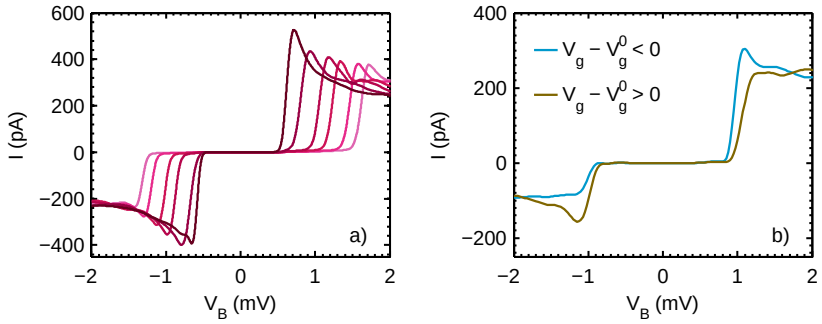

Figure 4.7: The peak shape is strongly dependent on the gate detuning from the charge degeneracy point. a) In device D, which has a rather symmetric tunnel coupling, the peak deforms symmetrically on the reversal of source-drain bias as the gate is detuned from the charge degeneracy point. b) In device C, which has a rather strong tunnel coupling asymmetry, the peak deforms asymmetrically upon the reversal of the bias.

coupled lead and beyond the coherence peak of the weaker coupled lead, the spectral density of the dot is strongly broadened into a Lorentzian shape and the line shape of the $I(V_b)$ trace is similar to that of a quantum dot coupled to a normal lead.

While there are many reports on experiments with weakly coupled superconducting-quantum dot device, this is the first quantitative study of the shape of the transport features around the current threshold. From the analyses of these features, we get a comprehensive picture of the coupling and the resulting quantum dot-lead hybridization. We have shown that the sub-threshold transport and the coherence peak shape are dominated by this hybridization which is important when operating the device as a single level turnstile (see section 5.4).

4.4 Cooper-pair — electron cotunneling

In the previous sections we have shown that the electron transport through our devices can be well described by the sequential tunneling model which applies to devices in the weak coupling regime. So far we have focussed the discussion on the transport of quasi-particles as the transport of Cooper-pairs is believed to be strongly suppressed by the weak coupling. However, Johansson *et al.* [58] predicted the existence of sub-threshold transport features in weakly coupled superconductor-quantum dot devices, due to the coherent tunneling of a Cooper-pair and an electron that manifest even at arbitrary high bias voltages. Here we report on the first observation to the best of our knowledge, of this contribution to the transport in S-QD junctions.

The intuitive picture of this pair current is given by the sequential breaking of a Cooper-pair in one lead followed by the cotunneling of the resulting quasi-particles as is illustrated in figure 4.9a. This process known as Cooper-pair — electron (CPE) cotunneling can only occur when $V_B > \pm\Delta$ and becomes resonant when the quantum

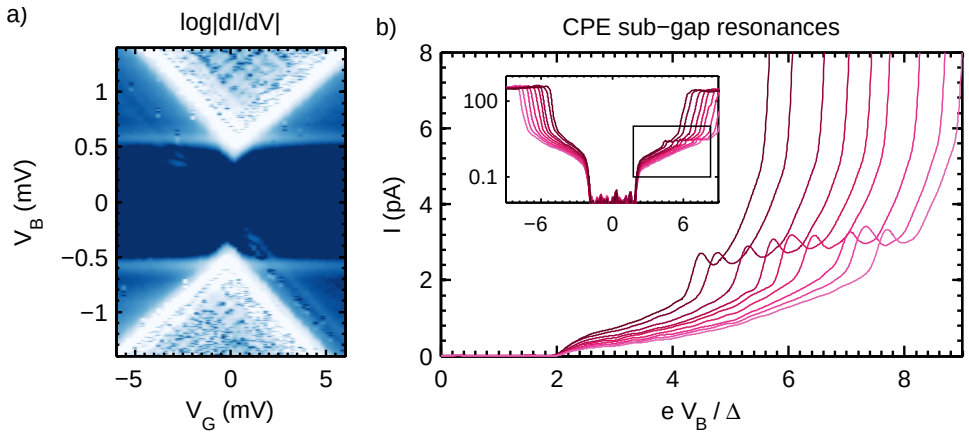

Figure 4.8: In devices C and D, there is a small local increase in the conductance positioned parallel and just below the Coulomb diamond edge.

dot level is aligned with the Fermi-energy of one of the superconducting leads. In the case of a symmetric tunnel coupling between the quantum dot and the leads one would expect a local increase of the conductance just below the Coulomb diamond edges as is visible in figure 4.9b. Note that the expected sub-threshold lines are located parallel to the Coulomb edges at a distance equal to the superconducting gap. This behaviour is consisted with the sub-threshold features that we observe in device C and D as shown in figure 4.8b. The contribution of CPE cotunneling appears as a small peak on top of the sub-threshold current located just below and aligned with the slopes of the Coulomb diamonds. In the conductance map (see figure 4.8a) of these devices, these peaks appear as faint lines parallel to the Coulomb edges. Around the charge degeneracy point the lines disappear abruptly when the source-drain bias is below the superconducting gap i.e. $|V_b| < \Delta$, which relates this feature unambiguously to the involvement of Cooper-pairs. Rather remarkably we observe the pair current contribution only on one side of the Coulomb diamond which could be related to charge parity or the asymmetric tunnel coupling with the leads.

4.5 Magnetic field dependence

The application of a magnetic field often changes the electronic properties of mesoscopic systems. For example it can drive superconductors to their normal state [144], split the spin-degeneracy of quantum levels [83] and introduce 1D conduction channels in 2DEGs known as Landau Edge states [33]. More recently it was shown that the application of a small magnetic field improves the performance of SINIS electronic coolers by the enhanced thermalization of out-of-equilibrium quasi-particles in the superconductors [112]. In this work, the reasons to study the electronic properties of our devices under a magnetic field are threefold. As to verify the origin of the observed

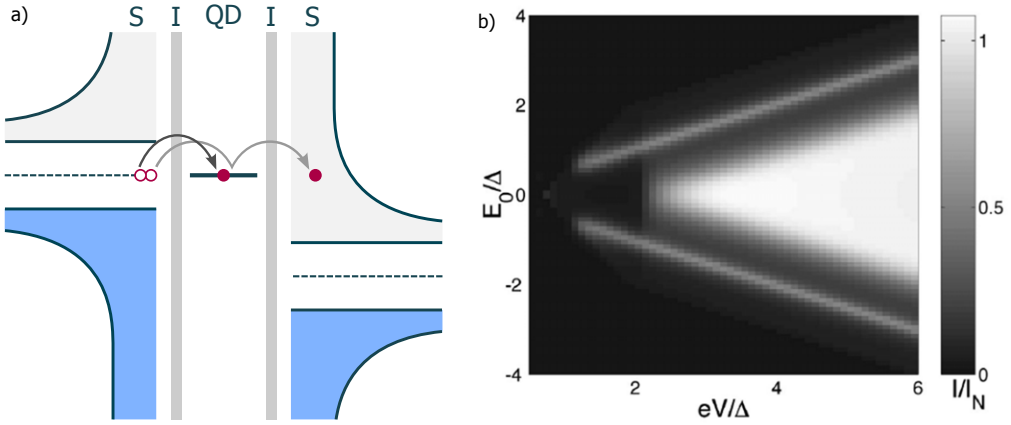

Figure 4.9: a) Schematic representation of the pair-current process observed in device C and D. Cooper-pairs in the left lead split after which transport is possible by quasi-particle co-tunnelling. This process gives rise to a local increase of the conductance located parallel to the Coulomb diamond edge ate at distance equal to two times the superconducting gap as is shown in the conductance map (b, extracted from [58]).

spectral gap to be superconducting rather than phonon blockade [17, 87, 134], we drive the superconducting leads to their normal state. By gradually increasing the magnetic field, we can verify that the pair-current line, observed in figure 4.8, coincides with the Coulomb diamond edge in the normal state. Furthermore we search for signatures of charge number parity, either in the Kondo effect or the Zeemann splitting of the Coulomb diamond edges.

4.5.1 Suppression of the superconducting gap

Figure 4.10 shows the conductance maps of device C around its charge degeneracy point measured at varying magnetic fields from zero to 600 mT at which we observe a clear suppression of the spectral gap. To illustrate the difference in the conductance between the superconducting state and the normal state of the device, we show the conductance map measured at 600 mT directly next to the conductance at 0 mT. Furthermore we observe that the superconductivity in the two leads is destroyed at different magnetic fields. The reduction of the superconducting gap in the leads will move their filled states up in energy, which lowers the conduction threshold. We observe this behaviour first in the range from 0 to 200 mT in which the left lead becomes normal; the right lead remains superconducting up till about 500 mT. We therefore associate the sub-gap current seen at 250 mT to thermal quasi-particles in this remaining superconducting lead.

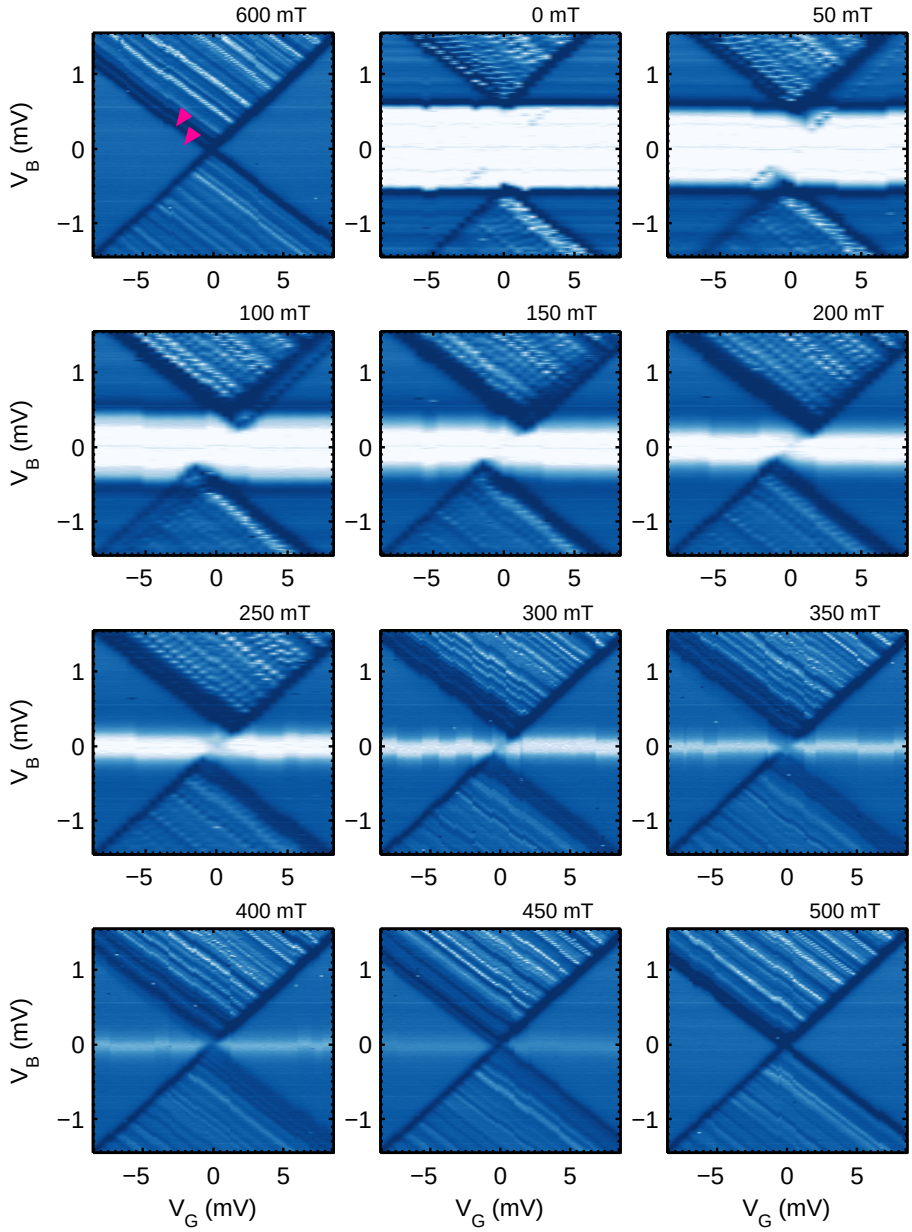

Figure 4.10: Conductance maps at $T \approx 80$ mK of device C at varying magnetic fields which show the transitions from the superconducting state of the device to its normal state. Additionally the pair-current below the Coulomb diamond edges is enhanced until it coincides with the Coulomb diamond edge at 150 mT. The Zeemann splitting of first quantum dot level on the left side of the charge degeneracy point indicates the even charge occupation of the N occupation state. There are no signatures of a Kondo resonance.

4.5.2 Field dependence of CPE cotunneling

The presence of the pair-current line indicates that it is in fact the lead with the higher tunnel coupling whose superconductivity is destroyed first. At this point the pair-current line coincides with the Coulomb diamond edge of the lead in its normal state. This confirms that the sub-threshold feature is resonant when the quantum dot level is aligned with the Fermi-energy of the lead, which is consistent with the picture of pair-currents. A more detailed study of the sub-threshold peak shows an increase in the pair-current with increasing magnetic field until it merges with the Coulomb diamond edge at 200 mT. The same behaviour is observed in device D. We do not yet know how this increases in the pair-current is related to the magnetic field. Possibly it is related to the better thermalization of out-of-equilibrium quasi-particles in superconductors subjected to a small magnetic field as was recently observed by Pascal *et al.* [112].

4.5.3 Revealing the Kondo resonance

Another interesting feature one can expect in quantum dot devices in the intermediate coupling regime is a strong zero-bias conductance inside the Coulomb diamonds that correspond to the odd charge states. This increase in conductance is caused by an elastic cotunneling process that involves the spin-flipping of the electron in the highest occupied level of the quantum dot and is known as the Kondo effect. However in hybrid quantum dot devices the Kondo effect is suppressed by the absence of states in the leads at low energy when the Kondo temperature T_K is lower than the superconducting gap [15]. Since we do not observe a conductance peak at zero bias at either side of the charge degeneracy point we have to conclude that the Kondo temperature of the first excited quantum dot level is lower than the superconducting gap in all samples.

In order to resolve any Kondo features in our devices, the superconductivity in the leads has to be suppressed. However with the application of a magnetic field, spin-degenerate quantum dot level will Zeemann split with an energy given by $E_Z = \pm\frac{g_S}{2}\mu_B B$ (g is the gyromagnetic ratio, μ_B is the Bohr magneton and B is the magnetic field), assuming the quantum dot level has no orbital angular momentum. The zero-bias Kondo resonance will persist in the presence of the magnetic field until the field exceed a critical value of $B_C \simeq \frac{k_B T_K}{\mu_B}$, at which the Kondo resonance splits into 2 symmetric peaks at $eV_B = g_S\mu_B(B - B_C)\Delta S_z$ (where $\Delta S_Z = \pm 1$) which faint rapidly with further increasing magnetic field [150, 15].

A detailed study of the conductance maps shown in figure 4.10 reveals no additional horizontal resonances at either zero and non-zero bias even when a magnetic field is applied. It can therefore be concluded that the high magnetic field necessary to bring

the device to its normal state[5] is larger than the critical field at which the Kondo resonances splits and starts to faint. This gives an upper bound to the Kondo temperature of the studied quantum dot level i.e. $T_K < 400$ mT, which is significantly smaller than the superconducting gap of aluminium ($T_\Delta \approx 3$ K).

4.5.4 Charge parity by Zeeman-splitting

Finally we do observe the Zeeman splitting of the first excited state as is indicated by the magenta coloured arrows in the conductance map at 600 mT. The energy splitting of this level corresponds to the gyromagnetic ratio of about 2, which can be expected. From the observed level splitting we can assign a electron parity to the two Coulomb diamonds around the charge degeneracy point. Since the level splits at the transition from N to N+1 electron on the dot there are two final states available. Hence the N+1 occupation state is a Kramer's doubled, i.e. the N+1 occupation state has an odd number of electrons.

[5]The critical magentic field of thin aluminium films is generally large than the bulk value.

Chapter 5

Non-stationary transport of single-level turnstile

In this chapter we will discuss the generation of quantized current by the turnstile operation of a single quantum dot level coupled to superconducting leads. First we will consider a semi-classical description of the single level turnstile, which we extend to the classical limit of vanishing level spacing. Next, we will include the effect of a finite quantum dot — superconductor hybridization and show how this can result in an adiabatic limitation of the turnstile operation frequency.

Chapter contents

Adding (or removing) a single electron to a weakly coupled island can require substantial electrostatic energy such that its charge states become well defined at low temperature. Current through the island is normally blocked unless at least two charge states are made degenerate (by gate and/or bias) and electrons can pass through in a sequential manner (see figure 5.1a). With the discovery of the single electron charging effect, it was realized that charge quantization provides a way to produce a well controlled current $I = ef$ synchronized to an external driving signal [89] with frequency f. The realization of such a *quantized current source* with normal leads would however require an additional number of weakly coupled islands in series as to block current while crossing the charge degeneracy [44]. An alternative method is to couple the island to leads with a gapped density of states around Fermi-energy[1].

In the foregoing theoretical discussion (section 3.2) on the electron transport through superconducting hybrids SET devices, it was shown that the superconducting gap in the leads suppresses *sequential* electron tunneling at low bias $|V_B| < 2\Delta/e$ at any gate potential, including the charge degeneracy regions. Nevertheless, around charge degeneracy *single electron tunnel events* can still occur between the leads and the island, provided that the electro-chemical potential μ of the island is aligned beyond the superconducting gap of either lead i.e. $\mu > \Delta - eV_B/2$. Driving the island state in a cyclic manner back-and-forth through a charge degeneracy region by manipulation of the gate produces a quantized current related to the driving frequency is generated. The dynamic operation of a superconducting hybrid SET turnstile, in the context of metrological current source was proposed and experimentally verified by Pekola *et al.* [3, 117] using superconducting — normal island (zero level spacing) hybrid devices. In this chapter we extend this principle of operation to a single level turnstile by employing a quantum dot. The quantized current accuracy is considered in terms of missed and erroneous tunnel events. More fundamentally, we study the dynamics of the quantum wave-function of a single occupied level which is tunnel coupled to a semi-continuum.

5.1 The single level turnstile operation

The operation of a single level turnstile is based on the co-operation of two principles i.e. the quantization of the electron charge on a quantum dot and the gapped density of states of superconducting leads[2]. Both principles can be represented schematically, in terms of the quantum dot charges states and the electron tunnel rates to (red) and

[1] Other solutions exists which either require at least two phase shifted driving signals [55, 121] or tunable barriers [81, 10]. A discussion of all different quantized current sources is presented in the introduction of this thesis.

[2] There are other materials with a gapped region in their density of states like e.g. semiconductors. However, as the turnstile performance depends strongly on the sharpness of the gap-edges, superconducting leads are favoured.

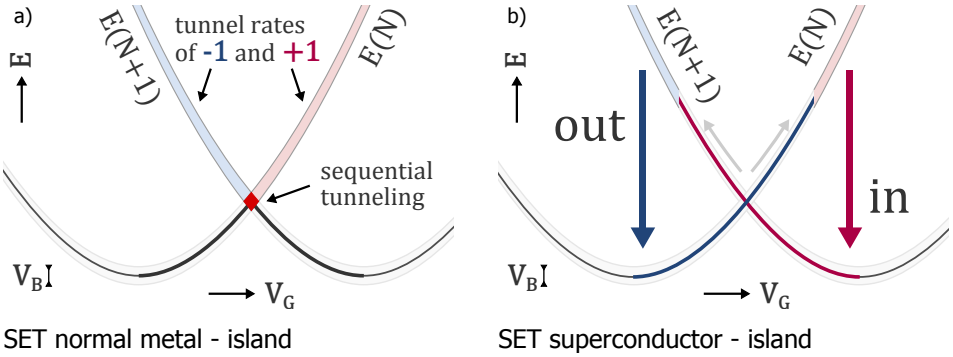

Figure 5.1: Single electron transistor charge states as function of the gate. a) Overlapping tunnel rates for adding (red) and removing (blue) electrons from the center island results in sequential tunneling. b) The gap in superconducting leads suppresses the tunnel rates around charge degeneracy and introduces hysteresis in the charge states which is exploited in electron turnstile devices.

from (blue) the quantum dot, as is shown in figure 5.1b. At sufficiently small bias ($|V_B| < 2\Delta/e$), the gap in the lead density of states nullifies the tunnel rates close to charge degeneracy such that sequential tunneling can not take place[3]. Beyond this region (still at $|V_B| < 2\Delta/e$) only a single electron can be added ('in') or removed ('out') at a time due to charge quantization. The resulting hysteresis in the quantum dot charge states is actively exploited in the turnstile. Driving the quantum dot in a cyclic manner between two charge states will transfer electrons one-by-one, resulting in a quantized current synchronized with the driving signal.

5.1.1 Principle of operation

The turnstile operation is presented schematically in figure 5.2 in which we consider a single quantum dot level positioned at the center of the charge degeneracy region[4] ($\epsilon_d^0 \propto \alpha V_g^0$). In case of a spin-degenerate level, we assume that its double occupation is blocked by the charging energy. A small oscillating gate modulation $A_G\zeta(t)$ with amplitude A_G and frequency f moves the energy level ϵ_d around its static energy position i.e. $\epsilon_d(t) = \epsilon_d^0 + A_d\zeta(t)$ with amplitude $A_d = \alpha A_G$, such that it passes through various states illustrated by the chemical potential diagrams (a-f). During each period it absorbs one electron from the left lead (c) which it ejects into the right lead (f). After the absorption (ejection) of an electron, the now occupied (unoccupied) level passes through the charge degeneracy region (d and a) where sequential tunneling is

[3]When the quantum dot would be coupled to normal leads, the crossing of a charge degeneracy point would always result in a period of allowed sequential tunneling during which many electrons are transported between the leads.

[4]Formally we consider the electro-chemical potential of the occupation of the quantum dot level and not it bare energy. However as there is only a single level present in our system its energy is equal to the electro-chemical potential required to occupy it.

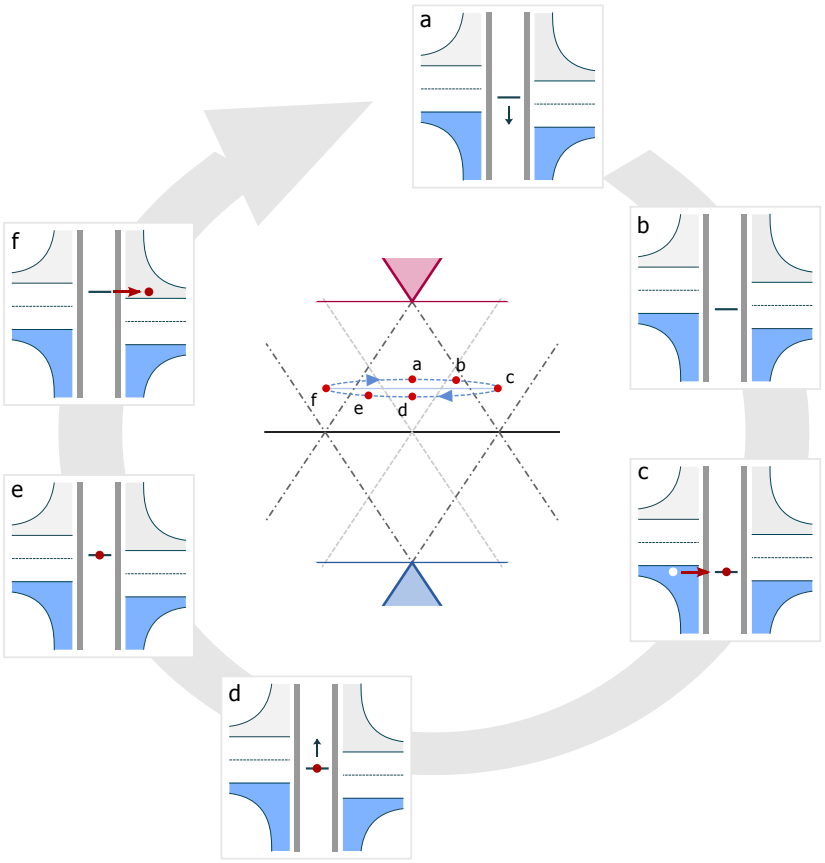

Figure 5.2: A system in which a single level is coupled to two superconducting leads can be used as an single electron turnstile. Driving the level in a cyclic manner through the charge degeneracy region at constant bias generates a quantized current which is equal to ef. The level trajectory corresponds to a horizontal movement in the conductance map of a quantum dot. During each cycle the level passed through various states illustrated by the chemical potential diagrams (a-f).

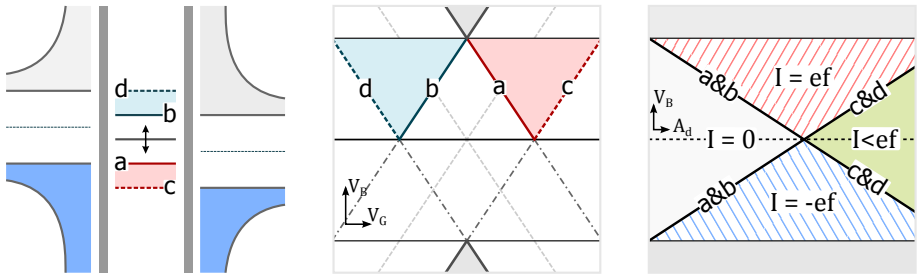

Figure 5.3: A single level electron turnstile can operate in three regimes of signal amplitude which depend on the source-drain bias. At small signal amplitude the level remains between the position a and b such that $I = 0$. The turnstile current will be optimal when $\Delta - V_B/2 < A_g < \Delta + V_B/2$. When the amplitude becomes larger, the turnstile current will deteriorate due to backtunneling events.

blocked by the superconducting density of states and the level maintains its charge. The applied bias determines from (to) which lead the electrons are absorbed (ejected) and hence the direction of the generated current. In the forthcoming discussions we will assume that the static energy level position ϵ_d^0 is tuned at the charge degeneracy point of the single level turnstile.

5.1.2 Static operation rules

From these diagrams one can infer three different regimes of the level modulation amplitude A_δ, which we will explain according to the schematic in figure 5.3. First, when the modulation amplitude is small i.e. $A_\delta < \Delta - V_B/2$, the level will remain inside the superconducting gap of both leads and will not absorb or eject electrons i.e. there is no current. At larger modulation amplitude the level passes both the filled branch edge of the left superconductor (a) and the empty branch edge of the right superconductor (b), which produces a positive current given by $I = ef$, where f is the frequency of the applied modulation signal. This current in *forward* direction will remain independent on the modulation amplitude until the level also passes the filled branch edge of the right superconductor (c) and/or the empty branch edge of the left superconductor (d) i.e. $A_g > \Delta + V_B/2$. In this third regime, referred to as the backtunneling regime, there is a finite chance that the quantum dot will absorb (eject) and electron from the right (left) superconductor. The successive absorption and ejection of an electron from and into the same lead is known as backtunneling. Such an event does not contribute to the turnstile current which consequently will be less than ef. Backtunneling events are therefore considered as a turnstile error.

Another possible process decreasing the turnstile accuracy is the successive absorption and ejections of an electron from the right lead into the left lead. This electrons transport goes in opposite (or *reverse*) direction and contributes negatively to the

turnstile current. In the hypothetical case that the quantum dot level 'jumps' instantaneously between two energies (e.g. assuming the gate is driven by a square wave signal and the setup has infinite bandwidth), respectively just below position c and above position d, one can even expect a negative average current. This can arise due to the inequality in the lead density of states, favouring the absorption from the right lead and the ejection into the left lead.

In the far extent of the backtunneling regime, the energy level excursion will go far beyond the superconducting gap where the density of states in the two leads will be approximately equal. In this limit there is no difference between the tunnel rates to/from either lead and the average current reduces to ≈ 0. The three turnstile amplitude regimes (figure 5.3c) i.e. 1) no current, 2) quantized current $I = ef$ and 3) the errorfull turnstile operation) can be mapped on the conductance map of a quantum dot (figure 5.3b). Electron absorption (ejection) in the forward direction becomes energetically allowed when the instantaneous gate is located to the right (left) of the solid line a (b). Similarly, backtunneling process becomes possibled beyond the lines c and d. Together these four lines construct two triangular areas where the electron absorption and ejections only proceeds from and to the designated leads. When the energy level trajectory is limited between the lines a and b, or exceeds the lines c and d, the turnstile current will be zero or deteriorated by backtunneling processes.

5.2 Errors in the high frequency range

Until now we have considered the turnstile operation from a rather static point of view as we have implicitly assumed that electron tunneling events occur instantaneously once energetically allowed. In reality, quantum tunneling is a stochastic process characterized by an average time between tunnel events given by inverse of the tunnel coupling i.e. $1/\Gamma$. Consequently there is some random delay until an electron enters or leaves the quantum dot. As to construct a more realistic picture one has to take into account the *dwell time* t_d i.e. the finite time between the successive events t_{in} and t_{out} at which the energy level crosses the superconducting gap edge. When the turnstile is operated such that the dwell time in the blue (red) region is much smaller then Γ^{-1}, the ejection (absorption) of electrons may be skipped. Naturally these *missed tunnel events* lead to a turnstile current less then ef.

5.2.1 First order approximation

In order to quantify the probability of these missed tunnel events, one can consider the ejection of an electron into the superconducting lead. The typical decay time of an electron on the quantum dot into the lead is determined up to first order by the tunnel

coupling and the density of states in the leads i.e. $\Gamma_i(\epsilon) = \gamma_i n_i(\epsilon_d)$, where ϵ_d is the position of the quantum dot level with respect to the Fermi-energy of the lead i and $n_i(E)$ is the leads normalized density of states. For an arbitrary trajectory $\epsilon_d(t)$ the probability of the electron to remain in the quantum dot is given by

$$P_{miss} = e^{-\int_{t_{in}}^{t_{out}} \Gamma(\epsilon_d(t))dt}, \tag{5.1}$$

where we integrate the excursion of the quantum dot level over the dwell time during which tunneling is energetically allowed. The total probability of a missed event per cycle is given by $\sim 2P_{miss}$ which accounts for both the missed electron absorption and ejection.

Usually for single electron turnstiles an estimate is obtained by considering a square wave gate signal [71]. Following this course, the probability of missed events in a single level turnstile is simply given by $P_{miss} = \exp(-\gamma n(\epsilon)/(2f))$. However, as the superconducting density of states goes to infinity when $\epsilon \to \Delta$, the probability of missed events vanishes for any driving frequency, which is physically wrong.

In case of a sine wave excursion it is nevertheless possible to obtain a semi-analytical expression by means of a parabolic approximation yielding,

$$P_{miss} = \exp\left[-\frac{\gamma\pi t_d}{\sqrt{A_d^2 - \Delta^2}} \left\{ (A_d + \Delta)\mathrm{E}\left(\frac{A_d - \Delta}{A_d + \Delta}\right) - \Delta\mathrm{F}\left(\frac{A_d - \Delta}{A_d + \Delta}\right) \right\} \right], \tag{5.2}$$

where $\mathrm{F}(m)$ and $\mathrm{E}(m)$ are the full elliptic integrals of respectively the first and second kind and $t_d = (2\pi f)^{-1}\mathrm{acos}(A_d/\Delta)$ is the dwell time. The probability of missed tunnel events, described by expression (5.2), is plotted by grey curves in figure 5.4 as function of modulation frequency (left panel) and amplitude (right panel). The absence of a clear dependence on the modulation amplitude is well understood as a counteracting effect of the decreasing dwell time which neutralizes the singular density of states as $A_d \to \Delta$.

5.2.2 The hybridized quantum dot level

As the solution obtained for the parabolic approximation is based on the Fermi golden rule, it does not take the hybridization of the quantum dot level and the superconducting lead into account. In the discussion of the stationary current through our devices (see section 4.3), we showed the profound effect of the hybridization on the device conductance. This observation justifies the search for a better model as to estimate the probability of missed tunnel events. The typical lifetime of the quantum dot level tunnel coupled to a superconducting lead can be derived by means of the retarded Green function of the quantum dot. In the forthcoming section (5.4) we will show that the

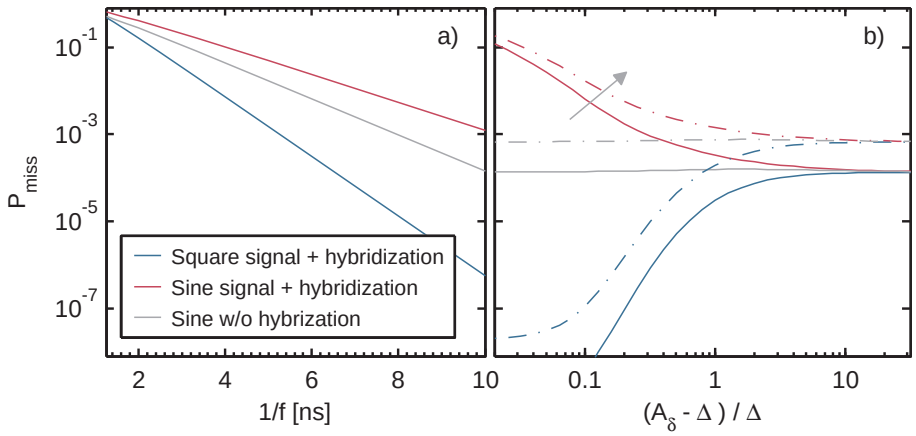

Figure 5.4: Probability of missed tunnel events in a single level turnstile as function of (a) signal frequency (A_δ = 1.1Δ) and (b) amplitude (f = 100, 120 MHz). Calculated rates are obtained with the 1) first order model (grey curves) and 2) the hybridized model (blue and red curves). The arrow in (b) points to increasing frequency. (Δ = 265μeV, γ = 0.03Δ)

energy dependent decay (tunnel) rate of the quantum dot level is given by $\mathrm{Im}(\epsilon_{qp})$, where ϵ_{qp} is the complex pole of the retarded Green's function in eq. 5.4.

As to calculate the probability of missed tunnel events for any arbitrary driving signal, we numerically obtain the complex poles of the retarded Green's function and substitute the corresponding quantum dot level decay rate into eq. 5.1. Figure 5.4 displays P_{miss} obtained for a sine wave (red) and square wave (blue) modulation signal as a function of the frequency (figure 5.4a) and amplitude (figure 5.4a). For both signal shapes there is an exponential increase with frequency visible similar to the result obtained by the first order approximation (grey). Interestingly there is a clear difference in P_{miss} between the two models calculated for sine wave operation, which seems to suggest that hybridization increases the number of missed tunnel events. The square wave signal shows despite this effect, superior results which are particularly pressing in the low frequency regime.

In fact, the difference between the three cases is largest when $A_d \approx \Delta$ (see figure 5.4a) and is easily understood. Due to the 'constant' nature of the square wave, the turnstile can optimally benefit from the increased tunnel rates when ϵ_d is aligned with the superconducting coherence peak. In sine wave operation however, the increasing tunnel rate is counteracted by a decreasing dwell time as $A_d \to \Delta$. In the first-order model (no hybridization) discussed earlier, this resulted in a nearly constant probability as opposed to the result obtained with the numerical model (which takes hybridization into). The effect of decreasing dwell time is in the latter case superior to the increasing tunnel rate as the singularity around $A_d \approx \Delta$ is suppressed by the hybridization between the energy level and the superconducting lead. The probability of missed events consequently increases as $A_d \to \Delta$.

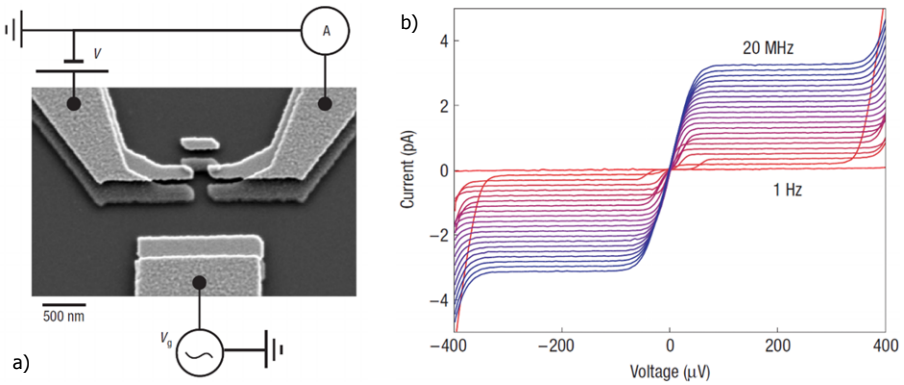

Figure 5.5: a) Scanning electron microscope (SEM) image of a hybrid SET single electron turnstile with a relatively large island (zero level spacing). b) Quantized current at varying modulation frequencies as function of the device bias measured by Pekola *et al.* [117].

With increasing operation amplitude the effect of signal shape and hybridization naturally decreases and the models finally converge at $P_{miss} = \exp(-\gamma\pi t_d)$. In this limit of large amplitude there is effectively no difference between the three models as, during the majority of time, the energy level is located far away from the gap edge, where the tunnel rates are nearly constant and the effect of hybridization is minimal.

5.3 Differences to the S-N-S turnstile

The quantization of charge on the quantum dot, required for the turnstile operation, is in the foregoing discussion intrinsically present as we considered a single non-degenerate quantum dot level. In devices with many electronic levels present on the quantum dot, charge quantization may still be present as the result of a large charging energy i.e. $E_C > k_B T$. In fact the first superconducting hybrid electron turnstile, realized in 2007 by Pekola *et al.* [117] (see figure 5.5), consisted of a relatively large central island ($E_C \approx 2$ K) tunnel coupled to two superconducting leads. Despite the presence of many available levels to (from) which electrons can tunnel, only a single electron can be removed (added), provided that $E_C \approx \Delta$.

Since the addition (subtraction) of a second electron is blocked by the charging energy, the operation of the electron turnstile is somewhat similar to the single level turnstile previously discussed. The introduction of multiple levels however does require an adequate description of their occupation probabilities. In the case of small level spacing, i.e. $\delta \ll k_b T$ and fast electron thermalization, i.e. thermal equilibrium, the level occupation on the island is given by the Fermi-Dirac distribution. The total rate at which electrons tunnel from the superconductor to the island is now simply given by

$$\Gamma_m = \sum_{\epsilon_k} \gamma n_S(\epsilon_k) f_L(\epsilon_k)\big(1 - f_I(\epsilon_k)\big), \tag{5.3}$$

where f_L and f_I are the Fermi-Dirac distributions of respectively the superconducting lead and the island, n_S is the normalized BCS density of states and γ is the tunnel coupling. In the limit of zero level spacing one recovers the electron tunnel rates as given by eq. (3.7) in chapter 3. From here one can easily calculate the probability of missed tunnel events in a many level single electron turnstile, by inserting eq. (5.3) in eq. (5.1). Due to the large number of available states on the island, the effective total tunnel rate for a given γ is much larger compared to the single level turnstile case and ultimately results in a lower probability of missed tunnel events. On the other hand, the electron tunneling is less energy-selective which does bring new challenges.

5.3.1 Thermal errors

Due to thermal fluctuations in the normal island, the sequential tunneling of electrons is possible below $V_B = 2\Delta/e$ and produces an exponentially small current[5] when the SET is tuned close to its charge degeneracy point. In turnstile operation this results in an extra contribution to the quantized current as SET periodically passes through its degeneracy point. Secondly, thermally excited electrons at the island increase the probability of backtunneling events around zero bias. As the relative error induced by sequential tunneling is given by $\simeq \exp(-eV/k_BT_N)$, and the error due to backtunneling is given by $\sim \exp(-(2\Delta - eV)/k_BT_N)$, there is an optimal bias for the turnstile operation given by $|eV_B| = \Delta$ at which both errors are of the order of $\exp(-\Delta/k_BT_N)$. The presence of an optimal source-drain bias defined by thermal arguments is typical to a large island hybrid turnstile. For a single level turnstile one can not define such an optimal operation point. As both error processes are thermally activated, their probability vanishes as the level spacing becomes much larger than the thermal energy i.e. $\delta \gg k_BT$.

5.3.2 Higher order errors

Beyond these classical contributions to the error in the turnstile current one can also expect quantum errors that arise from the elastic and inelastic coherent transfer of electron pairs as is discussed by Averin *et al.* [3]. Again, in the limit of large level spacing and charging energy ($\delta, E_C > \Delta$), the error contribution due to inelastic cotunneling vanishes. Elastic Cooper-pair — electron (CPE) cotunneling remains possible provided that the source-drain bias is larger than Δ as was discussed in section 4.4. But the contribution of this process decays rapidly with decreasing coupling as it is a fourth order process.

In conclusion it can be expected that the main source of error in a single level

[5] In chapter 3 it was shown that this current produces electronic cooling of the island

turnstile (i.e. $\delta > \Delta$) is dominated by the number of missed tunneling events. In order to obtain a rate of missed events comparable to the many-level (or normal island) turnstile, the scarcity of available levels can be compensated by increasing the tunnel coupling. Naturally, (higher-order) CPE cotunneling rate will increase, but do not necessarily limit the turnstile current accuracy. As each n^{th} order CPE cotunneling is characterised by a minimum bias $V_B > \Delta/n$ threshold, the error contribution of these processes can be easily avoided at low (zero) bias. Note that this feature is specific to a single-level hybrid turnstile and would not work in a normal-island hybrid turnstile. Finally it is possible that the (with γ) increasing presence of a Kondo resonance at zero bias puts a lower bias on the operation bias. Determination of the error contribution by these processes is beyond the scope of this thesis but is required as to determine the maximum performance of the single-level hybrid turnstile.

With increasing tunnel coupling also the hybridization between the single level and the superconducting leads increases and should be taken into account. In the next section we will describe the effect of the hybrization, starting from a model that describes the interaction between a single level and the superconducting density of states of a single lead.

5.4 Quantum dynamics originating from hybridization

Usually the tunnel coupling between the leads and a quantum dot is described perturbatively up to first or second order, which is justified when the tunnel coupling is smaller than the typical scale of the variation in the leads DOS. In this limit, the spectral broadening of a single level is the smallest energy scale and therefore the level can be approximated by a discrete state. However, in the case the quantum dot is coupled to a superconductor, this perturbative approach fails (up to any order) when the level is aligned to one of the superconducting coherence peaks (see section 3.5). Fortunately the hybridization between the single level and the superconductor can easily be described by means of Green functions. Without actually deriving any Green function here, we will discuss our results (obtained in collaboration with Denis Basko), to describe the effect of hybridization on the single level turnstile operation.

5.4.1 Spectral properties of the coupled quantum dot

Consider a system composed of a single non-degenerate level, whose bare energy[6] is given by ϵ_d. This level is coupled to a BCS superconductor by a tunnel coupling characterized by γ. The retarded Green function of the level is (in frequency representation)

[6]The bare eigenenergy of the level is the energy it would have if it were completely isolated.

given by

$$\mathcal{G}^R(\epsilon) = \frac{1}{\epsilon - \epsilon_d - \Sigma(\epsilon)}, \tag{5.4}$$

where $\Sigma(\epsilon)$ is called the self-energy of the quantum dot. From the theory of Green functions (see [93, 14]) we know that the retarded Green function contains the local properties of the quantum dot. Discrete eigenstates appear as poles on the real axis while quasi-particle states with a finite lifetime appear as poles in the complex plane, off the real axis. Finally a continuum of states will appear as a branch cut in the complex plane. The self-energy of the quantum dot coupled to a superconductor is proportional to the normal component of the Green's function in the superconductor, i.e.

$$\Sigma(\epsilon) = -\frac{\gamma\epsilon}{\sqrt{\Delta^2 - \epsilon^2}} \approx -\gamma\sqrt{\frac{\Delta/2}{\Delta - \epsilon}}. \tag{5.5}$$

Using this approximation which is valid when $\epsilon \simeq \Delta$, the poles of the retarded Green function[7] are determined by

$$\Lambda + \left(\epsilon_d - \Delta\right) \simeq \sqrt{\frac{\gamma^2\Delta/2}{\Lambda}}. \tag{5.6}$$

As a function of the bare level energy ϵ_d, we can distinguish two different regimes. For $\epsilon_d - \Delta < -\left(\gamma^2\Delta/4\right)^{1/3}$, eq. (5.6) has a single real and positive solution which indicates the existence a single discrete state $|A\rangle$ of infinite lifetime. In the opposite case, the retarded Green function has a second imaginary solution which corresponds to a resonance in the continuum at

$$\epsilon_{qp} \approx \epsilon_d - i\sqrt{\frac{\gamma^2\Delta}{2\left(\epsilon_d - \Delta\right)}}. \tag{5.7}$$

The characteristic lifetime of this quasi-particle state $|qp\rangle$ is given by the imaginary part of its energy i.e $\hbar/\mathrm{Im}\left(\epsilon_{qp}\right)$. In fact, we have already encountered this state, as it is responsible for the stationary electron transport at $|V_B| > 2\Delta/e$ described in section 3.5. Its spectral density (shown in figure 3.12b) is continuous and given by $\rho(\omega) = -(1/\pi)\mathrm{Im}\mathcal{G}^R(\omega)$.

The somehow unexpected result here is that the discrete state $|A\rangle$ described by the real pole of the retarded Green function survives beyond $\epsilon_d = \Delta$. For $\epsilon_d \gtrsim \Delta$ the energy of this state, which is bound below the superconducting gap edge, is given by

$$\epsilon_A - \Delta \approx -\frac{\Delta}{2}\frac{\gamma^2}{\left(\epsilon_d - \Delta\right)^2}. \tag{5.8}$$

We plot ϵ_A in figure 5.6a as function of the bare level energy ϵ_d for various coupling

[7] Besides the isolates poles that indicate the discrete and quasi-particle state, the Green function also has a branch cut at $\epsilon = \Delta - i\eta$, where η goes from 0 to ∞

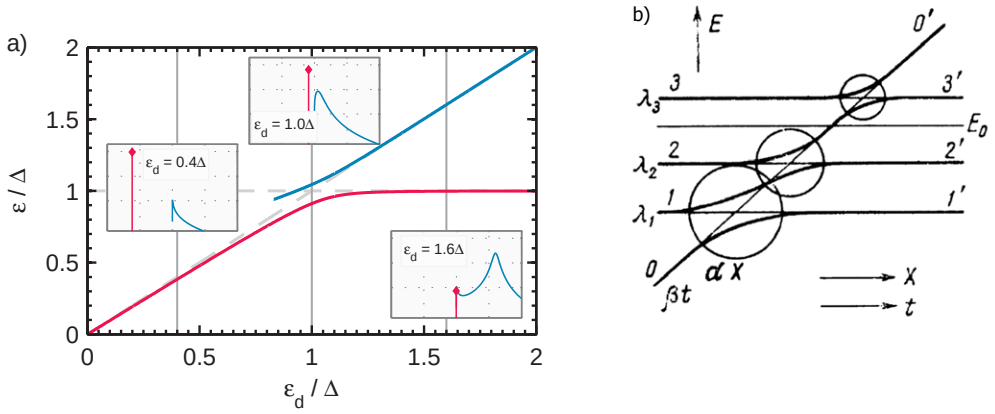

Figure 5.6: a) Spectral properties single level coupled to a superconductor ($\gamma = 0.04\Delta$, $\Delta = 265\,\mu$eV). For $\epsilon_B < \Delta$ there only exists one discrete solution $|A\rangle$ (magenta), while above $\epsilon_d \approx \Delta$ there exists a second quasi-particle state $|qp\rangle$ (blue) with $\epsilon_{qp} \approx \epsilon_d$. Insets display the spectral density and weight of the states at $\epsilon_d/\Delta = 0.4, 1.0, 1.6$, as function of ϵ on a log scale. b) Avoided crossings of a single discrete level with multiple close lying discrete states used by Demkov and Osherov [26] to explain the avoided crossing of a single discrete with a semi-continuum density of states ($\delta \to 0$).

strengths. In the same plot we show the energy of the quasi-particle state $|qp\rangle$ which exists only for $\epsilon_d - \Delta < -\left(\gamma^2\Delta/4\right)^{1/3}$. At $\epsilon_d = \Delta$, there is a visible anti-crossing between the two states which increases with increasing coupling (γ) between the single level and the superconductor.

5.4.2 Dynamics of the quantum dot wave function

The avoided crossing of ϵ_d and the gap edge is, to some extent, very similar to the Landau-Zener physics of a two-level system driven across degeneracy. We can obtain a more illustrative picture by regarding the consecutive crossing of a discrete level with various close-lying discrete levels (figure 5.6b). At each avoided crossing (encircled) there is a finite probability that the electron will make a transition to the excited state.

This approach has been used by Demkov and Osherov [26] to describe the transition probability between a discrete state and a semi-continuum i.e. in the limit of zero level spacing between the levels. They find that the transition probability from the discrete state to the continuum can be decomposed into elementary Landau-Zener factors. In the case of a featureless density of states above the gap edge, the spectral weight of the lowest discrete state decays exponentially as the bare level energy enters the semi-continuum. This is significantly different from the result that we find for superconducting leads, where the spectral weight of $|A\rangle$ is given by a power law,

$$Z = \left(1 - \frac{\partial\Sigma}{\partial\epsilon}\right)^{-1} \approx \frac{\gamma^2\Delta}{\left(\epsilon_d - \Delta\right)^3}. \tag{5.9}$$

Moreover we find that the level repulsion experienced by $|A\rangle$ at the gap edge is particularly amplified by the density of states divergence. Without the divergence, ϵ_A would exponentially tend to Δ, which significantly decreases the anti-crossing energy.

5.4.3 Time dependence

Next we assume ϵ_d is well below the superconducting gap and the discrete state is occupied while the quasi-particle state remains empty. When the bare level energy is moved adiabatically (by the gate) beyond the superconducting gap Δ and back, the electron will remain in the (ground) state $|A\rangle$, below the continuum, from where it can not be ejected into the superconductor. In the picture of the single electron turnstile operation, adiabatic transitions will thus result in missed tunneling events in the low signal frequency regime, where classically one would not expect it. The rate of these missed events is directly proportional to the probability of an adiabatic transition.

For an arbitrary time dependence $\epsilon_d(t)$, one can obtain this probability by calculating occupation probability of the discrete state $|A\rangle$ at the end of the bare level excursion when $\epsilon_d = 0$. Since $|A\rangle$ corresponds to the bare level when $\epsilon_d \ll \Delta$, its occupation probability is given by the electron wave function amplitude $\chi(t)$ of the bare energy level at $t \to \infty$, which is can be obtained by the following integro-differential equation

$$i\frac{d\chi(t)}{dt} = \epsilon_d(t)\chi(t) + \int_{-\infty}^{t} \Sigma^R\big(t-t'\big)\chi(t')dt'. \tag{5.10}$$

Here $\Sigma^R(t)$ is the inverse Fourier transform of the self energy given in eq. (5.5). Analytical solutions to this equation can be found for three particular signal shapes $\epsilon_d(t)$. Most extreme is the quantum quench model in which the level position is changed instantly. Consequently the transitions are always of a non-adiabatic nature as opposed to the two other solutions i.e. the linear and quadratic time dependence.

Turnstile dynamic operation diagram

Derivation of the solution to the quadratic time dependence, defined as $\epsilon_d - \Delta = (A_\delta - \Delta)\left(1 - 4t^2/t_d^2\right)$ is complex and goes beyond the scope of this thesis, but produces a good understanding of the turnstile operation in terms of two dimensionless parameters $x = (A_d - \Delta)^3/(\gamma^2\Delta)$ and $y = 4(A_d - \Delta)/(t_d^2\gamma^2\Delta)$. In the diagram shown in figure 5.7, four different areas are distinguished. The magenta shaded region at low signal frequency denotes an adiabatic area. Directly above and separated by the line $y = 1/x$ lies the semi-classical region in which the missed event probability is given by $P_{miss} = \exp\left(-\int \Gamma(\epsilon_d(t))dt\right)$. At even high signal frequencies ($y > \max(1, x)$) we find the third region where the bare level excursion goes to fast for complete decay such that the coupling to the leads acts as a small perturbation but does not lead to tunnel

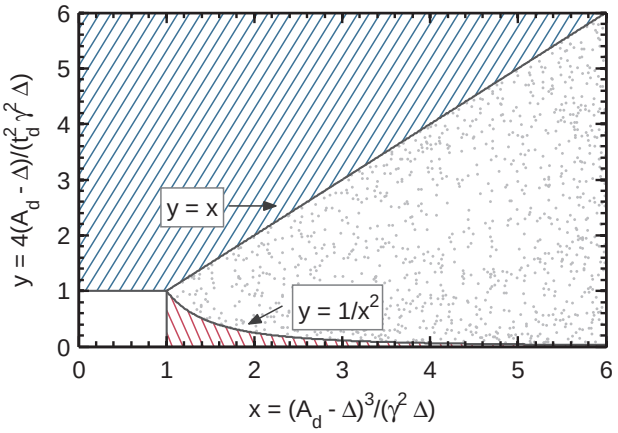

Figure 5.7: 'Phase' diagram of the single-level electron turnstile operated by a sine wave signal (approximated by a square wave trajectory) expressed as a function of two dimensionless parameters i.e. the horizontal and vertical axes are related to respectively operation amplitude and frequency. The red hatched area denotes the adiabatic operation regime; blue hatched the 'perturbative' and grey dotted the 'semi-classical' regime. The turnstile operation can not be analysed analytically within the white rectangle.

events. In the fourth region of small signal frequency ($y < 1$) and amplitude ($x < 1$), no solution could be found.

The quantum quench model

In the quantum quench model, the bare level energy is abruptly changed from some value deep in the superconducting gap at $t = 0^-$ to ϵ_d at $t = 0^+$. In this case the solution to eq. (5.10) is directly given by the retarded Green's function of the level leading to,

$$\chi(t > 0) = i\mathcal{G}^R(t) = -\int_{\infty}^{\infty} \frac{d\epsilon}{2\pi i} \frac{e^{-i\epsilon t}}{\epsilon + i0^+ - \epsilon_A - \Sigma\big(\epsilon + i0^+\big)\big)}, \tag{5.11}$$

whose integral can be obtained by the evaluation of the complex residues at the poles.

The quantum quench model is obviously a big oversimplification of the experimentally obtainable bare level excursion and one should consider whether it can be used at all. The applicability of the model is determined by the rise time of the applied signal which should be smaller than the typical time scale in the model t_{QQ} which is given by

$$t_{QQ} = 1/\max\Big(\epsilon_A - \Delta, \big(\gamma^2\Delta\big)^{1/3}\Big). \tag{5.12}$$

When we use the coupling parameter of devices C and D that we have obtained in the previous chapter, we conclude that $t_{QQ} > (10\,\mathrm{GHz})^{-1}$. Consequently the quantum quench model can not be applied when we assume an experimentally obtainable rise time of 0.8 - 1.6 ns.

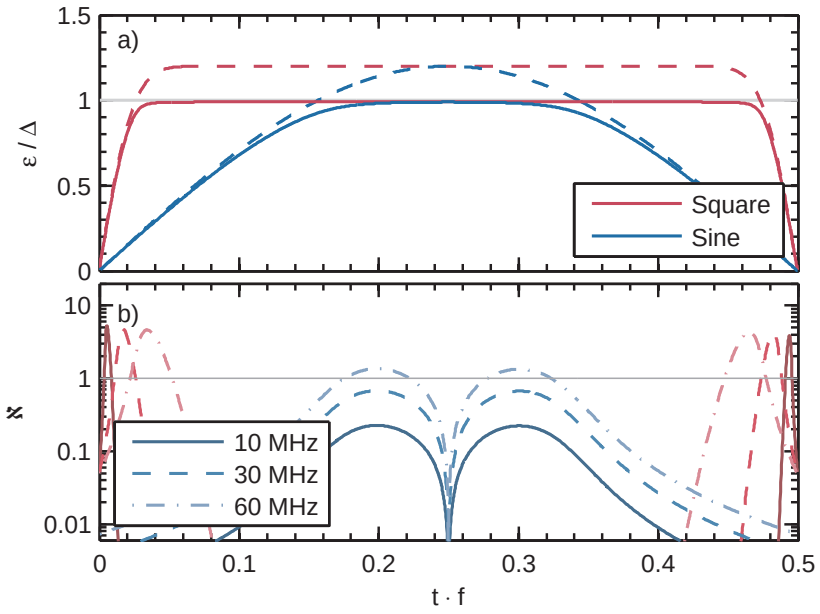

Figure 5.8: a) Numerically calculated discrete level (solid curve) trajectories $\epsilon_A(t)$ produced by a sine (blue) and square (red) wave modulated bare level (dashed curve). Rise time of the square wave is 1.6 ns. b) Numerical evaluation of the adiabaticity parameter $\aleph$ during the bare level modulations in (b), calculated at three different modulation frequencies (f = 10, 30, 60 MHz). When $\aleph < 1$ during the discrete level excursion, the system remains adiabatic which results in a missed tunnel event. With $\gamma = 0.03\Delta$ and $\Delta = 265\,\mu$eV, the transition from adiabatic to non-adiabatic takes place at $f \approx 20$ MHz.

5.4.4 Adiabatic transition at the gap edge

Although we are unable (at least up to the point of this writing) to derive or compute the exact probability of missed events for an experimentally realistic, bare level excursion $\epsilon_d(t)$, we can numerically evaluate the condition for adiabatic transitions which is, just like the case of a Landau-Zener 2-level system, given by

$$\frac{d\epsilon}{dt} \ll \epsilon^2/\hbar, \tag{5.13}$$

in which ϵ is the energy separation between two anti-crossing eigenstates. For the case under consideration, i.e. a single discrete level and a BCS continuum, the adiabaticity condition takes the following form

$$\aleph = \frac{1}{\omega^2}\frac{d\omega}{dt} \ll 1, \tag{5.14}$$

in which $\omega = \hbar\big(\epsilon_A - \Delta\big)$ and $t_{in} - t_{out}$ defines the dwell time of the bare level energy above the superconducting gap. The somewhat different energy parameter in this equation is a consequence of the continuous density of states in the superconductor. The turnstile operation will only be adiabatic when the inequality of eq. (5.14) holds throughout the complete period for which $\epsilon_A > \Delta$.

For any arbitrary bare level excursion $\epsilon_d(t)$, one can determine the instantaneous discrete state energy ϵ_A as a function of time, by solving eq. (5.6) numerically. Figure 5.8a shows ϵ_A (solid line) and ϵ_d (dashed line) as function of time for two different driving signals. The square wave signal has a constant rise time (typically 1.6 ns in our experiments). For each point in time the adiabaticity parameter $\aleph$ (hebrew *aleph*) can be evaluated and is shown in figure 5.8b, for three different driving frequencies. It is visible that the square wave driving signal always breaches the adiabaticity condition, since its rise time is constant. The behaviour of the sine wave driving is however frequency dependent and below a certain frequency the system remains adiabatic during the full excursion of the bare level. This is the main result of this chapter. It dictates that one can expect adiabatic suppression of the single level turnstile current at low frequencies, which was rather unexpected.

Up to now we have only considered the coupling to one the two junctions in the single electron turnstile. The continuation to two leads is rather straightforward since the source-drain bias can be regarded as an effective decrease of the superconducting gap i.e. $\Delta' = \Delta - eV_B/2$. This allows us to determine the 'adiabaticity degree' of the system as a function of both the applied bias and signal amplitude. In figure 5.9 we plot contour maps of maximum $\log_{10}(\aleph)$, reached during the bare level excursion produced by a sine wave modulation signal. Each contour plot represent a different combination of the driving frequency (columns) and coupling strength γ (rows). In the case of low

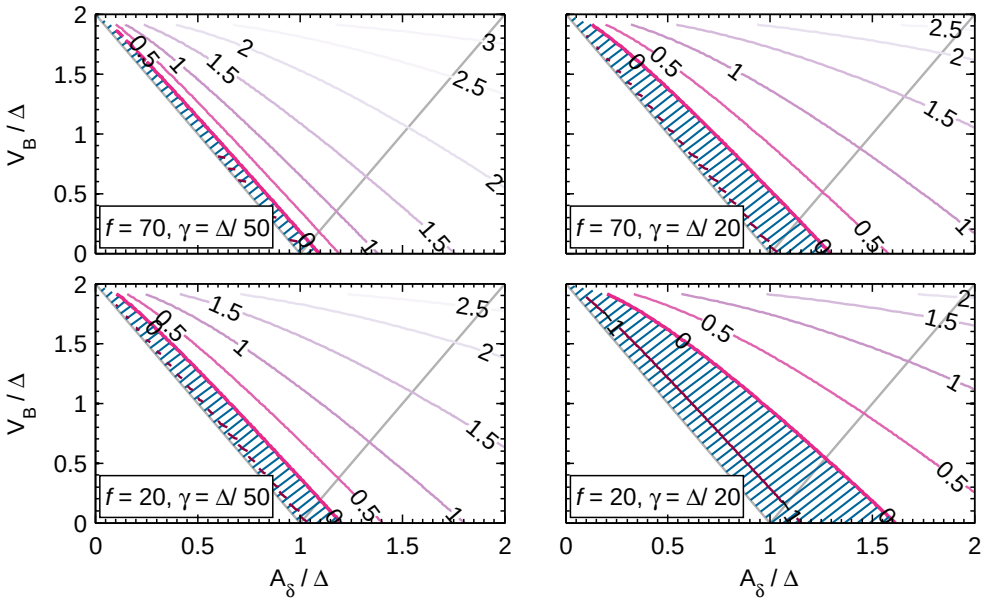

Figure 5.9: Contour maps of $\log_{10}(\max[\aleph])$ as function of the sine wave modulation amplitude and source-drain bias. The turnstile current is adiabatically suppressed in the area left of the zero contour line, while energetically allowed in the area right of the grey line. A decrease in signal frequency or an increase in the tunnel coupling (γ) 'rotates' the zero contour line to the top left, thereby increasing the hatched area in which adiabatic current suppression dominates the turnstile operation.

coupling and high frequency (presented in figure 5.9a) the $\aleph = 1$ contour appears as a near straight line, lying closely to the classical turnstile condition. The close proximity between the conditions reveals that the system behaves rather classically in this regime. With increasing coupling (figure 5.9b) or decreasing signal frequency (figure 5.9c), we observe that the $\aleph = 1$ contour 'turns' away from the classical turnstile condition. This results in an area (blue shaded) where the turnstile operation is energetically allowed but suppressed by adiabatic transitions.

Chapter 6

Single-level turnstile experiments

In this chapter we present measurements of a quantum metrological current generated by the periodic modulating of a single quantum electronic level coupled to two superconducting leads. We demonstrate current quantization up to 200 MHz, conveyed by a single quantum level. Strong experimental evidence of the single level nature of our turnstile device is provided by a sharp onset of backtunneling processes and the temperature-robust operation beyond 300 mK. Finally show a systematic current suppression uniquely observed in low frequency sine wave operation, which can be attributed to the adiabatic suppression of tunnel events.

Chapter contents

Until now the study of quantum dot - superconducting hybrids has mainly been focussed on the electrical features of strongly coupled hybrids under stationary conditions such as Andreev bound states [135, 118, 72], supercurrent reversal [146] and the interplay with the Kondo effect[16, 15, 150]. These studies are largely driven by the search towards quantum computing which requires the measurement of coherent quantum states. Driven by another perspective i.e. quantum-metrology, the quantized transport of single electrons has been studied by either the dynamical modulation of tunnel barriers in electrons pumps [81, 10] or the electro-chemical potential in superconducting single electron turnstile [117]. Here we show the first realization of a single level turnstile in which we manipulate the electro-chemical potential of a quantum dot contacted by superconducting leads to generate a quantized current. We explore and characterize the turnstile operation parameters. Moreover we show that the turnstile experiment is possibly an experimental realization of the single level versus semi-continuum Landau-Zener transition which was introduced in the last chapter.

6.1 Frequency response

Our quantum dot - superconductors hybrid devices are obtained by the electromigration of aluminium nano-junctions at T = 4K, preceded by the deposition of 4 nm diameter gold nano-particles. With this technique, we obtained 8 devices in which a small particle is weakly coupled to the superconducting leads. The DC electronic transport measurements $T \approx 80$ mK, as discussed in chapter 4 confirm the quantum dot behaviour of the particles. We now continue with the application of a time-dependent signal to the AC gate electrode which is capacitively coupled to the DC gate electrodes by a large on-chip parallel plate capacitor (see chapter 1). As discussed in the previous chapter, the back-and-forth modulation of the electro-chemical potential through the charge degeneracy region at a constant bias $|V_B| < 2\Delta/e$ should give rise to a quantized current equal to $I = ef$, where f is the frequency of the applied modulation signal. Here we study the turnstile current response to either a sine or square wave shaped time dependent signal. The rise-time t_{RT} of the square wave is set to 1.6 ns, such that the higher harmonics ($1/t_{RT} \approx 0.63$ GHz) remains well below the superconducting gap (~ 64 GHz) as to suppress photon-assisted quasi-particle excitations.

To roughly characterize the operation regime of our turnstile devices, we measure the turnstile current at constant bias $V_B = \Delta/e$ as function of the modulation signal frequency. Hereto we first accurately position the DC gate V_G^{DC} at the center of the charge degeneracy region. Note that this position, referred to as the gate offset position V_G^0, lies in between the two apexes of conductive regions at positive and negative bias (see section 4.2). As we do not precisely know the transmission of the AC wiring, including the on-chip capacitive coupling between the static gate and the AC electrode,

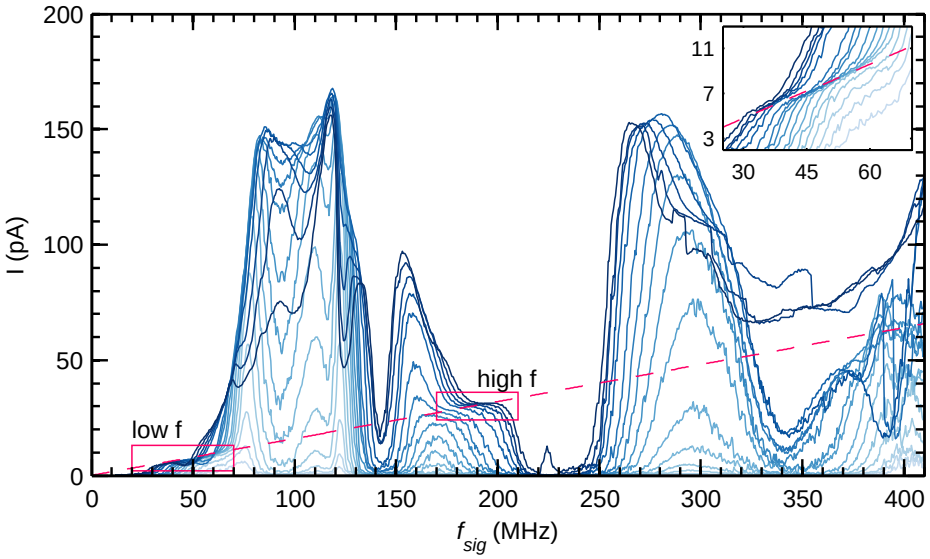

Figure 6.1: DC turnstile current (device D) as function the sine wave modulation frequency measured at varying modulation amplitude (increasing from bright to dark). The dashed magenta line gives the theoretical turnstile current $I = ef$. (T = 90 mK, $eV_B = 3/2\Delta, A_{sig}$ = −18 to − 2 dBm)

we measure frequency sweeps at various constant signal amplitudes. In figure 6.1 we plot the measured current response of device D for increasing signal amplitude (light blue to dark blue) of a sine wave modulation signal.

We observe frequency regions of high and low current as compared to the theoretical turnstile current which is indicated by the dashed magenta line. The current in these regions is possibly affected by the presence of parasitic resonances and regions of signal suppression in the AC electrode circuit. In two frequency regions (low: 20-70 and high: 180-205 MHz) however, we observe a partial correspondence between the theoretical turnstile current and the measured current response at different driving amplitudes (illustrated by the inset). In these two regions, we have an optimal coupling between the AC driving electrode and the electro-chemical potential of the quantum dot. This limited range of operation seems disappointing, but is considering our little experience in producing on-chip bias-tee elements a reasonable result. The previous conclusion that the coupling outside the two frequency regimes is affected by external resonances and alike, is supported by measurements on a second device (device C) which shows a similar behaviour in frequency. To construct an unambiguous picture of our single level turnstile device, we will characterize its operation in terms of various parameters in the next sections.

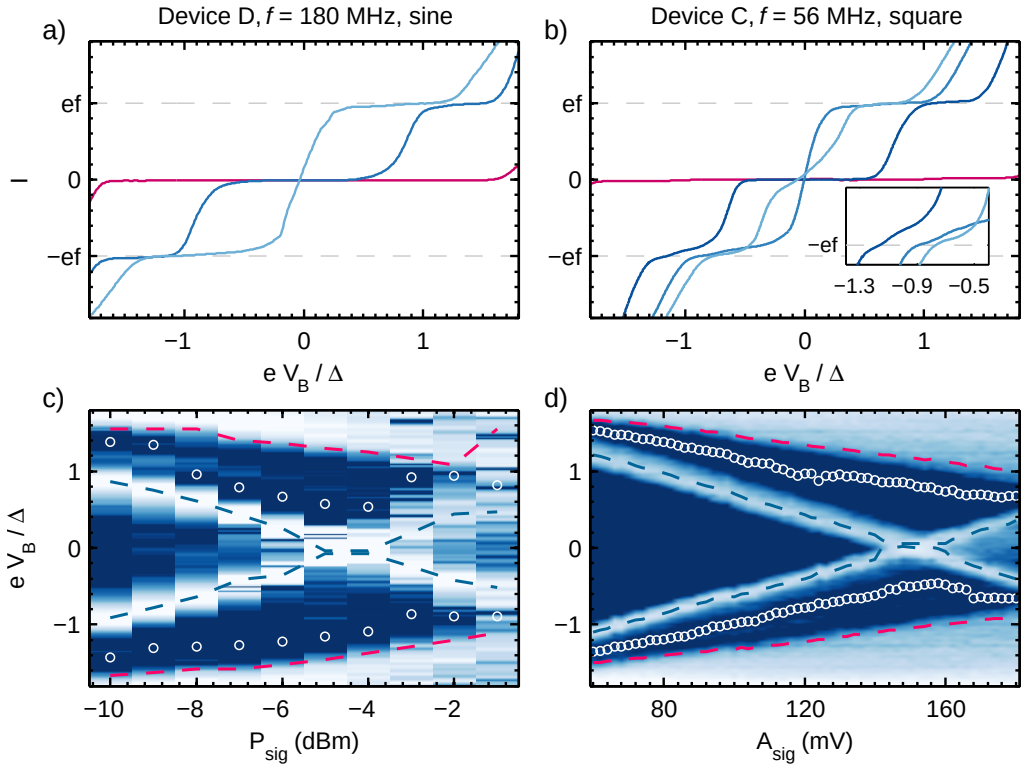

Figure 6.2: a, b) Example traces of the turnstile current as function of the bias measured in device D (a) and C (b) at several modulation amplitudes of respectively a sine (180 MHz) and square (56 MHz) wave. c, d) Differential conductance maps compiled from the bias traces exemplified by respectively (a) and (b). Blue dashed lines denote the current onset at V_B^{on}, white circles denote the point V_B^{opt} of minimum differential conductance at the current plateau and the magenta dashed lines give the error onset at V_B^{err}.

6.2 The semi-classical description

Our first step in the verification of the turnstile operation is the characterization of the current as a function of the bias potential and the modulation amplitude. Again we first accurately position the gate at V_G^0. Next we record the current while the bias is slowly varied between $\pm 2\Delta/e$ and a continuous modulation signal of constant frequency and amplitude is applied to the gate. Measurements at each frequency are repeated for various signal amplitudes. With increasing amplitude we observe the development of a clear plateau in the sub-gap current located at $I = \pm ef$ (figure 6.2a and 6.2b). The $I(V_B)$ trace measured under stationary conditions is shown as a reference by the magenta curve. Color maps of the numerically obtained differential conductance dI/dV_B at each signal amplitude A_{sig} show the transition between zero current and $I = \pm ef$ as bright lines that cross at zero bias (figure 6.2c and 6.2d). We numerically extract the plateau onset bias $\pm V_B^{on}(A_{sig})$ which is defined by the maximum differential conductance at the transition (indicated by the dashed blue lines). The extracted bias

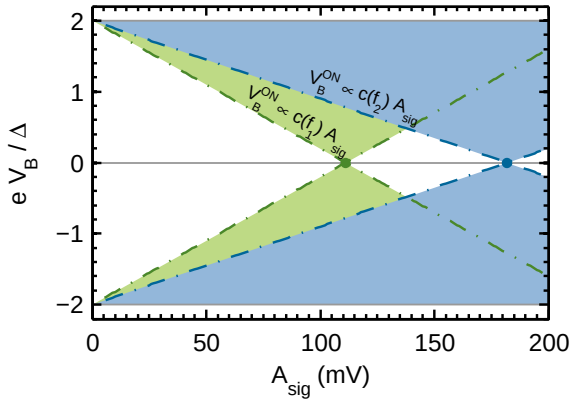

Figure 6.3: Theoretical turnstile current diagram as a function of signal amplitude and bias for two different operation frequencies. Dashed lines corresponding to the current onset, construct regions of quantized current (hatched areas). The slopes of the current onset is affected by the frequency dependent signal transmission $c(f)$.

points show a clear linear dependence on the driving amplitude[1]. A careful analysis of constructed lines at several frequencies of the modulation signal (sine or square waves) shows the consistent crossing of all lines through the point ($V_B = \pm 2\Delta/e$, $A_{sig} = 0$).

Verification of turnstile operation

The observed properties of the plateau in the sub-gap current meet three important criteria for the unambiguous identification as a turnstile current plateau i.e. 1) the two lines $\pm V_B^{on}(A_{sig})$ are linearly dependent on the signal amplitude and cross at zero bias, moreover 2) the lines constructed at each driving frequency all cross the point ($V_B = \pm 2\Delta/e$, $A_{sig} = 0$)[2] and finally 3) the current value on the plateau is exclusively determined by the signal frequency[3].

The crossing of the two transition lines at zero bias is both an important and practical observation. As discussed in the previous chapter, such a crossing is expected when 1) the turnstile current onset is unaffected by adiabatic suppression (section 5.4) *and* 2) the modulation amplitude of the electro-chemical potential is equal to the superconducting gap, i.e. $A_\delta = \Delta$ (section 5.1.2). Based on this observation we can calculate the frequency dependent signal transmission i.e. $A_\delta = c(f)A_{sig}$ and renormalise the signal amplitude. When the crossing at zero bias is not visible in a differential conductance map, the transmission can still be obtained but one has the assume that the turnstile operation is non-adiabatic at low A_{sig} such that the current onset is given by eq. (6.1).

[1] Signal generators often require the sine wave amplitude to be set in units of the signal power (dBm) instead of the potential (volt). One can simply convert one to the other by $[mV] \propto \sqrt{10^{0.1[\mathrm{dBm}]-3}}$.

[2] This was be verified by extrapolating $\pm V_B^{on}(A_{sig})$ to zero modulation amplitude.

[3] This is for example fundamentally different from photon assisted tunneling between two superconducting electrodes in which the current onset is frequency dependent while the current value of the subgap plateaux is frequency independent[136].

A (linear) fit of $V_B^{on}(A_{sig})$ in the low A_{sig} regime directly gives the signal transmission.

$$eV_B^{on} = 2\Delta - 2A_\delta \tag{6.1}$$

Parasitic effects

Besides the bright lines that indicate the plateau onset, we observe bright regions with a bias threshold $\pm V_B^{err}(A_{sig}) < \pm 2\Delta/e$ (magenta dashed lines in figures 6.2c and 6.2d) which decreases with increasing signal amplitude. In these regions ($|V_B| > V_B^{err}(A_{sig})$) the current becomes larger than $|I| = ef$ which is most likely due to crosstalk between the gate and bias electrode. A further characterization of this side effect will be presented in section 6.3. For now we consider the onset of these regions as the upper limit of the turnstile bias operation range.

Together the four lines ($\pm V_B^{err}$ and $\pm V_B^{on}$) delimit 3 characteristic current regions i.e. 1) a region of zero current, 2) two regions where $I \approx \pm ef$ and 3) a region where $|I| < ef$. The observation of a suppression of turnstile current in the third region is consistent with the concept of backtunneling as was discussed in the previous chapter. We will study this feature in more detail in section 6.6 as it is a strong indication of the single level nature of our turnstile device.

At some frequencies we observe yet another line in the $dI/dV_B(V_B, A_{sig})$ map which is located between the plateau and error onset lines at either one of the bias polarity (insets figures 6.2a and 6.2d). A closer inspection of the $I(V_B)$ traces shows that the line corresponds with a second small current step at the plateau (see inset figure 6.2b). In fact, it is only after this step that the current becomes equal to $\sim ef$. In sample C and D, the substructure is located at opposite polarity. The origin of these lines is so far not fully understood but a detailed study does exclude the asymmetry in the tunnel and capacitive coupling.

Gate dependency

The consistency of the turnstile operation can be further established by the study of the turnstile current as a function of the center gate value. Hereto we first apply a static bias $< 2\Delta/e$ to the device. Next we record the current while the static gate is slowly moved from below to above V_G^0. During each gate trace, a continuous modulation signal of constant frequency and amplitude is applied to the gate. We repeat the measurement for several combinations of the modulation amplitude and frequency. In figure 6.4a, five example traces are plotted for increasing (dark to bright) signal amplitude (f = 185 MHz, $V_B = 3/2\Delta$), which demonstrate the development of a flat current plateau at $I = ef$. Notice that the current accuracy on the plateau of the first 4 traces is strikingly independent of the gate voltage. Only at the edges of the

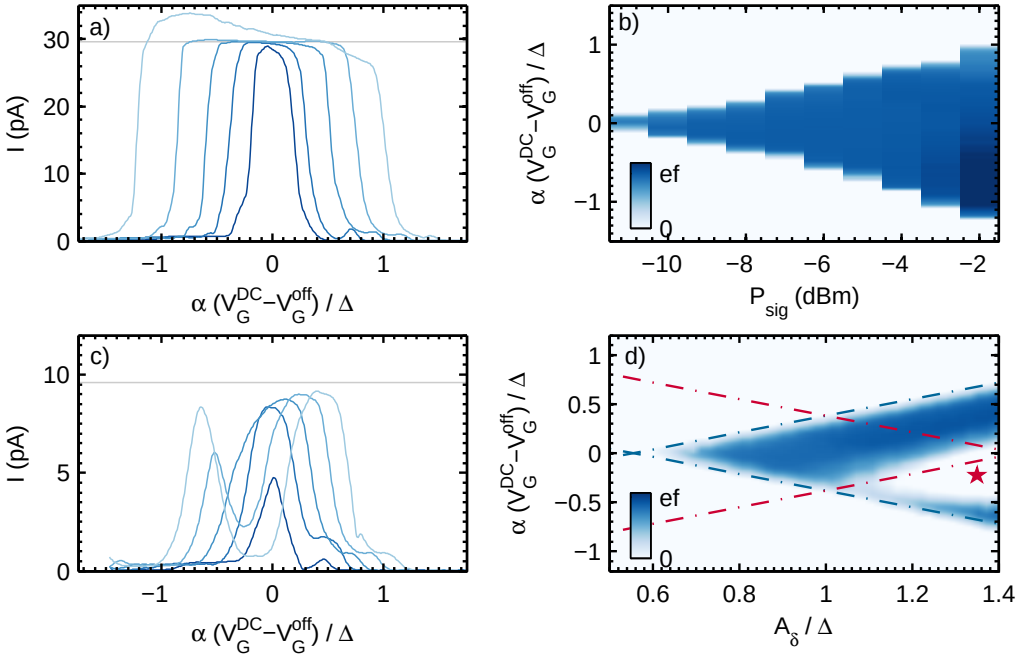

Figure 6.4: a) Example traces of the current as function of the center gate position measured with several modulation amplitudes P_{sig} = −10, −8, −6, −4, −2 dBm. b) Turnstile current map constructed from several center gate traces measured with varying modulation amplitude. (V_B = 3/2Δ, sine wave, device D) c, d) Similar measurements at V_B = Δ. (square wave, device D)

plateau there is some small curvature which is slightly different between the left and right side. A colour map (6.4b) of the current $I(V_B, V_G^{DC})$, demonstrates the plateau widening with increasing modulation amplitude. Below P_{sig} = −10 dBm the modulation amplitude of the quantum dot level is for any gate position, too small to cross both the filled branch of one superconductor and the empty branch of the other. With increasing amplitude, a current plateau is developed centred around V_G^0. When the modulation amplitude of the quantum dot level[4] increases beyond Δ we start to see the suppression of the turnstile current due to backtunneling at the edge of the plateau. On the right side of the P_{sig} = −2 dBm trace in figure 6.4a we observe a clear deficit in the current. The excess of current at the left edge of the plateau can be well understood by an angled level excursion in the (V_B, V_G) plane, caused by a non-negligible gate-bias crosstalk. Since the traces shown in figure 6.4 are obtained at a static bias close to the gap edge V_B = 3/2Δ, already a small vertical component can be enough to send the level beyond the Coulomb threshold where sequential tunneling is allowed. The result is an unknown current contribution which depends strongly on the exact excursion.

Similar measurements of the turnstile plateau obtained at a smaller static bias i.e. V_B = Δ show a remarkably different picture as is shown in figure 6.4d. Again we observe

[4]In the regime where the modulation amplitude of the quantum dot level A_Δ is below δ, its values can be read of directly from the edge locations of the plateau

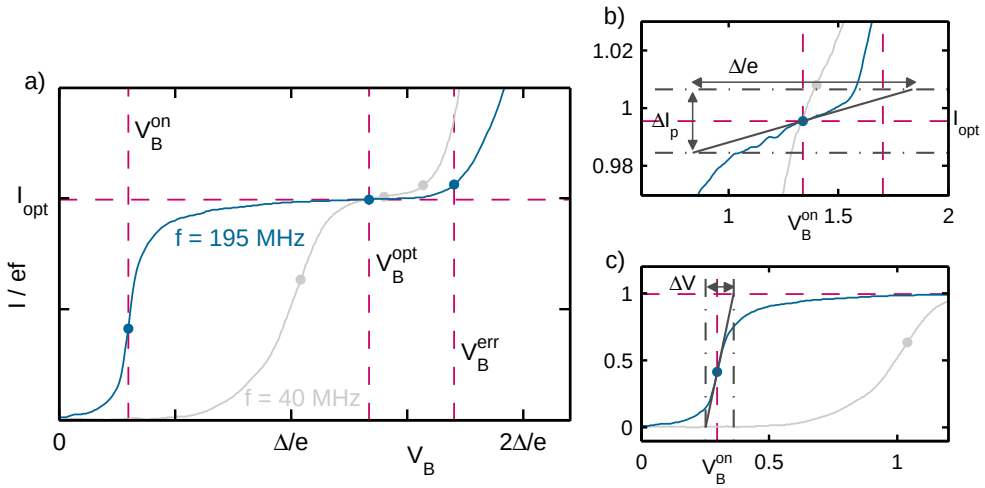

Figure 6.5: The turnstile operation as function of bias (sine wave, $f = 195$ MHz and 40 MHz) is characterized in terms of current onset, optimal bias and error bias. The current plateau is characterized by the current variation ΔI_p and the onset width ΔV.

typical triangular shape with the apex located at V_G^0. However at high modulation amplitudes another slightly asymmetric triangular region (denoted by star) appears in which current is strongly suppressed. We can attribute the current suppression to backtunneling which appears asymmetric around V_G^0 due to the asymmetric tunnel coupling to the leads.

6.2.1 Current accuracy and plateau characterization

The foregoing characterization the turnstile plateau shape as a function of bias/gate potential and modulation signal amplitude, showed that the generated current is indeed consistent with a quantized turnstile current. Next we will shift our focus to current traces and characterize the turnstile plateau in terms of three parameters (indicated in figure 6.5), i.e. the current accuracy ($\tilde{I}_{opt} - 1$, where $\tilde{I} = I/ef$) and plateau flatness (ΔI_p) at optimal bias (V_B^{opt}) and the rise voltage (ΔV) at the onset.

Turnstile current accuracy

In order to characterise the turnstile accuracy we evaluate the current I_{opt} at optimal bias $\pm V_B^{opt}(A_{sig})$ which is defined as the point of minimum differential conductance at the current plateau i.e. between the plateau onset $\pm V_B^{on}(A_{sig})$ and the error onset $\pm V_B^{err}(A_{sig})$. In figure 6.2c and 6.2d, $V_B^{opt}(A_{sig})$ is indicated by white circles. In device C, the extracted points seem to 'stick' to the plateau onset line, as opposed to device D. We will focus the ongoing discussion to the $V_B^{opt}(A_{sig})$ trace which follows the error onset line, as the opposite polarity trace is severely affected by the presence of a substructure in the current plateau.

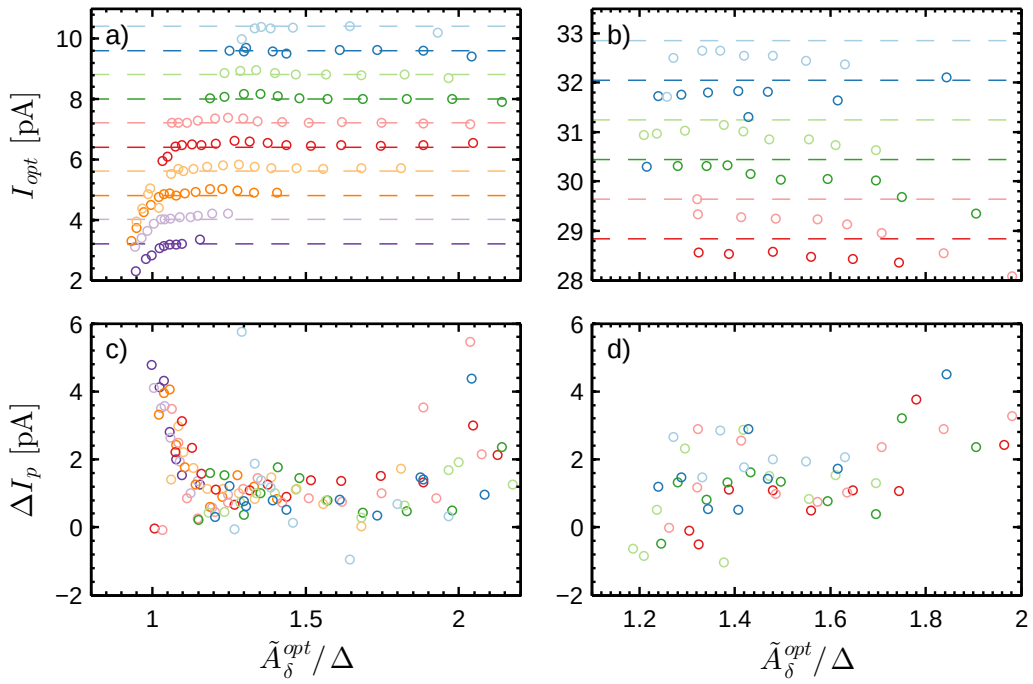

Figure 6.6: Turnstile current along the line of minimal differential conductance at the current plateau (a, b) and the current drop ΔI_p (c, d), as function of A_δ for a set of frequencies (5 MHz steps) in the low (a: 20 - 65 MHz) and high (b: 180 - 205 MHz) modulation regime (sine wave, device D).

For each optimal bias point we determine the turnstile current I_{opt} and the modulation amplitude A_δ of the quantum dot level. Here we assume that the turnstile operation is non-adiabatic[5] such that the plateau onset bias is given eq.(6.1). Later in this chapter it will be shown that this assumption can be violated when the turnstile is operated with a low frequency sine wave modulation signal (adiabatic operation regime). The extracted V_B^{on} value will give an underestimate of 'true' modulation amplitude since the semi-classical onset given by eq. (6.1) is suppressed by missed tunnel events due to the adiabatic operation. On the other hand we can safely assume that I_{opt} is much less affected by the low frequency turnstile operation as the optimal current is extracted at optimal bias where the turnstile operation is non-adiabatic due to a high bias and/or modulation amplitude.

Figure 6.6a and 6.6b show an example of the obtained current points against $\tilde{A}_\delta^{opt} = A_\delta - eV_B^{opt}/2$ for a sine wave gate modulation in two different frequency regimes. We have subtracted the optimal bias V_B^{opt} from the modulation amplitude such that $\tilde{A}_\delta = \Delta$ corresponds to the superconducting gap of the leads. In these plots we have coloured the data points according to the signal frequency. Each set of data points forms a well defined line located at $I \approx ef$. Below $\tilde{A}_\delta = \Delta$ we observe the suppression of the turnstile

[5] A theoretical discussion of the adiabatic operation regime was presented in the previous chapter

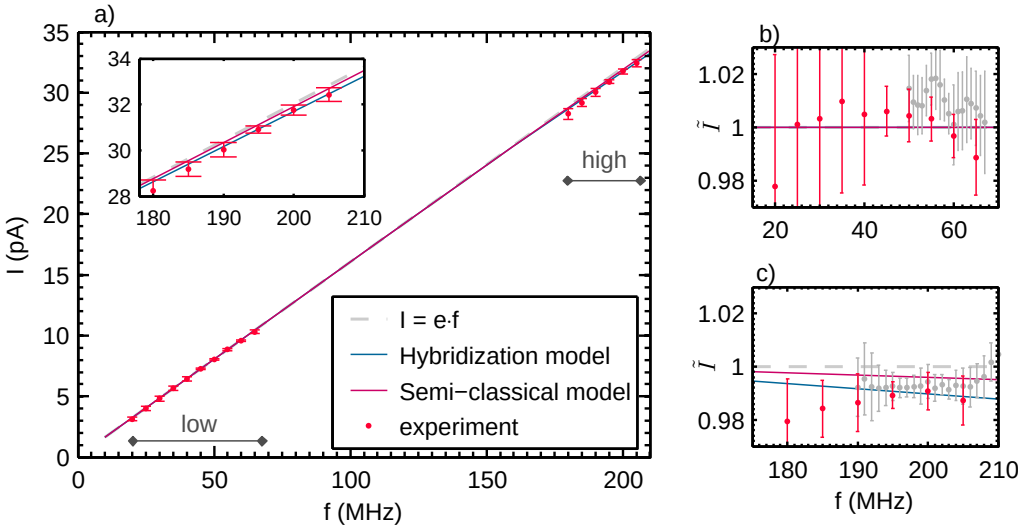

Figure 6.7: a) Turnstile current at optimal bias (average over modulation amplitude) as function of the modulation frequency (sine wave, device D). b,c) Current accuracy in the low (b) and high (c) frequency regime, obtained with a sine wave (magenta) and square wave (grey) modulation signal. (solid line give the theoretical predication based on a semi-classical model (magenta) or 'hybridization' model (blue).)

because of missed tunnel events. At low frequency sine wave operation, the missed tunnel events are possibly caused by the adiabatic turnstile operation as discussed in the previous chapter. At high modulation frequencies we observe a small but gradual decrease in the current as the modulation amplitude increases which we attribute to the gate-bias crosstalk.

The accuracy of the turnstile current can be expressed in terms of the reduced optimal current i.e. $\tilde{I}_{opt} - 1$. As to compare between different modulation frequencies and signal shapes (sine and square), we compute the accuracy averaged over $\Delta \lesssim A_{sig} \lesssim 2\Delta$. Figure 6.7 shows the obtained results for device D as a function of the frequency. The difference between the sine (magenta) and square (grey) wave shape signal is especially profound in the high frequency regime (figure 6.7c) where the turnstile operation suffers from missed tunnel events as can be seen by the current deficit. The somewhat large deficit observed for the sine wave signals corresponds best with the model that takes the quantum dot — superconductor hybridization effect (blue solid line) into account. In the low frequency range we do not observe a difference between the two signal shapes. As to obtain a reasonable accuracy value for low frequency sine wave operations, we omitted the small amplitude I_{opt} values from the average which is justified as the turnstile operation may be adiabatic in this regime.

Plateau flatness and onset

To characterize the plateau flatness we multiply the minimum differential conductance by Δ/e, which yields an estimation of the current variation ΔI_p over the plateau (see figure 6.5). The results of the low frequency sine wave modulation are shown in figure 6.6c. We observe a broad region $1 \lesssim \tilde{A}_\delta \lesssim 2$ where $\Delta I_p \approx 1$ pA. At the region borders, ΔI_p increases while can be attributed to respectively missed tunnel events ($\tilde{A}_\delta \lesssim 1$) and backtunneling or gate-bias crosstalk ($\tilde{A}_\delta \gtrsim 2$). The observation that the lower border uniquely consists of low frequency data ($\leq$ 45 MHz) can indicate adiabatic current suppression as the origin of missed tunnel events. The average ΔI_p of each device, modulation type and frequency range is given in table 6.1. The square wave modulation consistently results in flatter current plateaus as opposed to a sine wave modulation. However, the flatness decreases for both modulation types as the frequency increases.

The second performance parameter of the turnstile to be discussed is the plateau onset. The current onset can be characterized by the bias voltage range over which the reduced current $\tilde{I} = I/ef$ settles (see figure 6.5) i.e. the width of the bright lines in figure 6.2. We estimate the onset width by $\Delta V = 1/\left(d\tilde{I}/dV|_{V_B^{on}}\right)$. As the modulation amplitude should not affect the current transition, ΔV can be averaged over all modulation amplitudes. In the low frequency sine wave operation regime, we observe a small but significant increase in ΔV as the frequency decreases. We will study this feature in more detail in section 6.6.3 as it may indicate adiabatic current suppression. In any other operation regime (square wave or high frequency sine wave), there is no significant relation between ΔV and f. As to compare ΔV between the four operation regimes, we average over all frequencies within each regime. The obtained main values are given in table 6.1. There is a significant difference between the sine and square wave modulation signals in both frequency regimes, which is consistent with the previous observations.

Device & Type	$\tilde{I} - 1$	ΔI_p	ΔV	$\tilde{I} - 1$	ΔI_p	ΔV
Range	low	low	low	high	high	high
Units	%	pA	μeV	%	pA	μeV
C, square	-0.5 ± 2.1	0.79	75 ± 23	n.a.	n.a.	n.a.
D, square	1.2 ± 1.9	0.51	71 ± 8	-0.2 ± 1.2	1.25	93 ± 29
D, sine	1.0 ± 1.6	1.94	125±42	-1.6 ± 1.4	2.53	150±50

Table 6.1: Turnstile plateau characterization by the current accuracy, current drop over the turnstile plateau and the onset rise voltage, measured in the low and high frequency regime of a sine and square wave modulation signal.

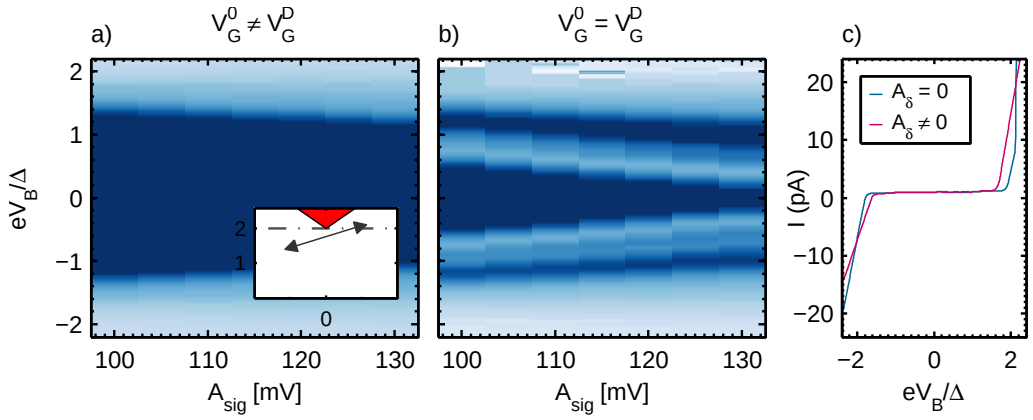

Figure 6.8: Differential conductance maps as function of bias and modulation amplitude measured with a large (a) and zero (b) detuning from the gate offset position (square wave, f = 60 MHz, device C). c) Example current traces as a function of bias at charge degeneracy illustration the cross-talk between the AC gate modulation signal and bias voltage.

6.3 Gate-bias crosstalk

In the previous sections we already took notice of a so-called gate-bias crosstalk without further specifying it. In the devices used for the turnstile experiments, the two superconducting leads are necessarily located on top of the gate, such that there is a non-negligible capacitive coupling between the leads and the gate (~ 14 fF). Crosstalk between the gate and the leads will naturally lead to oscillations in the electrochemical potential of the leads when the gate is modulated by an AC signal. Normally, when the capacitances to the gate are equal, this will only result in an effective reduction of the gate modulation amplitude. However, due to the common drain design in our electromigration chips, there is a factor ~ 10 between the two capacitances. The resulting imbalance in the crosstalk from the gate to source and drain, appears as a modulation of the bias voltage. This adds a vertical component to the trajectory of the quantum dot state in the (V_B, V_G) plain when a modulation signal is applied to the gate (inset figure 6.8a).

In the previous section it was already argued that the gate-bias crosstalk is responsible for the error onset visible in the differential conductance maps of the turnstile current $I_p(V_B, A_{sig})$. To verify that these error lines are indeed related to the effective modulation of the bias, the measurement of figure 6.8b is redone at a gate position far from the charge degeneracy regions (see figure 6.8a). This will exclude the current contribution from the turnstile operation. Again, we observe identical error onset lines as before, but in absence of the turnstile onset lines. Comparing the $I(V_B)$ traces in figure 6.8a with an $I(V_B)$ trace measured under stationary conditions clarifies the typical smoothing due to oscillations in the bias (see figure 6.8c). The turnstile operation of the measured samples is possibly most limited by the gate-bias crosstalk. The bias

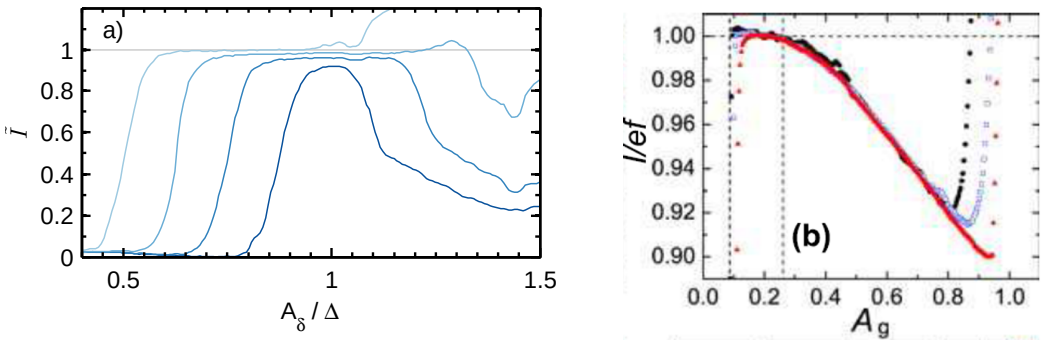

Figure 6.9: a) Normalized turnstile current as function the modulation amplitude of a square wave signal measured at several bias positions (eV_B/Δ = 0.25, 0.50, 0.75, 1). The backtunneling onset is clearly visible by the sudden decrease in current. (f = 56 MHz, device C) b) Similar measurements in the SINIS device show a different signature of the backtunneling (Extracted from [71]).

component in the modulation of the quantum dot state notably decreases the operation range $V_B^{on} \lesssim V_B \lesssim V_B^{err}$ and thereby the performance in terms of plateau flatness and accuracy. To eliminate the crosstalk the samples were redesigned as to balance the capacitances from the source an drain to the gate. The new sample design is shown in figure 1.8a but was not yet measured during this thesis.

6.4 Single-level signature: backtunneling

One of the profound signatures of a single level turnstile is the strong presence of backtunneling. At fixed bias, the turnstile current passes through three different regimes as the modulation amplitude increases (see chapter 5.1.2), i.e. 1) no current when $A_\delta < \Delta - V_B/2e$, 2) the turnstile current plateau when $\Delta - V_B/2e < A_\delta < \Delta + V_B/2e$ and 3) an erroneous regime ($A_\delta > \Delta + V_B/2e$) where backtunneling strongly suppresses the current. All three regimes are clearly visible in figure 6.9a where the normalized turnstile current is plotted against the modulation amplitude of the quantum dot level for 4 different fixed bias values.

The small difference in the plateau current between the curves originates from the finite slope of the turnstile plateau as a function of the bias (see section 6.2.1). Each plateau maintains its value until it is either sharply bent up by the gate-bias cross talk or bent down by backtunneling. This behaviour is fundamentally different from a SINIS turnstile in which the electro-chemical potential of a continuum density of states is modulated. Also in SINIS devices there is a regime in which only 'forward' tunneling is energetically allowed i.e. between the two dashed vertical lines in figure 6.9b. Beyond this regime, backtunneling increasingly suppresses the turnstile current with increasing modulation amplitude. The current suppression with increasing modulation amplitude

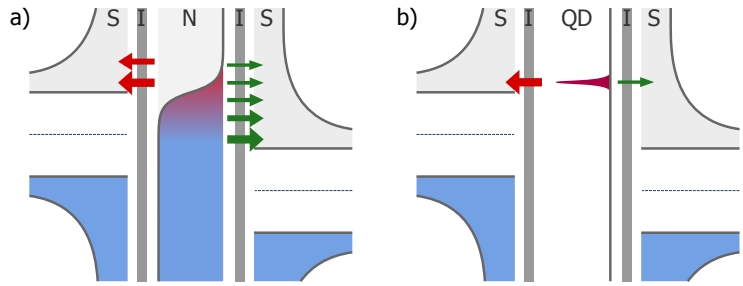

Figure 6.10: Energies schematic illustrating the energy windows available for forward tunneling (green) and backtunneling (red) in a single *electron* turnstile (a) and a single *level* turnstile (b).

in SINIS turnstile device is significantly different from the sharp exponential-like suppression that we observe in the curves of figure 6.9a. The striking difference with our observations can be well understood by the difference in the density of states of the central part of a turnstile as is illustrated by figure 6.10. In a single level turnstile (figure 6.10b) there is only a small energy window (given by the level broadening) available for forward tunnel events. This is opposed to a single electron turnstile (figure 6.10a) in which the available energy window is given by the bias eV_B, which makes it much more robust against backtunneling.

The narrow spectral density of a single quantum dot level would make a sign reversal of the turnstile current possible as was discussed in section 5.1.2. The square wave turnstile operation, optimized to alternate between the two backtunneling threshold positions, favours current in the opposite direction. In our experiments we haven't been able to observe this feature which relies on the singularity at the BCS gap edge. The tunnel coupling observed in our experiments is actually too large compared to the limited rise time of the applied square wave signal. This observation is confirmed by calculations that take the quantum dot — superconductor hybridization into account. As to observe the sign reversal of the current at backtunneling threshold, a lower tunnel coupling would be more favourable.

6.5 Single-level signature: temperature independent accuracy

In the theoretical discussion of the single level turnstile (previous chapter), temperature was completely ignored. The justification is given by the observation that the thermal energy is in fact the smallest energy scale compared to both the superconducting gap and the mean level spacing on the quantum dot. The operation of a single level turnstile should thus be very robust against temperature up to $k_B T \lesssim \min[\Delta, \delta]$, where δ is the mean level spacing on the quantum dot. The consistency of this assertion is verified experimentally by the analysis of the turnstile current plateau as a function of cryostat

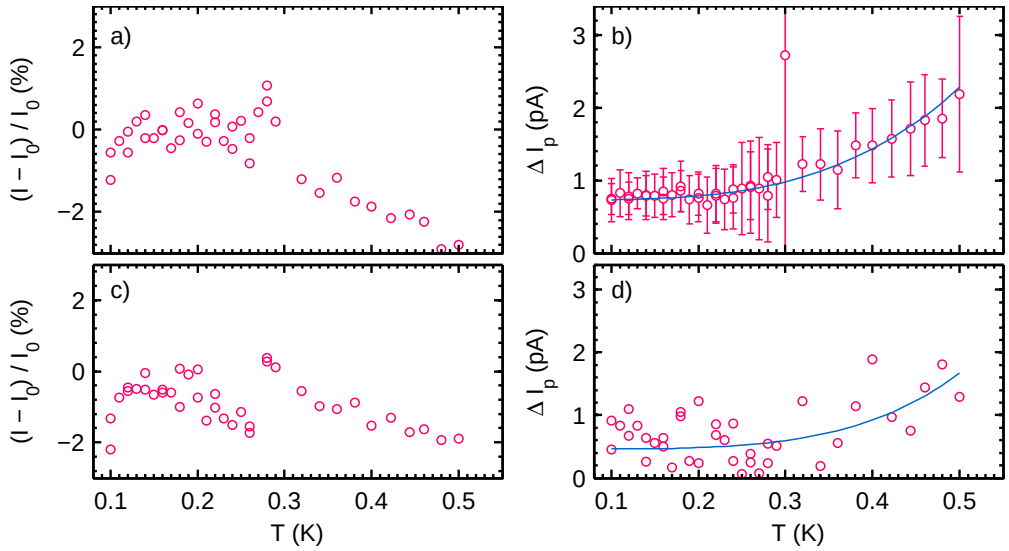

Figure 6.11: Turnstile current accuracy at V_B^{opt}(a, c) and current drop over the plateau (c, d) as function of the cryostat base temperature. The data presented in (a,b) are the average values of all measured modulation amplitudes, while (c,d) only show the data at optimal modulation amplitude. The solid lines are a guide to the eye. (device C, f = 56MHz, square wave)

base temperature. At each cryostat temperature the turnstile current is measured as a function of the bias and for various modulation amplitudes. The DC gate position and modulation frequency are kept constant during the measurements. Again we characterize each turnstile current plateau according to its current at minimum differential conductance and the extended current drop over the plateau.

Figure 6.11 shows the average values obtained from all modulation amplitudes at a given base temperature. With increasing temperature, there is a small gradual decrease in the current accuracy visible (figure 6.11a). Simultaneously we observe a small increase in ΔI_p. Of course we have to consider the possibility that the average values are dominated by the data points extracted at non-optimal modulation amplitudes. The data presented in figure 6.6c showed that optimal turnstile operation is often obtained when $A_\delta \gtrsim \Delta$. Data at optimal modulation amplitude shows an essentially constant current accuracy ΔI_p when the temperature is varied up till ~ 300 mK above which the turnstile performance only weakly deteriorates with further increasing temperature. The decreasing turnstile performance can be due to 1) backtunneling from thermally activated higher quantum dot levels and 2) a finite electron-hole population in the superconducting leads. As the superconducting gap is the smallest energy scale in the device it is likely that the latter process is dominant.

The extremely small temperature dependence of the turnstile plateau in single level turnstiles is notably different from the what is observed in SINIS turnstiles. In an experiment by Nakamura *et al.* [102] with aluminium SINIS junctions, a strong increase

in ΔI_p was observed with increasing temperature above 300 mK. At $T = 500$ mK ΔI_p in Nakamura *et al.* is ≈ 10 pA which is significantly higher than our observation. The robustness of the turnstile operation is a hallmark of a single quantum level conveying the current.

6.6 Adiabatic turnstile operation

So far we have experimentally verified and characterized the turnstile operation of our devices. In the high frequency range we observed a small error in the turnstile current due to a significant increase in missed tunnel events (figure 6.7). The error is consistent with the model discussed in the previous chapter. Moreover, we have shown various signatures illustrating the single level character of our devices. There is a strong decrease in the turnstile current as backtunneling becomes energetically allowed. Furthermore we find that the turnstile plateau remains essentially unchanged up to 500 mK, which is only expected when $k_B T \ll \delta$, where δ is the level spacing on the quantum dot.

Despite the single level character of our devices we have until now always interpreted the system from a semi-classical point of view, based on the Fermi Golden rule. For example, the plateau onset bias was assumed to be directly related to the modulation amplitude by $V_B^{on} = 2\Delta - 2A_\delta$, which is just an energy condition. This semi-classical picture is however only applicable when the coupling between the quantum dot and the superconducting leads can be described as a vanishing perturbation. In the previous chapter however we learned that a non-zero coupling should result in the avoided crossing between a discrete state bound below the superconducting gap edge and a quasi-particle state above. During the turnstile operation, electrons can only tunnel to/from the superconducting leads from the quasi-particle state. A turnstile current is generated provided that the electrons make a transition from the discrete state to the quasi-particle state which only occurs when the quantum dot level excursion becomes diabatic (non-adiabatic). When the system remains adiabatic during the level excursion above (below) the gap edge, the turnstile current will be suppressed as the main part of the electron wave-function remains in the bound state. Our calculations presented in the previous chapter show that we can expect adiabatic current suppression in device C when the quantum dot level is modulated by a sine wave with f below a few tens of MHz. In device D we can expect the adiabatic suppression to extend to higher frequencies as $\max[\gamma_L, \gamma_R]$, is larger. However we do not have experimental data of the turnstile current generated by a sine wave modulation in this device. In the forthcoming sections we present three different observations which are all consistent with the model of adiabatic suppression of the current in device C.

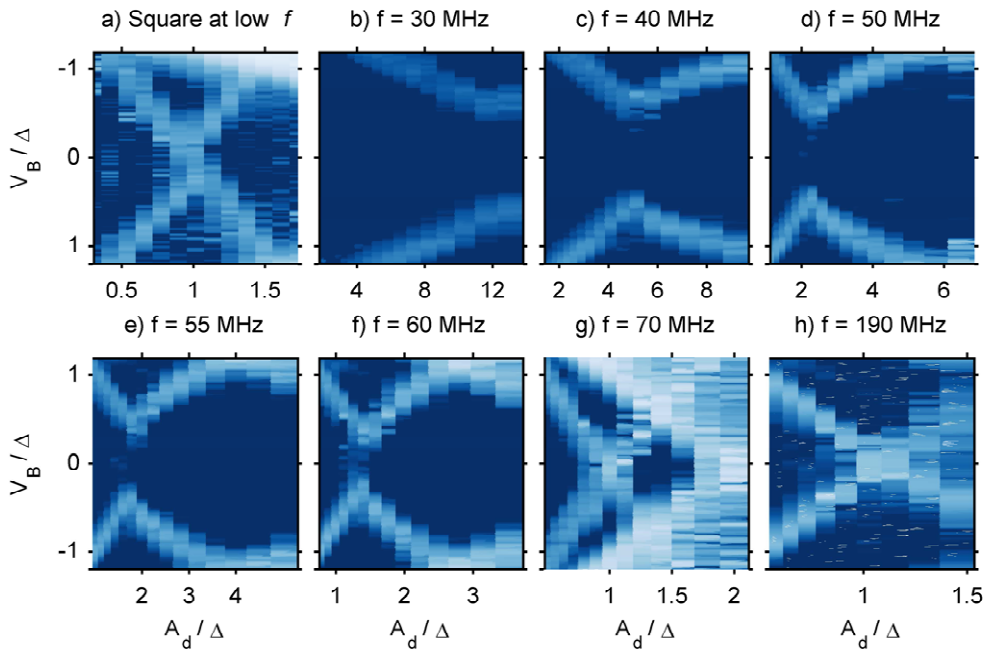

Figure 6.12: Differential conductance maps of the turnstile current as function of the bias and modulation amplitude. a) Operation of the turnstile with a square wave signal always shows the crossing of the plateau onset lines at zero bias. b-f) In the low frequency regime of a sine wave modulation, the turnstile current shows a gap which decreases with increasing frequency. h) In the high sine wave frequency operation regime the gap is zero, and the crossing of the onset lines is recovered. (device D)

6.6.1 The threshold gap

In the semi-classical picture of the turnstile operation around V_G^0, one will always observe the crossing of the two plateau onset lines in the differential conductance at zero bias as for example in figure 6.2d. For any modulation frequency and type, there exists an amplitude at which the turnstile produces an accurate quantized current down to zero bias. Around zero bias, the current will steadily change from $\pm ef$ to $\mp ef$ without interruption as the bias goes through zero. With increasing frequency the dwell time above (below) the gap decreases and one can expect a suppression in current close to zero bias due to missed tunneling events. In the low frequency limit however, the current accuracy should become better. It is therefore rather striking that we observe exactly the opposite behaviour in our experiments conducted at V_G^0 with a sine wave modulation of the quantum dot level as is shown in figure 6.12 (b-g). At high modulation frequency we consistently observe the crossing of the plateau onset lines at zero bias (figure 6.12h). Below 70 MHz, a gap of zero current appears which increases with decreasing modulation frequency (figure 6.12 b-g).

The suppression of the current in the gap appears to be related to the modulation

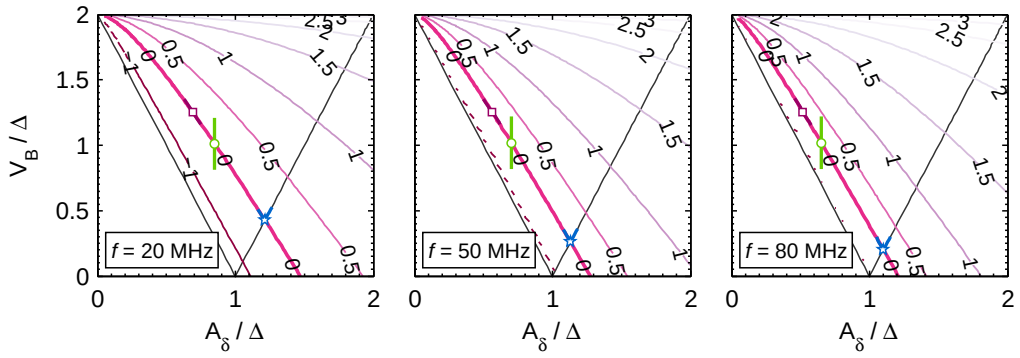

Figure 6.13: Simulated contour maps of the adiabaticity parameter א (on log10 scale) as function of the normalized bias and modulation amplitude of the quantum dot level at three different modulation signals. Grey solid lines denote the classical onset of the turnstile current and backtunneling events. The blue star marks the gap in the turnstile current. The purple open square marks to position where the inconsistent gate coupling is measured. The green circle denotes the position and range where the plateau onset measurements are performed. ($\gamma = 0.04\Delta$, corresponding to device D)

rate as experiments with a square wave modulation signal at equal frequencies again show the crossing of the two plateau onset lines at zero bias (see figure 6.12a). The existence and properties of the gap are remarkably consistent with the picture of the adiabatic suppression of the turnstile current. Figure 6.13(a-c) shows the adiabaticity contour maps of a turnstile operated by a sine wave modulation signal of 30-70 MHz. The solid black lines mark the regions of accurate turnstile operation (no missed event or backtunneling) given by the classical energy conditions. The contour lines give the maximum value (on log10 scale) of the adiabaticity parameter א as defined by eq. (5.14). Adiabatic suppression of the turnstile current is expected when $א \ll 1$. With increasing frequency we observe that the $א = 1$ contour rotates away from the semi-classical condition for the plateau onset, towards higher modulation amplitudes. The backtunneling onset however remains unaffected by the adiabaticity in the system. Once an electron made the transition from the discrete state below the reduced gap into the quasi-particle state, the system behaves semi-classically[6]. The co-existence of the adiabatic suppression and backtunneling produces a frequency dependent gap as observed in figure 6.12 (blue star). As the rise time of our square wave modulation signal ($t_{RT} = 1.6$ ns) is much smaller and frequency independent, the $א = 1$ contour will always coincide with the semi-classical condition of the plateau onset, which is consistent with the absence of a gap in the square wave experiments.

A gap in the turnstile differential conductance map can also arise when the turnstile is operated at a non-zero detuning from V_G^0 as was illustrated in figure 6.4d. In this case, the forward and reverse tunneling thresholds cross at non-zero bias and produce a gap in

[6]The crossing of a quasi-particle state with the superconducting gap edge does not show any avoided crossing like the discrete state does.

f (MHz)	$\kappa^{\square}$	$\kappa^{\sim}$	$\kappa^{\square}/\kappa^{\square}_{70}$	$\kappa^{\sim}/\kappa^{\square}_{70}$	$\kappa^{\sim}/\kappa^{\square}$
30	0.075	0.045	0.39	0.23	0.59
40	0.133	0.083	0.70	0.43	0.62
60	0.218	0.188	1.14	0.98	0.86
70	0.191	0.216	1.00	1.13	1.13

Table 6.2: Proportionality factors between the modulation amplitude and the onset bias V_B^{on} from differential conductance maps in the low frequency regime of square and sine wave modulation signals. (device D)

the dI_p/dV_B map. The size of the gap is would then however be *frequency independent* but depends linearly on the gate detuning. As to produce a gap comparable to those in figure 6.12 an accidental[7] gate detuning would need to be significantly larger than the gate noise in our measurements. Figure 6.14 shows the turnstile current as a function of the gate detuning and modulation amplitude measured at $eV_B = \Delta$ and low frequency square wave operation. Extending the current onset line $V_G - V_G^0 = 3A_\delta/\Delta$ to $A_\delta = 1$ indicates that the gate detuning required to generate a gap as large as $eV_B = \Delta$ is 1.5 mV. To create a gap as observed in figure 6.12c ($\sim \Delta/2$) the minimum gate detuning would be $750\mu eV$ which is huge! Together with the observed frequency dependence, an explanation of the observed gap in terms of a non-zero gate detuning becomes strongly unlikely.

6.6.2 Calibration of A_δ

Note that the $\aleph = 1$ contour in figure 6.13 always crosses $eV_B = \pm 2\Delta$ at $A_\delta = 0$ but under an angle (w.r.t the the amplitude axes) which depends on the modulation frequency. This implies that the local slope of $eV_B^{on}(A_\delta)$ (e.g. around the purple square in figure 6.13) will deviate from -2 as expected from eq. (6.1). Recall that the accidental detuning of the center gate position will not result in such a deviation. We can parametrize the new relation simply by the incorporation of a frequency dependent correction factor i.e. $eV_B^{on} = 2\Delta - 2\chi(f)A_\delta$. When the system can be described semi-classically, the correction factor is simply given by $\chi(f) = 1$. The observation of a frequency dependent $\chi(f) < 1$, would be consistent with the presence of adiabatic suppression.

Unfortunately, since the signal transmission $c(f)$ i.e. the proportionality between A_δ and A_{sig}, also depends on frequency, the experimental local slope is determined by $\kappa = 2\chi(f)c(f)$ rather than $\kappa = \chi(f)$. To be able to distinguish between $\chi(f)$ and $c(f)$ further information is required. Under the assumption that the signal transmission is shape independent, all necessary information is provided by experiments conducted with a square wave driving. As the lines observed in these experiments are determined by the semi-classical picture i.e. $\chi(f) = 1$, we can determine the signal transmission

[7] All presented measurements are carefully positioned at V_G^0 direct before starting the measurement.

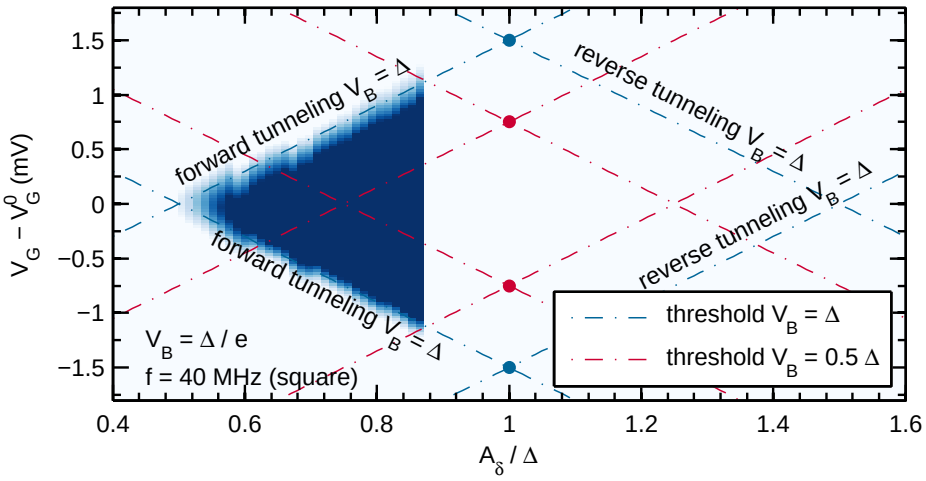

Figure 6.14: Turnstile current map as a function of gate detuning and modulation amplitude. The turnstile current appears as a diamond enclosed by four threshold lines of which only a small part is measured.

parameter $c(f)$ from the experimental slope $\partial V_B^{on}/\partial A_{sig}$. The value of $\chi(f)$ is now easily obtained by $\chi(f) = \kappa^{\sim}/\kappa^{\square}$. In table 6.2 we list the experimentally obtained proportionality $\kappa = c(f)\chi(f)$ between V_B^{on} and A_{sig} in the low modulation amplitude regime for both modulation types.

Assuming $\kappa = c(f)$ for both sine and square wave operation at 70 MHz, all values can be normalized according to the proportionality factor measured with the square wave modulation ($\kappa_{70}^{\square}$). The discrepancy between the normalized values indicate that $\kappa^{\sim}$ value is not exclusively determined by the signal transmission i.e. $\kappa^{\sim} \neq c(f)$. Moreover the ratio $\kappa^{\sim}/\kappa^{\square}$ increases with decreasing modulation frequency which is consistent with the hypothesis of adiabatic current suppression.

6.6.3 The onset transition width

A detailed study of the plateau onset transition in the low frequency regime of the sine wave modulation is justified. As these transitions are probably governed by Landau-Zener physics, the shape of the transition may be frequency-dependent. A closer look at the iso-ℵ lines in figure 6.13 shows a decreasing spacing between the lines as the frequency increases. This indicates a steeper increase of the adiabatic parameter as function of the bias which will result in a sharper current onset.

In the analysis of the current onset transition we compare the differential conductance of the normalized current traces (red dotted data in figure 6.15) at $eV_B \approx \Delta$. The modulation amplitude at each frequency is chosen such that the current onset takes place at $eV_B \approx \Delta$ (green circle in figure 6.13). The peaks in the differential conduc-

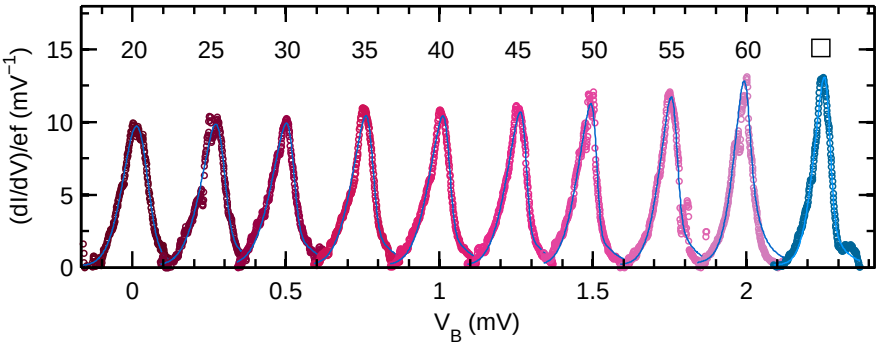

Figure 6.15: Normalized differential conductance peaks of the plateau onset measured at several modulation frequencies (20-60 MHz) of a sine wave (shifted by 0.25 mV). The modulation amplitude of each onset is adapted such that the onset takes place at $V_B \approx \Delta$. The rightmost curve shows the differential conductance of the onset measured with a square wave modulation signal (f = 50MHz). (device D)

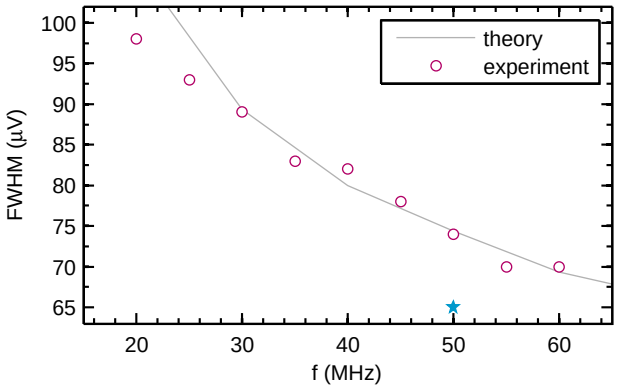

Figure 6.16: Full-width-half-maximum (FWHM) values of the differential conductance peaks presented in figure 6.15 for sine (circles) and square (star) wave modulation signal. The solid grey curve represents the theoretical estimation based on the adiabatic model.

tance can be well fitted with a quasi-Voigt function[8] containing a skewed Gaussian contribution (blue solid curves) which is convenient dor the extraction a a full-width hall-maximum value.

Since the turnstile operation with a square wave modulation signal will be fully semi-classical, its differential conductance peak (blue curve in figure 6.16) serves as a good reference. With decreasing frequency there is a well visible decrease in the maximum value of the peaks generated by the sine wave modulation. Even at f = 60 MHz, there still is a small difference between the sine and square wave operation. To quantify the difference between the peaks, we extract their full-width-half-maximum (FWHM) values. Figure 6.16 shows the extracted values against the modulation frequency. The blue star gives the result for a square wave modulation. There is a clear decrease in

[8]The quasi-Voigt function is a linear combination of a Lorentzian and (skewed) Guassian profile.

the FWHM visible with increasing frequency, which is consistent with a plateau onset dominated by the adiabatic suppression.

In the previous sections we showed that there is no significant difference in the plateau current accuracy between the various frequencies (in the low range) which indicates that all classical considerations like e.g. the dwell time, do not play a dominant role. As to compare the data with the adiabatic model we determine the bias distances between the $\aleph = 0.1$ and $\aleph = 1$ contour line in figure 6.13 at equal A_δ and close to $V_B = \Delta$ at each frequency. Without any scaling factor we find a reasonable correspondent between the experimental data and the obtained theoretical estimation as presented by the grey solid line in figure 6.16.

6.6.4 Adiabaticity breaking

Together the three different observations form a compelling argument that the measured current onset obtained with a low frequency sine wave modulation, is in fact the transition from the adiabatic to the diabatic operation regime. The observation of adiabatic current suppression was rather unexpected for us and can have profound implications.

Spectral isolation of the subgap state

Adiabatic evolution of the turnstile operation requires a 'hard' gap with a diverging density of states at the gap edge as was shown in the previous chapter. Intrinsic broadening of the gap edge will soften the spectral separation between the gap edge an the discrete bound state such that non-diabetic transitions become likely. A semi-classical but intuitive explanation can be given in terms of tunnel events between the discrete sub-gap state and sub-gap states in the superconducting leads. During adiabatic operation, an electron is 'stuck' in the discrete state bound below the superconducting gap edge. When the bare level energy goes beyond $\Delta - eV_B/2$, the discrete level is 'pressed' against the gap edge (see figure 6.17) where the presence of sub-gap states in the leads would allow the electron to escape from the discrete quantum dot state. One should therefore compare the spectral separation $\epsilon_A - \Delta$ with the intrinsic broadening of the superconducting gap edge caused by the finite Cooper-pair lifetime in superconductors [29]. The broadening of the diverging coherence peaks in the superconducting density of states is well characterized by the Dynes parameter (see eq. 4.5). DC measurements presented in chapter 4 set an upper bound $5 \cdot 10^{-5}\Delta$ to the Dynes parameter which is in fact limited by the current noise in our system. Other experiments [131, 115] set the upper bound of the Dynes parameter in aluminium to $1.7 \cdot 10^{-7}$ by the use of full-counting statistics. In order to obtain this result, the measurement had to be executed in a micro-wave filtered sample cavity as photon-assisted tunneling can also broaden

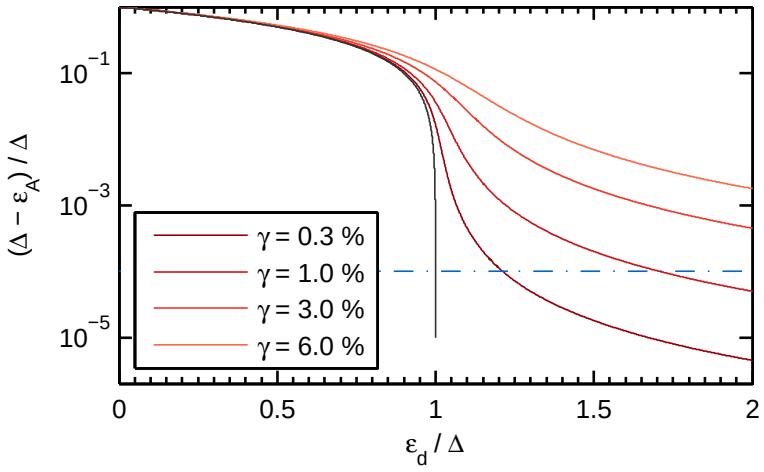

Figure 6.17: Calculated energy difference between the superconducting gap edge and the discrete Andreev level as function of the normalized bare energy level (controlled by the gate) for several tunnel coupling values. The black lines corresponds to the classical situation where the hybridization is neglected. The dashed lines is drawn at 10^{-4}.

the coherence peaks. As our measurements were conducted in a similar environment[9] it is reasonable to assume an equally low Dynes parameter[10].

Turnstile operation at A_δ and $V_B = \Delta/2$, limits the bare energy level to $A_\delta + eV_B/e = 3/2\Delta$. Taking the measured tunnel coupling $\gamma \approx 0.03\Delta$ into account we obtain an lower limit to the spectral separation $\Delta - \epsilon_A \geq 5 \cdot 10^{-3}\Delta \simeq 1\mu$eV during the level trajectory which is well above the intrinsic broadening of the diverging coherence peaks. We can therefore safely conclude that the discrete sub-gap state is well defined and the gap-edge is 'diverging'.

Decoherence of the electron wave-function in the leads

During the period when the level is pressed against the gap edge, the electron wave-function is divided over the quasi-particle state above and the discrete state below the gap edge. As the majority of the electron wave-function is located in the discrete state $|A\rangle$, the change that the electron will tunnel out through the quasi-particle state is essentially zero. However, during the dwell time the wave-function belonging to $|A\rangle$, spreads out into the superconductor where it might loose its coherence. If it does, the electron wave-function can not be re-collected at the end of the dwell time and is ejected into the lead. The loss of phase coherence in the leads therefore breaks the adiabatic current suppression. Our observation of current suppression at 20 MHz

[9] That is a doubled shielded sampled cavity with measurement wires filtered by 1 meter Thermocoax

[10] Here we might also benefit from a large shunt capacitance (present due to the small but relatively long geometry of the electro-migration gaps), which suppresses environmentally activated tunnel events [133].

implies phase coherence of the electron wave-function in the leads during the dwell of ~ 10 ns at $A_\Delta \approx 1.5\Delta$ which is consistent with qubit experiments in which coherence times superior to $\sim 1\mu$s are measured [76].

Summary

Electrons in condensed (solid) matter display a remarkable rich behaviour that is yet, despite decades of research, at most partially explored. The basis of this versatility lies with the wave-particle duality of electrons as formulated by De Broglie in 1924. Prior to the de-Broglie hypothesis, electrons were thought of as corpuscular entities. Three years later, in 1927, the wave-like character of electrons was confirmed in 'the most beautiful physics experiment', conducted by Davisson and Germer [24]. As the interference can only arise from a wave-like character, the experiment demonstrates the true essence of quantum-mechanics.

Still the particle-like representation of electrons is not entirely wrong. In normal metals the electron wave-function quickly suffers from phase decoherence due to the (abundant) interactions with its environment e.g. inelastic scattering with electrons, phonons and photons. With the loss of phase coherence, (self)interference effects vanish and electrons become 'classical' particles. Even when electrons are subjected to quantum mechanical features e.g. tunneling and level discretization, an experiment can often be considered classical as its relevant time scales exceeds the phase decoherence time. In this thesis, the electron transport through quantum dot - superconductor single electron transistor devices was studied under *stationary* and *turnstile* conditions. As the electron tunnel rates in SETs are generally the longest time scale, we initially considered the experiment from this quasi-classical point of view. However, we find that a 'hard' superconducting gap in the lead density of states combined with a large level spacing enhances the coherent state of the quantum dot.

Assuming semi-classical conditions, we first considered the charge and heat transport between a small normal island (zero level spacing) and the superconducting leads numerically using first order perturbation theory. Heat maps of the SET in (V_B, V_G) space show areas of positive heat flux out of the normal island located around the charge degeneracy points, that is, cooling. Away from charge degeneracy however, the flux is exponentially suppressed by the charging energy, which results in a strong localization in gate space as E_C increases. Introducing a finite level spacing δ on the island has two important ramifications. As thermal excitations are frozen out, electron temperature is no longer defined. Furthermore, the broadening of electronic quantum dot level

is dominated by the tunneling coupling (hybridization) as both the electron-electron and electron-phonon interaction are negligible in small-size quantum dots. This makes quantum dots with large level spacing unfavourable for studying electronic cooling.

Employing the in-situ electromigration of aluminium nanowires, superconducting contacts to gold nano-particle (4 nm) quantum dots are established. As to study their electronic properties, we have carefully measured the current under stationary conditions. The experimental data indeed shows a non-thermal broadening of the coherence peaks at current threshold. The excellent agreement with a model describing quantum dot - lead hybridization indicates a vanishing inelastic scattering rate on the quantum dot. The agreement is especially striking in the sub-threshold (including sub-gap) regime where other models, e.g. environmentally activated tunneling, severely deviate. With these measurements we have shown that electron transport through the quantum dot - superconductor devices is conveyed by a single phase-coherent electronic level.

To operate the devices as a turnstile, a periodic modulation signal (sine or squares wave) is added to the back-gate potential. We measure a quantized current $I = ef$ ($\lesssim 1$ % error) up to operation frequencies around 200 MHz. The obtained turnstile current plateaus as a function of the bias show a small but finite slope, possibly contributed by the bias-gate crosstalk. The single quantum dot level character of these devices is particularly well illustrated by 1) a marked threshold type onset of electron backtunneling events and 2) a vanishingly small temperature dependence of the turnstile current accuracy.

Besides these quasi-classical hallmarks, we find yet another striking feature indicating the quantum coherent evolution of the single electron wave function during turnstile operation. The tunnel coupling between the quantum dot level and the superconducting leads, induces (besides broadening of transport features) a small anti-crossing in the spectral density of the quantum dot. Under adiabatic operation, the electron will always remain in the ground state while the bare level makes an excursion above the superconducting gap. During this trajectory, the electron wave function initially spreads out into the superconducting leads, with only its evanescent part located at the quantum dot. As the bare level returns below the gap, the electron wave function is forced back into the quantum dot.

As a consequence tunnel events are missed as the frequency is lowered, which is completely contradicting the semi-classical picture. Loss of phase coherence, when spread out in the leads, would result in the ejection of the electron as the wave function can not be forced back into the quantum dot. Otherwise, adiabatic operation will result in missed tunnel events.

Our observation of adiabatic tunneling suppression down to 20 MHz requires a lower

bound of about 5 ns to the electron coherence time in superconducting leads. This is not surprising as the electron-phonon scattering and quasi-particle recombination times in aluminium are known to be much larger. Also the interaction between quasi-particles is expected to be small, as there are essentially none present above the superconducting gap. Unfortunately we were unable to drive our turnstile device below 20 MHz due to decreasing signal transmission. Further measurements at even lower frequency regime may possibly reveal the recovery of the semi-classical picture as the adiabatic operation might become disturbed by the loss of phase coherence in the leads.

The theoretical consideration of 1) the adiabatic current suppression and 2) the missed tunnel events presented in this thesis suggests promising turnstile accuracy within an unbounded frequency region with increasing tunnel coupling. It is however likely that there is an upper limit to the coupling, set by n-th order Cooper-pair — electron cotunneling processes, each characterised by a minimum bias $V_B > \Delta/n$ threshold. Furthermore the presence of a Kondo resonance at zero bias can be anticipated with increasing tunnel coupling. Consequently there may be an optimal bias at which the combined error contribution will be minimal. Further study of these processes is necessary as to determine whether single level turnstile devices can reach metrological accuracy at an operation frequency exceeding 1 GHz.

In addition to the metrological application, the single level turnstile may possibly find use in quantum computing. One might imagine this system as an coherence preserving electron box. Stored electrons only loose coherence once it has been ejected into the superconducting leads. However the maximum storage time may be limited by higher-order Cooper-pair electron cotunneling processes and Kondo mediated multiple Andreev reflections. Again, further study of these processes is necessary to determine the storage time.

Bibliography

[1] B. Altshuler, Y. Gefen, A. Kamenev, and L. Levitov. Quasiparticle Lifetime in a Finite System: A Nonperturbative Approach. *Phys. Rev. Lett.*, 78(14):2803–2806, Apr. 1997.

[2] T. Aref, V. F. Maisi, M. Gustafsson, P. Delsing, and J. P. Pekola. Andreev tunneling in charge pumping with SINIS turnstiles. pages 1–6, 2011.

[3] D. Averin and J. P. Pekola. Nonadiabatic Charge Pumping in a Hybrid Single-Electron Transistor. *Phys. Rev. Lett.*, 101(6):066801, Aug. 2008.

[4] D. V. Averin and K. K. Likharev. Coulomb blockade of single-electron tunneling, and coherent oscillations in small tunnel junctions. *J. Low Temp. Phys.*, 62(3-4):345–373, Feb. 1986.

[5] D. V. Averin, A. A. Odintsov, and S. V. Vyshenskii. Ultimate accuracy of single-electron dc current standards. *J. Appl. Phys.*, 73(3):1297, Feb. 1993.

[6] Axon. Micro-D connectors, 2015.

[7] C. W. J. Beenakker. Theory of Coulomb-blockade oscillations in the conductance of a quantum dot. *Phys. Rev. B*, 44(4):1646–1656, July 1991.

[8] H. Bluhm and K. a. Moler. Dissipative cryogenic filters with zero dc resistance. *Rev. Sci. Instrum.*, 79(1):014703, Jan. 2008.

[9] M. Blumenthal, B. Kaestner, L. Li, S. Giblin, T. Janssen, M. Pepper, D. Anderson, G. Jones, and D. Ritchie. Electron pumping through quantum dots defined in parallel etched quantum wires. *Microelectronics J.*, 39(3-4):365–368, Mar. 2008.

[10] M. D. Blumenthal, B. Kaestner, L. Li, S. Giblin, T. J. B. M. Janssen, M. Pepper, D. Anderson, G. Jones, and D. A. Ritchie. Gigahertz quantized charge pumping. *Nat. Phys.*, pages 343–347, 2007.

[11] K. I. Bolotin. *Spin-dependent transport in nanoscale structures.* PhD thesis, 2007.

[12] K. I. Bolotin, F. Kuemmeth, a. N. Pasupathy, and D. C. Ralph. Metal-nanoparticle single-electron transistors fabricated using electromigration. *Appl. Phys. Lett.*, 84(16):3154, 2004.

[13] E. Bonet, M. M. Deshmukh, D. C. Ralph, and A. Pasupathy. Solving rate equations for electron tunneling via discrete quantum states. *Phys. Rev. B*, 65(4):073301, Jan. 2002.

[14] H. Bruus and K. Flensberg. *Many-Body Quantum Theory in Condensed Matter Physics: An Introduction*. Oxford Graduate Texts. OUP Oxford, 2004.

[15] M. Buitelaar, T. Nussbaumer, and C. Schönenberger. Quantum Dot in the Kondo Regime Coupled to Superconductors. *Phys. Rev. Lett.*, 89(25):256801, Dec. 2002.

[16] C. Buizert, A. Oiwa, K. Shibata, K. Hirakawa, and S. Tarucha. Kondo Universal Scaling for a Quantum Dot Coupled to Superconducting Leads. *Phys. Rev. Lett.*, 99(13):136806, Sept. 2007.

[17] E. Burzurí, Y. Yamamoto, M. Warnock, X. Zhong, K. Park, A. Cornia, and H. S. J. van der Zant. Franck-Condon blockade in a single-molecule transistor. *Nano Lett.*, 14(6):3191–6, June 2014.

[18] J. M. Campbell and R. G. Knobel. Feedback-controlled electromigration for the fabrication of point contacts. *Appl. Phys. Lett.*, 102(2):023105, Oct. 2013.

[19] S. J. Chorley, J. Frake, C. G. Smith, G. a. C. Jones, and M. R. Buitelaar. Quantized charge pumping through a carbon nanotube double quantum dot. *Appl. Phys. Lett.*, 100(14):143104, Apr. 2012.

[20] C. Cohen-Tannoudji, B. Diu, and F. Laloë. *Quantum Mechanics Volume 2*. Hermann.

[21] M. R. Connolly, K. L. Chiu, S. P. Giblin, M. Kataoka, J. D. Fletcher, C. Chua, J. P. Griffiths, G. A. C. Jones, V. I. Fal'ko, C. G. Smith, and T. J. B. M. Janssen. Gigahertz quantized charge pumping in graphene quantum dots. *Nat. Nanotechnol.*, 8(6):417–20, July 2013.

[22] H. Courtois, S. Rajauria, P. Gandit, F. W. J. Hekking, and B. Pannetier. Inherent Thermometry in a Hybrid Superconducting Tunnel Junction. *J. Low Temp. Phys.*, 153(5-6):325–338, Oct. 2008.

[23] S. Datta, D. Strachan, and A. Johnson. Gate coupling to nanoscale electronics. *Phys. Rev. B*, 79(20):205404, May 2009.

[24] C. Davisson and L. Germer. Diffraction of Electrons by a Crystal of Nickel. *Phys. Rev.*, 30(6):705–740, Dec. 1927.

[25] R. S. Deacon, Y. Tanaka, A. Oiwa, R. Sakano, K. Yoshida, K. Shibata, K. Hirakawa, and S. Tarucha. Tunneling Spectroscopy of Andreev Energy Levels in a Quantum Dot Coupled to a Superconductor. *Phys. Rev. Lett.*, 104(7):076805, Feb. 2010.

[26] Y. N. Demkov and V. I. Osherov. Stationary and nonstationary problems in quantum mechanics that can be solved by means of contour integration. *Sov. Phys. JETP*, 26(916):1, 1968.

[27] M. H. Devoret, D. Esteve, and C. Urbina. Single-electron transfer in metallic nanostructures. *Nature*, 360(6404):547–553, Dec. 1992.

[28] T. Dittrich. *Quantum transport and dissipation.* Wiley-VCH, 1998.

[29] R. Dynes, V. Narayanamurti, and J. Garno. Direct Measurement of Quasiparticle-Lifetime Broadening in a Strong-Coupled Superconductor. *Phys. Rev. Lett.*, 41(21):1509–1512, Nov. 1978.

[30] F. Elste and C. Timm. Cotunneling and nonequilibrium magnetization in magnetic molecular monolayers. *Phys. Rev. B*, 75(19):195341, May 2007.

[31] Emerson & Cuming. Eccosorb, 2015.

[32] G. Esen and M. S. Fuhrer. Temperature control of electromigration to form gold nanogap junctions. *Appl. Phys. Lett.*, 87(26):263101, 2005.

[33] D. K. Ferry, S. M. Goodnick, and J. Bird. *Transport in Nanostructures.* Transport in Nanostructures. Cambridge University Press, 2009.

[34] A. V. Feshchenko, J. V. Koski, and J. P. Pekola. Experimental realization of a Coulomb blockade refrigerator. *Phys. Rev. B*, 90(20):201407, Nov. 2014.

[35] G. Fève, A. Mahé, J.-M. Berroir, T. Kontos, B. Plaçais, D. C. Glattli, A. Cavanna, B. Etienne, and Y. Jin. An on-demand coherent single-electron source. *Science*, 316(5828):1169–72, May 2007.

[36] J. D. Fletcher, M. Kataoka, S. P. Giblin, S. Park, H.-S. Sim, P. See, D. A. Ritchie, J. P. Griffiths, G. A. C. Jones, H. E. Beere, and T. J. B. M. Janssen. Stabilization of single-electron pumps by high magnetic fields. *Phys. Rev. B*, 86(15):155311, Oct. 2012.

[37] G. Frens. Controlled Nucleation for the Regulation of the Particle Size in Monodisperse Gold Suspensions. *Nat. Phys. Sci.*, 241(105):20–22, Jan. 1973.

[38] L. Fricke, M. Wulf, B. Kaestner, F. Hohls, P. Mirovsky, B. Mackrodt, R. Dolata, T. Weimann, K. Pierz, U. Siegner, and H. W. Schumacher. Self-Referenced Single-Electron Quantized Current Source. *Phys. Rev. Lett.*, 112(22):226803, June 2014.

[39] L. Fricke, M. Wulf, B. Kaestner, V. Kashcheyevs, J. Timoshenko, P. Nazarov, F. Hohls, P. Mirovsky, B. Mackrodt, R. Dolata, T. Weimann, K. Pierz, and H. Schumacher. Counting Statistics for Electron Capture in a Dynamic Quantum Dot. *Phys. Rev. Lett.*, 110(12):126803, Mar. 2013.

[40] A. Fujiwara, K. Nishiguchi, and Y. Ono. Nanoampere charge pump by single-electron ratchet using silicon nanowire metal-oxide-semiconductor field-effect transistor. *Appl. Phys. Lett.*, 92(4):042102, 2008.

[41] A. Fujiwara and Y. Takahashi. Manipulation of elementary charge in a silicon charge-coupled device. *Nature*, 410(6828):560–2, Mar. 2001.

[42] A. Fujiwara, N. M. Zimmerman, Y. Ono, and Y. Takahashi. Current quantization due to single-electron transfer in Si-wire charge-coupled devices. *Appl. Phys. Lett.*, 84(8):1323, 2004.

[43] T. Fulton and G. Dolan. Observation of single-electron charging effects in small tunnel junctions. *Phys. Rev. Lett.*, 59(1):109–112, July 1987.

[44] L. Geerligs, V. Anderegg, P. Holweg, J. Mooij, H. Pothier, D. Esteve, C. Urbina, and M. Devoret. Frequency-locked turnstile device for single electrons. *Phys. Rev. Lett.*, 64(22):2691–2694, May 1990.

[45] F. Giazotto, T. Heikkilä, A. Luukanen, A. Savin, and J. P. Pekola. Opportunities for mesoscopics in thermometry and refrigeration: Physics and applications. *Rev. Mod. Phys.*, 78(1):217–274, Mar. 2006.

[46] S. P. Giblin, M. Kataoka, J. D. Fletcher, P. See, T. J. B. M. Janssen, J. P. Griffiths, G. A. C. Jones, I. Farrer, and D. A. Ritchie. Towards a quantum representation of the ampere using single electron pumps. *Nat. Commun.*, 3:930, Jan. 2012.

[47] K. Gloos, P. J. Koppinen, and J. P. Pekola. Properties of native ultrathin aluminium oxide tunnel barriers. *J. Phys. Condens. Matter*, 15(10):1733–1746, Mar. 2003.

[48] S. R. Groot. *Thermodynamics of irreversible processes.* Selected topics in modern physics. North-Holland Pub. Co., 1963.

[49] S. Guéron, H. Pothier, N. Birge, D. Esteve, and M. Devoret. Superconducting Proximity Effect Probed on a Mesoscopic Length Scale. *Phys. Rev. Lett.*, 77(14):3025–3028, Sept. 1996.

[50] H. B. Heersche, P. Jarillo-Herrero, J. B. Oostinga, L. M. K. Vandersypen, and A. F. Morpurgo. Bipolar supercurrent in graphene. *Nature*, 446(7131):56–9, Mar. 2007.

[51] P. S. Ho and T. Kwok. Electromigration in metals. *Reports Prog. Phys.*, 52(3):301–348, Mar. 1989.

[52] Y. Hu, H. O. H. Churchill, D. J. Reilly, J. Xiang, C. M. Lieber, and C. M. Marcus. A Ge/Si heterostructure nanowire-based double quantum dot with integrated charge sensor. *Nat. Nanotechnol.*, 2(10):622–5, Oct. 2007.

[53] P. Jarillo-Herrero, J. A. van Dam, and L. P. Kouwenhoven. Quantum supercurrent transistors in carbon nanotubes. *Nature*, 439(7079):953–6, Feb. 2006.

[54] X. Jehl, M. Keller, R. Kautz, J. Aumentado, and J. Martinis. Counting errors in a voltage-biased electron pump. *Phys. Rev. B*, 67(16):165331, Apr. 2003.

[55] X. Jehl, B. Voisin, T. Charron, P. Clapera, S. Ray, B. Roche, M. Sanquer, S. Djordjevic, L. Devoille, R. Wacquez, and M. Vinet. Hybrid Metal-Semiconductor Electron Pump for Quantum Metrology. *Phys. Rev. X*, 3(2):021012, May 2013.

[56] H. Jensen and J. Martinis. Accuracy of the electron pump. *Phys. Rev. B*, 46(20):13407–13427, Nov. 1992.

[57] S. Jezouin, F. D. Parmentier, A. Anthore, U. Gennser, A. Cavanna, Y. Jin, and F. Pierre. Quantum limit of heat flow across a single electronic channel. *Science*, 342(6158):601–4, Nov. 2013.

[58] G. Johansson, E. Bratus, V. Shumeiko, and G. Wendin. Resonant multiple Andreev reflections in mesoscopic superconducting junctions. *Phys. Rev. B*, 60(2):1382–1393, July 1999.

[59] B. Kaestner, C. Leicht, V. Kashcheyevs, K. Pierz, U. Siegner, and H. W. Schumacher. Single-parameter quantized charge pumping in high magnetic fields. *Appl. Phys. Lett.*, 94(1):012106, 2009.

[60] B. Kaestner, C. Leicht, P. Mirovsky, V. Kashcheyevs, E. V. Kurganova, U. Zeitler, K. Pierz, H. W. Schumacher, J. Ihm, and H. Cheong. Constructive Role Of Nonadiabaticity For Quantized Charge Pumping. 345(2011):345–346, 2011.

[61] S. Kafanov, a. Kemppinen, Y. Pashkin, M. Meschke, J. Tsai, and J. Pekola. Single-Electronic Radio-Frequency Refrigerator. *Phys. Rev. Lett.*, 103(12):120801, Sept. 2009.

[62] D. Kahng. A historical perspective on the development of MOS transistors and related devices. *IEEE Trans. Electron Devices*, 23(7):655–657, July 1976.

[63] K. Kang. Transport through an interacting quantum dot coupled to two superconducting leads. *Phys. Rev. B*, 57(19):891–894, 1998.

[64] V. Kashcheyevs and B. Kaestner. Universal Decay Cascade Model for Dynamic Quantum Dot Initialization. *Phys. Rev. Lett.*, 104(18):186805, May 2010.

[65] M. Kataoka, J. D. Fletcher, P. See, S. P. Giblin, T. J. B. M. Janssen, J. P. Griffiths, G. A. C. Jones, I. Farrer, and D. A. Ritchie. Tunable Nonadiabatic Excitation in a Single-Electron Quantum Dot. *Phys. Rev. Lett.*, 106(12):126801, Mar. 2011.

[66] G. Katsaros, P. Spathis, M. Stoffel, F. Fournel, M. Mongillo, V. Bouchiat, F. Lefloch, A. Rastelli, O. G. Schmidt, and S. De Franceschi. Hybrid superconductor-semiconductor devices made from self-assembled SiGe nanocrystals on silicon. *Nat. Nanotechnol.*, 5(6):458–64, June 2010.

[67] R. Kautz, M. Keller, and J. Martinis. Leakage and counting errors in a seven-junction electron pump. *Phys. Rev. B*, 60(11):8199–8212, Sept. 1999.

[68] R. Kautz, M. Keller, and J. Martinis. Noise-induced leakage and counting errors in the electron pump. *Phys. Rev. B*, 62(23):15888–15902, Dec. 2000.

[69] E. Kawakami, P. Scarlino, D. R. Ward, F. R. Braakman, D. E. Savage, M. G. Lagally, M. Friesen, S. N. Coppersmith, M. A. Eriksson, and L. M. K. Vandersypen. Electrical control of a long-lived spin qubit in a Si/SiGe quantum dot. *Nat. Nanotechnol.*, 9(9):666–70, Sept. 2014.

[70] M. W. Keller, J. M. Martinis, N. M. Zimmerman, and A. H. Steinbach. Accuracy of electron counting using a 7-junction electron pump. *Appl. Phys. Lett.*, 69(12):1804, 1996.

[71] A. Kemppinen, S. Kafanov, Y. A. Pashkin, J. S. Tsai, D. V. Averin, and J. P. Pekola. Experimental investigation of hybrid single-electron turnstiles with high charging energy. *Appl. Phys. Lett.*, 94(17):172108, 2009.

[72] B. K. Kim, Y. H. Ahn, J. J. Kim, M. S. Choi, M. H. Bae, K. Kang, J. S. Lim, R. Lopez, and N. Kim. Transport measurement of andreev bound states in a kondo-correlated quantum dot. *Phys. Rev. Lett.*, 110(February):1–5, 2013.

[73] H. Kim, P. C. McIntyre, and K. C. Saraswat. Effects of crystallization on the electrical properties of ultrathin HfO[sub 2] dielectrics grown by atomic layer deposition. *Appl. Phys. Lett.*, 82(1):106, 2003.

[74] H. S. Knowles, V. F. Maisi, and J. P. Pekola. Probing quasiparticle excitations in a hybrid single electron transistor. *Appl. Phys. Lett.*, 100, 2012.

[75] J. König, H. Schoeller, and G. Schön. Cotunneling at Resonance for the Single-Electron Transistor. *Phys. Rev. Lett.*, 78(23):4482–4485, June 1997.

[76] F. H. L. Koppens, C. Buizert, K. J. Tielrooij, I. T. Vink, K. C. Nowack, T. Meunier, L. P. Kouwenhoven, and L. M. K. Vandersypen. Driven coherent oscillations of a single electron spin in a quantum dot. *Nature*, 442(7104):766–71, Aug. 2006.

[77] P. J. Koppinen, T. Kühn, and I. J. Maasilta. Effects of charging energy on SINIS tunnel junction thermometry. *J. Low Temp. Phys.*, 154(5-6):12, 2008.

[78] A. Korotkov, D. Averin, and K. Likharev. Single-electron charging of the quantum wells and dots. *Phys. B Condens. Matter*, 165-166:927–928, Aug. 1990.

[79] J. Koski, V. Maisi, T. Sagawa, and J. Pekola. Experimental Observation of the Role of Mutual Information in the Nonequilibrium Dynamics of a Maxwell Demon. *Phys. Rev. Lett.*, 113(3):030601, July 2014.

[80] J. V. Koski, V. F. Maisi, J. P. Pekola, and D. V. Averin. Experimental realization of a Szilard engine with a single electron. *Proc. Natl. Acad. Sci. U. S. A.*, 111(38):13786–9, Sept. 2014.

[81] L. Kouwenhoven, A. Johnson, N. van der Vaart, C. Harmans, and C. Foxon. Quantized current in a quantum-dot turnstile using oscillating tunnel barriers. *Phys. Rev. Lett.*, 67(12):1626–1629, Sept. 1991.

[82] L. P. Kouwenhoven, A. T. Johnson, N. C. van der Vaart, A. van der Enden, C. J. P. M. Harmans, and C. T. Foxon. Quantized current in a quantum dot turnstile. *Zeitschrift für Phys. B Condens. Matter*, 85(3):381–388, Oct. 1991.

[83] F. Kuemmeth, K. I. Bolotin, S.-f. Shi, and D. C. Ralph. Measurement of discrete energy-level spectra in individual chemically synthesized gold nanoparticles. *Nano Lett.*, 8(12):4506–12, Dec. 2008.

[84] A. Kumar, M. Gaim, D. Steininger, A. L. Yeyati, A. Martín-Rodero, a. K. Hüttel, and C. Strunk. Temperature dependence of Andreev spectra in a superconducting carbon nanotube quantum dot. *Phys. Rev. B*, 89(7):075428, Feb. 2014.

[85] G. P. Lansbergen, Y. Ono, and A. Fujiwara. Donor-based single electron pumps with tunable donor binding energy. *Nano Lett.*, 12(2):763–8, Feb. 2012.

[86] M. M. Leivo, J. P. Pekola, and D. V. Averin. Efficient Peltier refrigeration by a pair of normal metal/insulator/superconductor junctions. *Appl. Phys. Lett.*, 68(14):1996, Apr. 1996.

[87] R. Leturcq, C. Stampfer, K. Inderbitzin, L. Durrer, C. Hierold, E. Mariani, M. G. Schultz, F. von Oppen, and K. Ensslin. FranckCondon blockade in suspended carbon nanotube quantum dots. *Nat. Phys.*, 5(5):327–331, Apr. 2009.

[88] A. Levy Yeyati and J. Cuevas. Resonant tunneling through a small quantum dot coupled to superconducting leads. *Phys. Rev. B*, 55(10):6137–6140, 1997.

[89] K. K. Likharev and A. B. Zorin. Theory of the Bloch-wave oscillations in small Josephson junctions. *J. Low Temp. Phys.*, 59(3-4):347–382, May 1985.

[90] S. V. Lotkhov, S. A. Bogoslovsky, A. B. Zorin, and J. Niemeyer. Operation of a three-junction single-electron pump with on-chip resistors. *Appl. Phys. Lett.*, 78(7):946, Feb. 2001.

[91] S. V. Lotkhov, A. Kemppinen, S. Kafanov, J. P. Pekola, and a. B. Zorin. Pumping properties of the hybrid single-electron transistor in dissipative environment. *Appl. Phys. Lett.*, 95(11):112507, 2009.

[92] K. Luo and Z. Yao. Fabrication of nanometer-spaced superconducting Pb electrodes. *Appl. Phys. Lett.*, 95(11):113115, 2009.

[93] G. D. Mahan. *Many-Particle Physics*. NATO Asi Series. Springer, 1990.

[94] N. Maire, F. Hohls, B. Kaestner, K. Pierz, H. W. Schumacher, and R. J. Haug. Noise measurement of a quantized charge pump. *Appl. Phys. Lett.*, 92(8):082112, 2008.

[95] V. F. Maisi, S. V. Lotkhov, A. Kemppinen, A. Heimes, J. T. Muhonen, and J. P. Pekola. Excitation of Single Quasiparticles in a Small Superconducting Al Island Connected to Normal-Metal Leads by Tunnel Junctions. *Phys. Rev. Lett.*, 111(14):147001, Oct. 2013.

[96] V. F. Maisi, Y. A. Pashkin, S. Kafanov, J.-S. Tsai, and J. P. Pekola. Parallel pumping of electrons. *New J. Phys.*, 11(11):113057, Nov. 2009.

[97] J. Martinis, M. Nahum, and H. Jensen. Metrological accuracy of the electron pump. *Phys. Rev. Lett.*, 72(6):904–907, Feb. 1994.

[98] Y. Meir and N. Wingreen. Landauer formula for the current through an interacting electron region. *Phys. Rev. Lett.*, 68(16):2512–2515, Apr. 1992.

[99] T. Meng, S. Florens, and P. Simon. Self-consistent description of Andreev bound states in Josephson quantum dot devices. *Phys. Rev. B*, 79(22):224521, June 2009.

[100] N. Moussy. *Mesoscopic superconductors probed by very low temperature scanning tunnelining microscopy*. Theses, Universit{é} Joseph-Fourier - Grenoble I, 2000.

[101] M. Nahum, T. M. Eiles, and J. M. Martinis. Electronic microrefrigerator based on a normal-insulator-superconductor tunnel junction. *Appl. Phys. Lett.*, 65(24):3123, Dec. 1994.

[102] S. Nakamura, Y. Pashkin, J.-S. Tsai, and N.-H. Kaneko. Temperature dependence of single-electron pumping using a SINIS turnstile. *Phys. C Supercond.*, 504:93–96, Sept. 2014.

[103] Y. V. Nazarov and Y. M. Blanter. *Quantum Transport: Introduction to Nanoscience*. Cambridge University Press, 2009.

[104] K. S. Novoselov, a. K. Geim, S. V. Morozov, D. Jiang, M. I. Katsnelson, I. V. Grigorieva, S. V. Dubonos, and a. a. Firsov. Two-dimensional gas of massless Dirac fermions in graphene. *Nature*, 438(7065):197–200, Nov. 2005.

[105] K. ONeill, E. a. Osorio, and H. S. J. van der Zant. Self-breaking in planar few-atom Au constrictions for nanometer-spaced electrodes. *Appl. Phys. Lett.*, 90(13):133109, 2007.

[106] Y. Ono and Y. Takahashi. Electron pump by a combined single-electron/field-effect- transistor structure. *Appl. Phys. Lett.*, 82(8):1221, 2003.

[107] Y. Ono, Y. Takahashi, K. Yamazaki, M. Nagase, H. Namatsu, K. Kurihara, and K. Murase. Fabrication method for IC-oriented Si single-electron transistors. *IEEE Trans. Electron Devices*, 47(1):147–153, 2000.

[108] E. Osorio, K. O'Neill, N. Stuhr-Hansen, O. Nielsen, T. Bjø rnholm, and H. vanderZant. Addition Energies and Vibrational Fine Structure Measured in Electromigrated Single-Molecule Junctions Based on an Oligophenylenevinylene Derivative. *Adv. Mater.*, 19(2):281–285, Jan. 2007.

[109] E. A. Osorio, K. O'Neill, M. Wegewijs, N. Stuhr-Hansen, J. Paaske, T. Bjø rnholm, and H. S. J. van der Zant. Electronic excitations of a single molecule contacted in a three-terminal configuration. *Nano Lett.*, 7(11):3336–42, Nov. 2007.

[110] H. Park, A. K. L. Lim, a. P. Alivisatos, J. Park, and P. L. McEuen. Fabrication of metallic electrodes with nanometer separation by electromigration. *Appl. Phys. Lett.*, 75(2):301, 1999.

[111] H. Park, J. Park, A. Lim, E. Anderson, A. Alivisatos, and P. McEuen. Nanomechanical oscillations in a single-C60 transistor. *Nature*, 407(6800):57–60, Sept. 2000.

[112] L. Pascal. Electronic refrigeration and Thermal couplings in Superconducting Hybrid Devices. 2012.

[113] J. P. Pekola. Towards quantum thermodynamics in electroniccircuits. *Nat. Phys.*, 11(2):118–123, Feb. 2015.

[114] J. P. Pekola, T. Heikkilä, A. Savin, J. Flyktman, F. Giazotto, and F. Hekking. Limitations in Cooling Electrons using Normal-Metal-Superconductor Tunnel Junctions. *Phys. Rev. Lett.*, 92(5):056804, Feb. 2004.

[115] J. P. Pekola, V. F. Maisi, S. Kafanov, N. Chekurov, A. Kemppinen, Y. a. Pashkin, O.-P. Saira, M. Möttönen, and J. S. Tsai. Environment-Assisted Tunneling as an Origin of the Dynes Density of States. *Phys. Rev. Lett.*, 105(2):026803, July 2010.

[116] J. P. Pekola, O.-P. Saira, V. F. Maisi, A. Kemppinen, M. Möttönen, Y. A. Pashkin, and D. V. Averin. Single-electron current sources: Toward a refined definition of the ampere. *Rev. Mod. Phys.*, 85(4):1421–1472, Oct. 2013.

[117] J. P. Pekola, J. J. Vartiainen, M. Möttönen, O.-P. Saira, M. Meschke, and D. V. Averin. Hybrid single-electron transistor as a source of quantized electric current. *Nat. Phys.*, 4(2):120–124, Dec. 2007.

[118] J.-D. Pillet, P. Joyez, R. Žitko, and M. F. Goffman. Tunneling spectroscopy of a single quantum dot coupled to a superconductor: From Kondo ridge to Andreev bound states. *Phys. Rev. B*, 88(4):045101, July 2013.

[119] J.-D. Pillet, C. H. L. Quay, P. Morfin, C. Bena, A. L. Yeyati, and P. Joyez. Andreev bound states in supercurrent-carrying carbon nanotubes revealed. *Nat. Phys.*, 6(12):965–969, Nov. 2010.

[120] H. Pothier, S. Guéron, N. Birge, D. Esteve, and M. Devoret. Energy Distribution Function of Quasiparticles in Mesoscopic Wires. *Phys. Rev. Lett.*, 79(18):3490–3493, Nov. 1997.

[121] H. Pothier, P. Lafarge, C. Urbina, D. Esteve, and M. H. Devoret. Single-Electron Pump Based on Charging Effects. *Europhys. Lett.*, 17(3):249–254, Jan. 1992.

[122] S. Rajauria. *Electronic refrigeration using superconducting tunnel junctions*. PhD thesis, 2008.

[123] S. Rajauria, P. Luo, T. Fournier, F. Hekking, H. Courtois, and B. Pannetier. Electron and Phonon Cooling in a SuperconductorNormal-MetalSuperconductor Tunnel Junction. *Phys. Rev. Lett.*, 99(4):047004, July 2007.

[124] D. C. Ralph, C. Black, and M. T. Tinkham. Spectroscopic Measurements of Discrete Electronic States in Single Metal Particles. *Phys. Rev. Lett.*, 74(16):3241–3244, 1995.

[125] D. C. Ralph, C. T. Black, and M. Tinkham. Gate-Voltage Studies of Discrete Electronic States in Aluminum Nanoparticles. *Phys. Rev. Lett.*, (d):4087–4090, 1997.

[126] D. Ristè, C. C. Bultink, M. J. Tiggelman, R. N. Schouten, K. W. Lehnert, and L. DiCarlo. Millisecond charge-parity fluctuations and induced decoherence in a superconducting transmon qubit. *Nat. Commun.*, 4(May):1913, Jan. 2013.

[127] N. Roch. *Single molecule transistors: from exotic Kondo effects to molecular spintronics*. Theses, Universit{é} Joseph-Fourier - Grenoble I, Nov. 2009.

[128] N. Roch, R. Vincent, F. Elste, W. Harneit, W. Wernsdorfer, C. Timm, and F. Balestro. Cotunneling through a magnetic single-molecule transistor based on N@C_{60}. *Phys. Rev. B*, 83(8):081407, Feb. 2011.

[129] B. Roche, R.-P. Riwar, B. Voisin, E. Dupont-Ferrier, R. Wacquez, M. Vinet, M. Sanquer, J. Splettstoesser, and X. Jehl. A two-atom electron pump. *Nat. Commun.*, 4:1581, Jan. 2013.

[130] A. Rossi, T. Tanttu, K. Y. Tan, I. Iisakka, R. Zhao, K. W. Chan, G. C. Tettamanzi, S. Rogge, A. S. Dzurak, and M. Möttönen. An accurate single-electron pump based on a highly tunable silicon quantum dot. *Nano Lett.*, 14(6):3405–11, June 2014.

[131] O.-P. Saira, A. Kemppinen, V. F. Maisi, and J. P. Pekola. Vanishing quasiparticle density in a hybrid Al/Cu/Al single-electron transistor. *Phys. Rev. B*, 85(1):012504, Jan. 2012.

[132] O.-P. Saira, M. Meschke, F. Giazotto, A. Savin, M. Möttönen, and J. P. Pekola. Heat Transistor: Demonstration of Gate-Controlled Electronic Refrigeration. *Phys. Rev. Lett.*, 99(2):027203, July 2007.

[133] O.-P. Saira, M. Möttönen, V. F. Maisi, and J. P. Pekola. Environmentally activated tunneling events in a hybrid single-electron box. *Phys. Rev. B*, 82(15):155443, Oct. 2010.

[134] S. Sapmaz, P. Jarillo-Herrero, Y. Blanter, C. Dekker, and H. van der Zant. Tunneling in Suspended Carbon Nanotubes Assisted by Longitudinal Phonons. *Phys. Rev. Lett.*, 96(2):026801, Jan. 2006.

[135] J. Schindele, A. Baumgartner, R. Maurand, M. Weiss, and C. Schönenberger. Nonlocal spectroscopy of Andreev bound states. *Phys. Rev. B*, 89(4):045422, Jan. 2014.

[136] B. Seeber. *Handbook of Applied Superconductivity.* Number v. 2. CRC Press, 2010.

[137] M. Seo, Y.-H. Ahn, Y. Oh, Y. Chung, S. Ryu, H.-S. Sim, I.-H. Lee, M.-H. Bae, and N. Kim. Improvement of electron pump accuracy by a potential-shape-tunable quantum dot pump. *Phys. Rev. B*, 90(8):085307, Aug. 2014.

[138] L. Spietz, J. Teufel, and R. J. Schoelkopf. A Twisted Pair Cryogenic Filter. *Appl. Phys.*, pages 1–12, 2008.

[139] D. R. Strachan, D. E. Smith, D. E. Johnston, T.-H. Park, M. J. Therien, D. a. Bonnell, and a. T. Johnson. Controlled fabrication of nanogaps in ambient environment for molecular electronics. *Appl. Phys. Lett.*, 86(4):043109, 2005.

[140] ThermoCoax. ThermoCoax, 2015.

[141] S. Thiele, F. Balestro, R. Ballou, S. Klyatskaya, M. Ruben, and W. Wernsdorfer. Electrically driven nuclear spin resonance in single-molecule magnets. *Science*, 344(6188):1135–8, June 2014.

[142] J. M. Thijssen and H. S. J. van der Zant. Charge transport and single-electron effects in nanoscale systems. *Phys. Status Solidi*, 245(8):1455–1470, Aug. 2008.

[143] C. Timm. Tunneling through molecules and quantum dots: Master-equation approaches. *Phys. Rev. B*, 77(19):195416, May 2008.

[144] M. Tinkham. *Introduction to Superconductivity.* Dover Publications, Incorporated, 2012.

[145] M. L. Trouwborst, S. J. van der Molen, and B. J. van Wees. The role of Joule heating in the formation of nanogaps by electromigration. *J. Appl. Phys.*, 99(11):114316, 2006.

[146] J. a. van Dam, Y. V. Nazarov, E. P. a. M. Bakkers, S. De Franceschi, and L. P. Kouwenhoven. Supercurrent reversal in quantum dots. *Nature*, 442(7103):667–70, Aug. 2006.

[147] D. J. van Woerkom, A. Geresdi, and L. P. Kouwenhoven. 1 minute parity lifetime of a NbTiN Cooper-pair transistor. Jan. 2015.

[148] R. Vincent. *Electronic read-out of a single nuclear spin based on a molecular spin transistor.* Theses, Universit{é} de Grenoble, Dec. 2012.

[149] J. von Delft and D. Ralph. Spectroscopy of discrete energy levels in ultrasmall metallic grains. *Phys. Rep.*, 345(2-3):61–173, Apr. 2001.

[150] C. B. Winkelmann, N. Roch, W. Wernsdorfer, V. Bouchiat, and F. Balestro. Superconductivity in a single-C60 transistor. *Nat. Phys.*, 5(12):876–879, Oct. 2009.

[151] S. Wright, M. Blumenthal, G. Gumbs, A. Thorn, M. Pepper, T. Janssen, S. Holmes, D. Anderson, G. Jones, C. Nicoll, and D. Ritchie. Enhanced current quantization in high-frequency electron pumps in a perpendicular magnetic field. *Phys. Rev. B*, 78(23):233311, Dec. 2008.

[152] S. Wright, M. Blumenthal, M. Pepper, D. Anderson, G. Jones, C. Nicoll, and D. Ritchie. Parallel quantized charge pumping. *Phys. Rev. B*, 80(11):113303, Sept. 2009.

[153] Z. M. Wu, M. Steinacher, R. Huber, M. Calame, S. J. van der Molen, and C. Schonenberger. Feedback controlled electromigration in four-terminal nanojunctions. *Appl. Phys. Lett.*, 91(5):053118, Mar. 2007.

[154] G. Yamahata, K. Nishiguchi, and A. Fujiwara. Accuracy evaluation of single-electron shuttle transfer in Si nanowire metal-oxide-semiconductor field-effect transistors. *Appl. Phys. Lett.*, 98(22):222104, June 2011.

[155] G. Yamahata, K. Nishiguchi, and A. Fujiwara. Gigahertz single-trap electron pumps in silicon. *Nat. Commun.*, 5:1–7, Jan. 2014.

[156] L. J. Zeng, S. Nik, T. Greibe, C. M. Wilson, P. Delsing, and E. Olsson. Direct observation of the thickness distribution of ultra thin AlOx barrier in Al/AlOx/Al Josephson junctions. page 5, July 2014.

[157] N. M. Zimmerman, W. H. Huber, A. Fujiwara, and Y. Takahashi. Excellent charge offset stability in a Si-based single-electron tunneling transistor. *Appl. Phys. Lett.*, 79(19):3188, Nov. 2001.

[158] A. B. Zorin. The thermocoax cable as the microwave frequency filter for single electron circuits. *Rev. Sci. Instrum.*, 66(8):4296, Aug. 1995.

[159] A. B. Zorin, S. V. Lotkhov, H. Zangerle, and J. Niemeyer. Coulomb blockade and cotunneling in single electron circuits with on-chip resistors: Towards the implementation of the R pump. *J. Appl. Phys.*, 88(5):2665, Sept. 2000.